Deliverable A2.2

"Analysis of the selected regions and pilot sites"

Project ref. number	LIFE20 PRE/IT/000007
Project title	Remote sensing oriented nature-based solutions towards a NEW LIFE FOR DRYLANDS
Project Acronym	NewLife4Drylands

Deliverable title	Analysis of the selected regions and pilot sites
Deliverable number	2.2
Deliverable version	V1 2nd release: updates
Contractual date of delivery	30/06/2023
Actual date of delivery	30/06/2023
Online access	Yes
Diffusion	Public
Nature of deliverable	Technical
Action	A2
Partner responsible	CNR-IIA
Author(s)	Cristina Tarantino, Saverio Vicario, Maria Adamo, Sabino Maggi, Mariella Aquilino (CNR-IIA) Vicenç Carabassa, Pau Montero, Cristina Domingo (CREAF) Marcello Vitale, Vito Cambria, Martina Perez (SAPIENZA)
Editor	Cristina Tarantino

Executive summary

The present document represents the second part of Deliverable A2.2 already delivered on June 30th, 2022 and contains results related to the extraction from remote sensing data of further indices and sub-indicators at local scale useful to characterize and monitor the land degradation status of each study site according to the local pressures and threats affecting each site. Furthermore, those indices and sub-indicators already described in the previous release are summarised.

Lastly, the document reports SDG 15.3.1 indicator computation with resulting land degradation mapping, as recommended by United Nations Convention to Combat Desertification to characterize the LD status, for each site.

All the indicators were adopted not only for assessing the LD status but also for NBS restoration techniques effectiveness evaluation in those sites with restoration activities on-going or started during the project.

Table of Contents

Acronyms and Abbreviations

Acronym	Description
1OAO	One Out, All Out
BNR	Blue/NIR Ratio
BS	Burn Severity
CERTH-ITI	CEntre for Research & Technology Hellas-Information Technology Institute
CLC	Corine Land Cover
DEM	Digital Elevation Model
dNBR	difference Normalized Burn Ratio
EO	Earth Observation
EOSD	Day of the end of the season
EOSV	Value of the end of the season
ESA	European Space Agency
ETM+	Enhanced Thematic Mapper Plus
EV	Essential Variable
FAO-LCCS	Food and Agriculture Organisation - Land Cover Classification System
GIS	Geographic Information System
HP	Hydro-Period
HR	High Resolution
HR-VPP	High-Resolution Vegetation Phenology and Productivity
kNN	k-Nearest Neighbour
LC	Land Cover
LD	Land Degradation
LIDAR	LIght Detection And Ranging
MAXD	Day of the maximum of the season
MAXV	Value of the maximum of the season
MINV	Value of the minimum of the season
MNDVI	Modified-Normalized Difference Vegetation Index
MSI	MultiSpectral Imager
MODIS	Moderate Resolution Imaging Spectroradiometer

MSAVI	Modified Soil Adjusted Vegetation Index
MW	Micro-Wave
N2K	Natura 2000
NBR	Normalized Burn Ratio
NBS	Nature-Based Solutions
NDVI	Normalized Difference Vegetation Index
NDWI	Normalized Difference Water Index
NIR	Near Infra-Red
OLI	Operational Land Imager
PA	Protected Area
PoB	Peak of Biomass
PostPoB	Post-Peak of Biomass
PP	Primary Productivity
PPI	Plant Phenology Index
PrePoB	Pre-Peak of Biomass
RGB	Red-Green-Blue
RMSE	Root Mean Square Error
RS	Remote Sensing
SDG	Sustainable Development Goal
SOC	Soil Organic Carbon
SOSD	Day of the start of the season
SOSV	Value of the start of the season
SPEI	Standardized Precipitation Evapotranspiration Index
SRTM	Shuttle Radar Topography Mission
SS	Soil Salinity
SVM	Support Vector Machine
SWIR	Short Wave Infra-Red
TM	Thematic Mapper
TPROD	Total productivity
UNCCD	United Nations Convention to Combat Desertification
USGS	United States Geological Survey

UTM	Universal Transverse Mercator
VHR	Very High Resolution
Vis	Visible

1. Introduction

Action A2 has as major outcomes the extraction of information useful to characterize and monitor the LD status of the six study sites from RS data. The activities started from the first month of the project has been arrived at the first release of the present Deliverable A2.2 on June, 30th 2022 containing information about the initial release of indices and sub-indicators at local scale to be integrated into the SDG 15.3.1 indicator computation. Due to the need for more effort to cover all the project's sites, the end of the activities has been extended for a further year. Therefore, this document represents the second part of Deliverable A2.2 and presents the results related to the extraction of the remaining indices and sub-indicators and summarises the results already discussed in the previous version to provide a comprehensive overview of the studies carried out for each site.

Lastly, the document reports SDG 15.3.1 indicator computation with resulting land degradation mapping, according to the United Nations Convention to Combat Desertification recommendation to characterize the LD status, for each site.

All the indicators were adopted not only for assessing the LD status but also for NBS restoration techniques effectiveness evaluation in those sites with restoration activities already on-going or started during the project.

2. Updates in the analysis of the study sites with remote sensing indicators extraction: methodologies and results

The following is a comprehensive overview of the indices and sub-indicators extracted at local scale from remote sensing data for the study sites, according to the related pressures and threats affecting each of them, in order to provide a complete overview for the analysis of the LD status arriving at the SDG 15.3.1 indicator computation and the extraction of LD maps.

2.1 Alta Murgia (Italy)

Alta Murgia study site (SCI IT9120007) is characterized by a dryland ecosystem where natural and semi-natural grassland, hereafter collectively called grasslands, (with 62A0, 6210(*) and 6220* habitat), is dominant hosting numerous endemic and generally rare species (Forte et al., 2005; Tarantino et al., 2021). During last 30-40 years grasslands ecosystem has been exposed to tremendous impacts and accelerated processes of habitat degradation, fragmentation, and biotic contamination (i.e., woody encroachment), both within and next to its borders (Mairota et al., 2015). The practice of stone (rock) graining aimed to drive land use change from pasture to agricultural activities along with fire events, climate change and global warming, increasing of illegal waste and toxic mud dumping and traditional legal/illegal mining activities and the spreading of invasive plant species (Tarantino et al., 2019) have threatened severely the site.
In 2004 the National Park was instituted so a series of protection and safeguard actions started. Hence, a long-term monitoring by RS was considered focusing about how useful was the establishing of National Park authority and what the consequential effects in the LD process of the site have been. The findings, reported in Tarantino et al. (2023), have assessed the key-role of National Park authority whose actions on the territory have resulted effective to preserve grasslands ecosystem conservation. During NL4DL project NBS activities for grasslands restoration are being testing in Alta Murgia site and their effectiveness will be analyzed by the end of the project with same indices/sub-indicators identified for LD monitoring. Figure 1 shows the Alta Murgia study site.

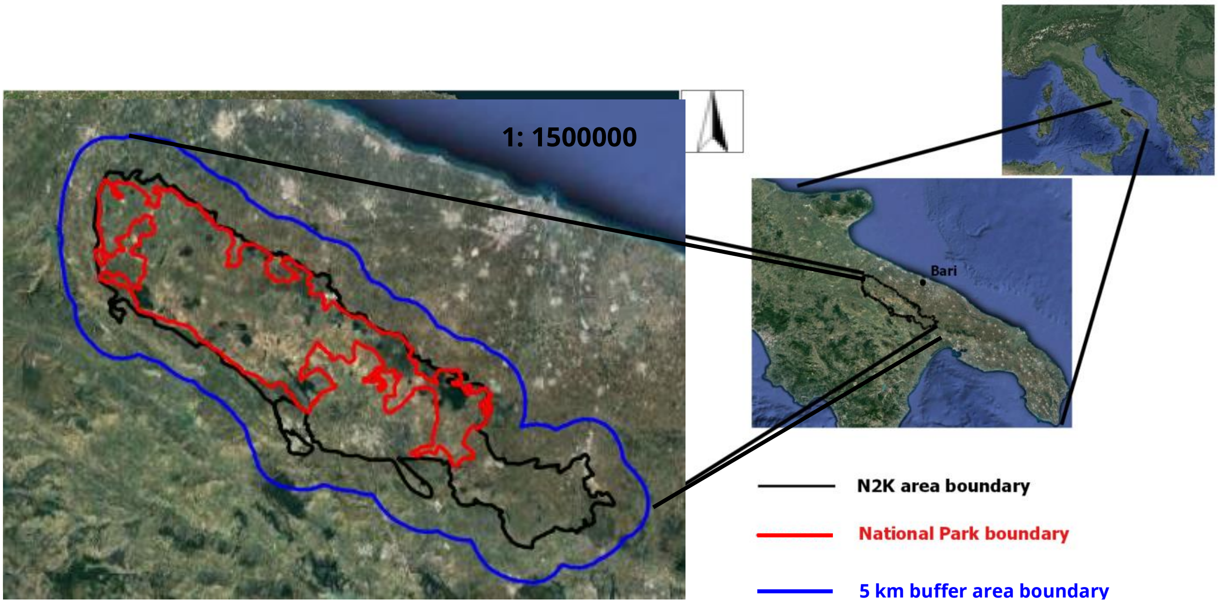

Figure 1. Alta Murgia study site, southern Italy.

For monitoring purpose of the pressures referred to above, according to Deliverable A2.1, the following RS indices and sub-indicators were extracted as reported in Table 1.

Table 1. Indices and sub-indicators selected for Alta Murgia study site.

<table>
<tr><th colspan="2">Sub-indicators</th><th>Sensor</th><th>Spatial resolution (m)</th><th>Spatial frame</th><th>Temporal frame</th></tr>
<tr><td colspan="2" rowspan="2">GRASSLANDS COVER MAP;
BURN SEVERITY MAP</td><td>Landsat</td><td>30</td><td rowspan="6">N2K +5 km buffer</td><td>1990; 2001; 2004; 2011</td></tr>
<tr><td>Sentinel-2</td><td>10</td><td>2018; 2021</td></tr>
<tr><td rowspan="2">PRIMARY PRODUCTIVITY</td><td>VEGETATION PHENOLOGY INDEX (MSAVI2)</td><td>Landsat</td><td>30</td><td>2000-2018</td></tr>
<tr><td>PLANT PHENOLOGY INDEX (PPI)</td><td>Sentinel-2</td><td>10</td><td>2017-2020</td></tr>
<tr><td colspan="2">STANDARDIZED PRECIPITATION EVAPOTRANSPIRATION INDEX (SPEI)</td><td>3 meteo stations</td><td>-----------</td><td>2002-2020</td></tr>
<tr><td colspan="2">SOC</td><td>Soilgrids+ LC maps</td><td>30/10</td><td>1990; 2004; 2018; 2021</td></tr>
</table>

2.1.1 Grasslands Cover temporal trend

Methodology

To obtain LC mappings a multi-temporal dataset composed of four multi-season satellite images was evaluated for each year considered, namely 1990, 2001, 2004, 2011, 2018, 2021. The choice of these years was based on the need for a long-term investigation and the absence of cloud cover along with the open satellite archive of ready-for-processing satellite imagery availability. Indeed, time-series imagery from Landsat satellite collection results from 1990 with well-assessed radiometric and geometric corrections. In addition, for comparison purposes, the selected years result close to (differing no more than ±2 years) the years of the two available products of CLC (https://land.copernicus.eu/pan-european/corine-land-cover) (1990, 2000, 2006, 2012, 2018), at 100 meters spatial resolution, and Copernicus Pan-European HR grasslands layer (https://land.copernicus.eu/pan-european/high-resolution-layers/grassland) (2015 and 2018) at 20 meters and 10 meters spatial resolution, respectively.

From 1990 to 2011, Landsat satellite imagery, at 30-m spatial resolution, was considered, whereas for 2018 and 2021 Sentinel-2 satellite data, 10-m spatial resolution was used. We chose to produce mappings with higher spatial details (10 m) for recent years in order to provide local management authorities to be able to rely on a useful and effective tool. (Tarantino et al; 2023).

For each satellite image the spectral bands in the Vis–NIR–SWIR were considered so resulting in 6 bands for Landsat 5 TM and 10 bands for Sentinel-2 A/B data.

Landsat data were freely downloaded from the USGS EarthExplorer portal (https://earthexplorer.usgs.gov/), Collection 2, Level 2, surface reflectance products, thus, atmospherically correct, and orthorectified using ground data by USGS. The whole N2K PA, plus a 5-km buffer area surrounding its boundary, result covered by the track 188, frame 31 and 32 floating, so a mosaicking step was realized after cropping the boundary of interest. Sentinel-2 data were freely downloaded from the ESA Copernicus Open Access Hub (https://scihub.copernicus.eu/dhus/#/home) as L2A products which are surface reflectance and orthorectified products. Even in this case, the entire study area results covered by the two tiles 33TXF and 33TWF, thus, their mosaicking was needed. The bands with native spatial resolution of 20 meters (i.e., B5, B5, B7, B8A, B11, B12) were resampled, by a Nearest Neighbour algorithm, at 10 meters as those natives (B2, B3, B4, B8).

Table 2 shows the whole set of satellite imagery considered jointly with their acquisition dates.

Table 2. List of satellite imagery considered for the LC mappings.

Year	Acquisition date	Sensor	Spatial resolution (m)	Bands
1990	March, 1st; May, 4th; July, 23rd; September, 25th	Landsat 5 TM	30	B1, B2, B3 (Vis) B4 (NIR) B5, B7 (SWIR) (6 bands)
2001	March, 15th; June, 3rd; August, 6th; November, 26th			
2004	February, 4th; May, 26th; August, 30th; September, 15th			
2011	February, 7th; May, 14th; August, 18th; October, 5th			
2018	January, 30th; April, 20th; July, 19th; October, 27th	Sentinel-2 A/B	10	B2, B3, B4 (Vis) B5, B6, B7 (Red Edge) B8, B8A (NIR) B11, B12 (SWIR) (10 bands)
2021	February, 3rd; May, 24th; July, 23rd; September, 26th			

The four images of each year, with its own bands each one, were stacked obtaining a multi-season raster dataset composed by 24 layers, in the case of Landsat data, or by 40 layers for Sentinel-2 data. Each resulting multi-season dataset, for each year, was the input to a supervised, data-driven, pixel-based classification machine learning algorithm to obtain LC classified maps as output. A set of reference polygons collected through, both, in-field campaigns and visual interpretation of available orthophotos and distributed with a "stratified" sampling to ensure a minimum number of polygons–samples for each class (i.e., stratum) (Congalton et al., 2014) were considered for training the classifier and subsequent validation of the output map. As a result, 70% of each LC class sample was used for training and 30% for the validation, respectively. Ground truth data was related to 12 LC classes, including grasslands, labelled according to FAO-LCCS2 (Di Gregorio & Jansen, 2005) class taxonomy. Nearly 50% of the training and validation pixels were represented by grassland samples since this was the dominant LC in the scene and the class of greatest interest in this study, so high accuracy was required for this class. The list of LC classes mapped is reported in Table 3.

Table 3. LC classes legend according to FAO-LCCS2 taxonomy

Val		Description	Code
0		Unclassified	
1		Cultivated Terrestrial Vegetation/(Trees/Shrubs)Broadleaved.Evergreen	A11/A7.A9
2		Cultivated Terrestrial Vegetation/Trees.Broadleaved.Deciduous	A11/A1.A7.A10
3		Cultivated Terrestrial Vegetation/Shrubs.Broadleaved.Deciduous	A11/A2.A7.A10
4		Cultivated Terrestrial Vegetation/Herbaceous	A11/A3
5		Natural Terrestrial Vegetation/(Trees/Shrubs)Broadleaved.Evergreen	A12/D1.E1
6		Natural Terrestrial Vegetation/(Trees/Shrubs)Broadleaved.Deciduous	A12/ D1.E2
7		Natural Terrestrial Vegetation/(Trees/Shrubs)Needleleaved.Evergreen	A12/ D2.E1
8		Natural Terrestrial Vegetation/Herbaceous.Graminoid (GRASSLANDS)	A12/A2.A6
9		Artificial Surfaces/BuiltUp	B15/A1
10		Artificial Surfaces/NonBuiltUp.ExtractionSites	B15/A2.A6
11		Artificial or Natural Waterbodies/Water	B27-B28/A1
12		Burn Area	

A different SVM classifier (Huang et al., 2002; Mountrakis et al., 2011) was trained for multi-class problems, one for each year, due to its effectiveness in high dimensional spaces (Foody & Mathur, 2004) and well-suited when small training data sets are available. Following the recommendations reported by Othman & Gloaguen (2014), in our study a radial basis function was selected as kernel type while the penalty parameter chosen was taken as 100. The gamma in kernel function was chosen as the inverse of the band numbers used in the data input (Yang, 2011).

Then, from each LC mapping produced as output, the grasslands layer was extracted obtaining a time series of grasslands mappings. The whole workflow for obtaining the grasslands cover mapping, for each year considered, is shown in Figure 2.

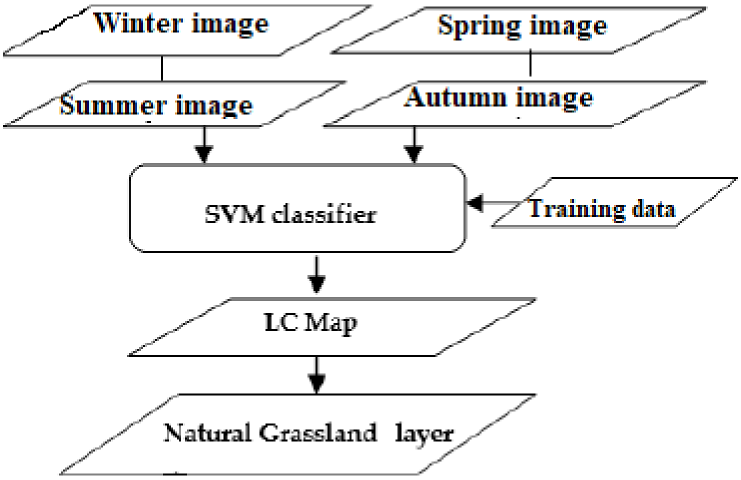

Figure 2. Workflow for grasslands cover mapping.

Results

Figure 3 shows the LC mapping obtained for 2021.

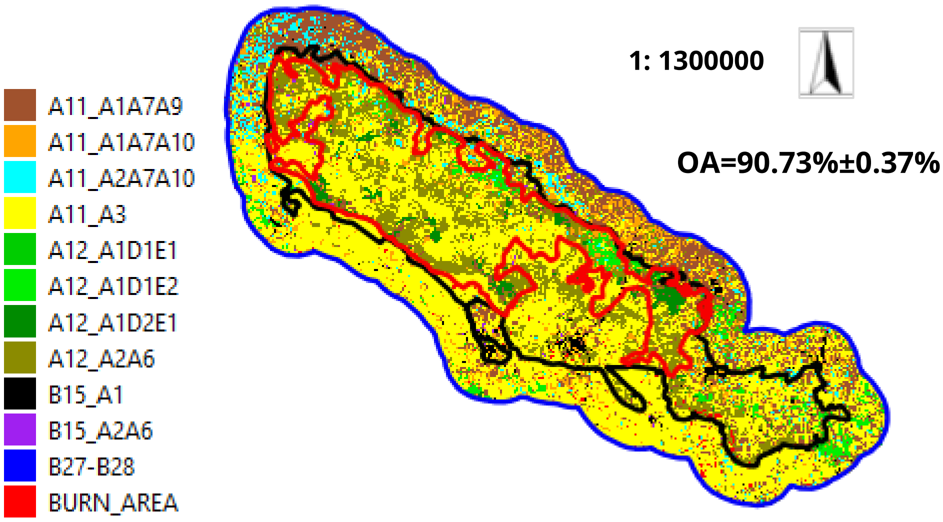

Figure 3. LC mapping for 2021.

The resulting grasslands mappings for each year are shown in Figure 4 jointly with information about Overall Accuracy (OA) in the discrimination of grasslands cover vs. other (binary classification problem). OA is computing according to Congalton & Kass (2009).

As expected, those mappings obtained from Sentinel-2 resulted more detailed (the mapped areas result less smoothed) not only for the higher spatial resolution but also more accurate for the use of more spectral bands (i.e., 10 bands vs. 6) with the addition of the contribution of more spectral ranges for grasslands discrimination.

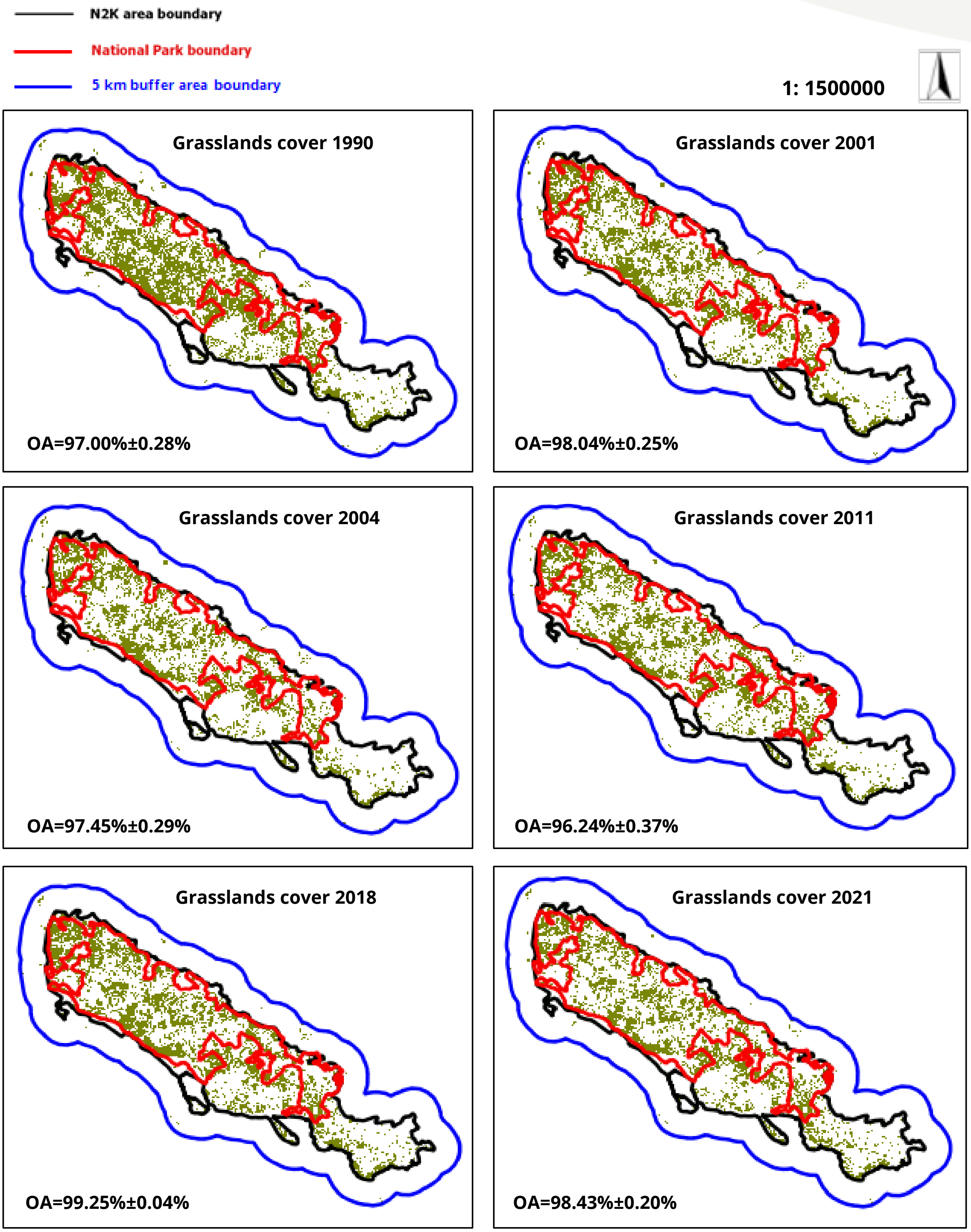

Figure 4. Grasslands cover mapping for the years: 1990, 2001, 2004, 2011, 2018, 2021.

Grasslands coverage, for each year, resulting from the mappings is reported in Table 4.

Table 4. Grasslands cover (ha) for each year within N2K PA, National Park and buffer area only boundaries. The percentage cover over the whole area for each boundary is reported too.

Year	Spatial resolution (m)	N2K PA boundary (126175 ha)	National Park boundary (68192 ha)	Buffer area only boundary (124110 ha)
1990	30	49513 (39.24%)	33610 (49.28%)	899 (0.72%)
2001		36921 (29.26%)	25689 (37.67%)	778 (0.62%)
2004		35140 (27.85%)	24728 (36.26%)	678 (0.54%)
2011		35748 (28.33%)	24673 (36.18%)	638 (0.51%)
2018	10	40679 (32.24%)	27457 (40.26%)	520 (0.42%)
2021		35139 (27.85%)	23427 (34.35%)	435 (0.35%)

Figure 5 shows several plots of the presence of grasslands, within N2K PA and the National Park boundary (on the left) and in a 5-km buffer area surrounding (on the right), during the period 1990-2021 to evaluate its temporal trend.

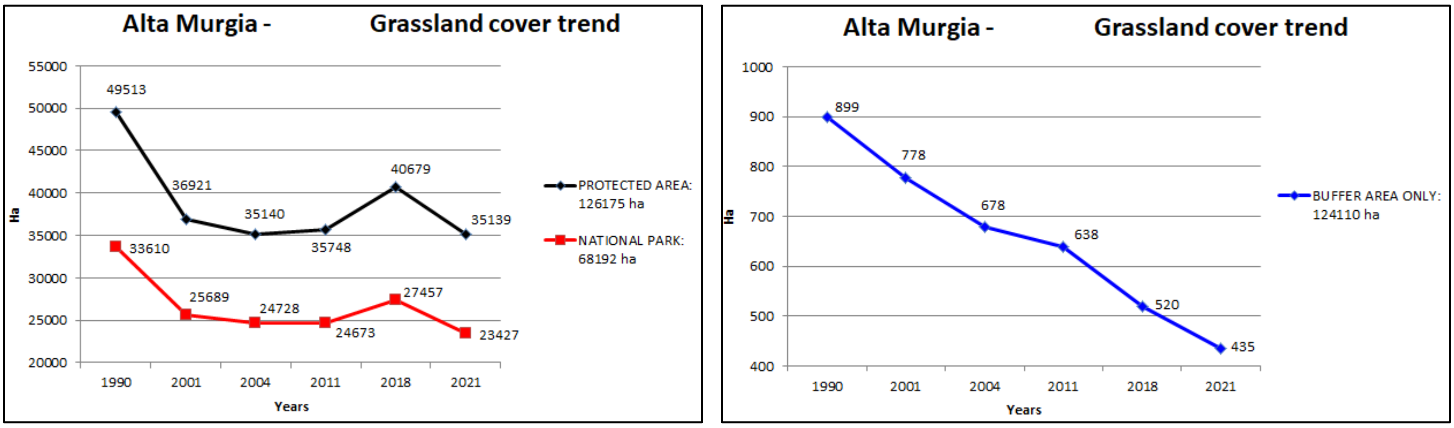

Figure 5. Plots of trend for grasslands cover vs. time.

From the analysis of the temporal trend for grasslands presence the following considerations can be evaluated:

- From 1990 to 2004, year of establishment for the National Park authority, there was a high reduction of grasslands ecosystem more pronounced during the decade from 1990 to 2001 (Figure 6);

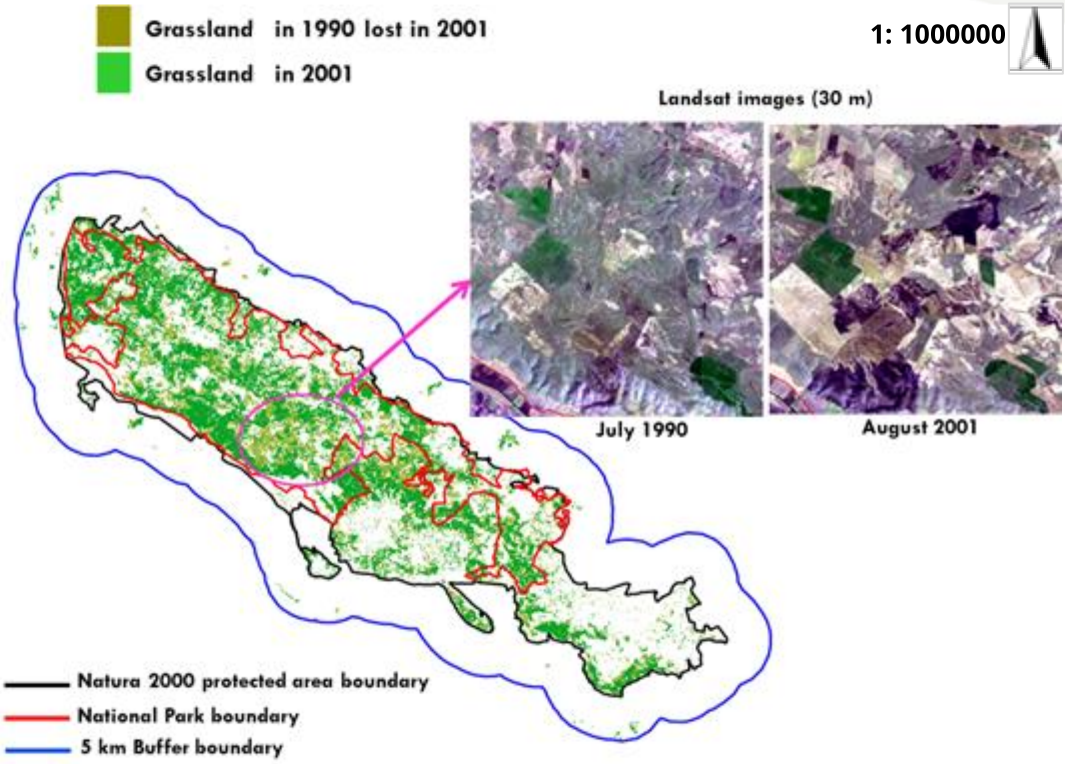

Figure 6. Grasslands mappings comparison: 1990 vs. 2001.
In the close-up natural grassland lost due to fire events can be appreciated.

- From 2004 to the present grasslands presence has remained substantially the same except for a slight increase detected in the 2018 due to grasslands regrowth after fire events. Several of these latter areas interested by grasslands regrowth became occupied by woody encroachment, thus, with a new decrease in grasslands presence;
- In the buffer area, surrounding the protected area boundary, the presence of grasslands, very poor all along, has suffered of a continuous declining temporal trend starting from 1990 to the present;
- The presence of protection and safeguard actions as those carried out by the National Park authority or the establishment of a PA seem to have been essential to preserve grasslands ecosystem degradation.

2.1.2 Burn Severity (BS) temporal trend

Methodology

For the analysis of fire-affected areas, BS mappings through the computation of NBR spectral indices (Deliverable A2.1), according to Nasery & Kalkan (2020), were computed from May to September (summer season) considering acquisition date at the beginning and the end of each month, for the same years of LC mappings. Then, for each month, the difference between the former and the latter NBRs (dNBR), so considering them as pre-fires and post-fires images, respectively, was computed to estimate the BS. In case of availability of only one image per month the difference between two successive months was considered. Later the dNBR was masked extracting those pixels corresponding to LC layers with values equal to 5, 6, 7, 8, 12 which represent grasslands, forest and burned areas excluding cultivated areas so to remove those burned areas due to agricultural practices. Finally, some thresholds were applied to identify different severity levels zones. Landsat and Sentinel-2 images (at 20 m) among those free of clouds were considered and pre-processed as described at previous subsection 2.1.1 for radiometric and geometric calibration and mosaicking. The list of images considered is reported in Table 5.

Table 5. List of satellite imagery considered for BS mappings.

Year	Acquisition date		Sensor	Spatial resolution (m)	Bands
1990	May, 4th; June, 5th;	July, 23rd; September, 25th	Landsat 5 TM	30	B4 (NIR) B7 (SWIR)
2001	May, 2nd;	August, 6th			
2004	May, 26th;	August, 30th			
2011	May, 14th;	August, 18th			
2018	April, 30th; May, 25th; July, 2nd; July, 22nd;	August, 1st; August, 31st; September, 7th; September, 22nd	Sentinel-2 A/B	20	B8A (NIR narrow) B12 (SWIR)
2021	May, 9th; May, 24th; June, 3rd; June, 28th; July, 8th;	July, 28th; August, 7th; August, 22nd; September, 14th; September, 26th			

Figure 7 shows the workflow for Burn Severity mapping.

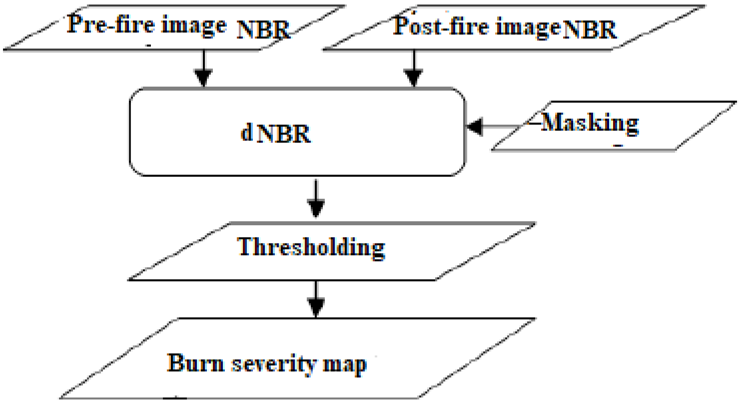

Figure 7. Workflow for BS mapping.

Results

An example of BS mapping with several close-ups compared with satellite Sentinel-2 images is shown in Figure 8.

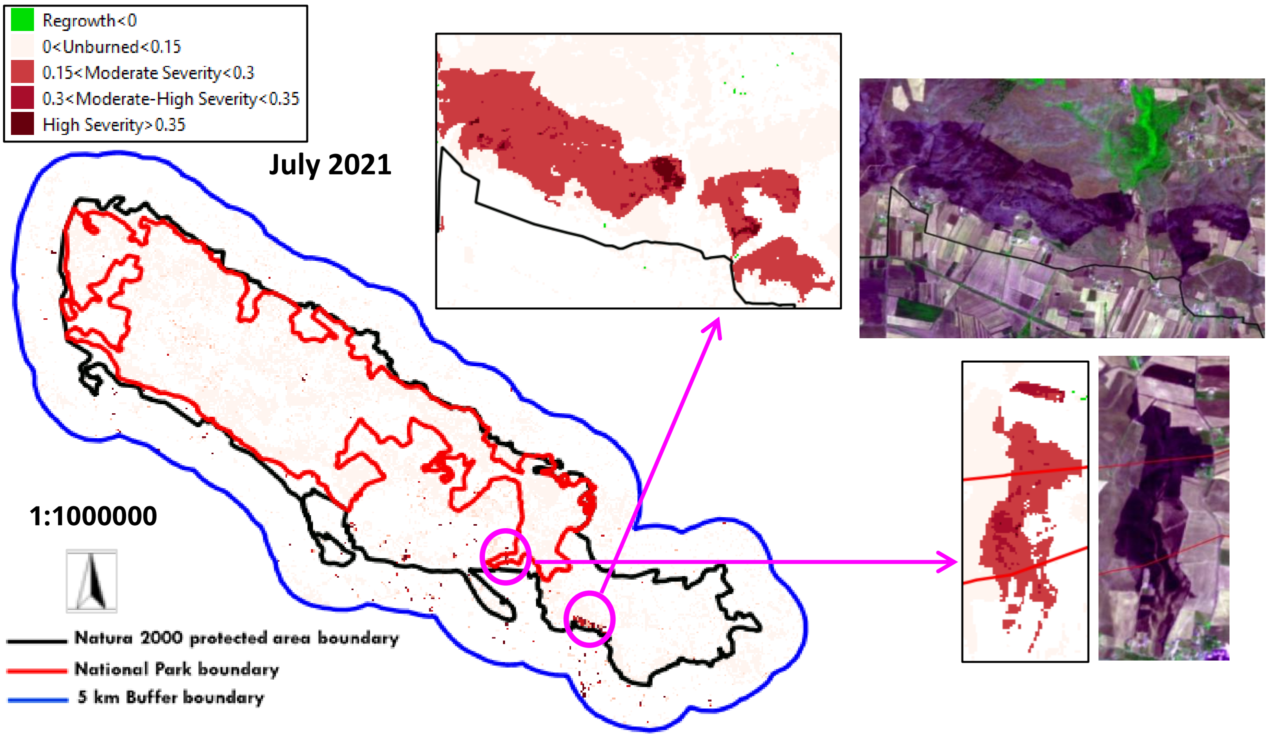

Figure 8. BS mapping for July 2021 with two close-ups in which mappings are compared to Sentinel-2 images for a qualitative validation.

From the analysis of the temporal trend for BS mappings time-series emerges:

- A high capacity of recovery by grasslands after fire events: already after several weeks burned areas cannot be detected from satellite imagery;
- Grasslands is the initial vegetation in areas where forest was burned;
- For those areas crossed by fires more times, probably more resilient not autochthone species appear (e.g., downy oak).
- Mappings by RS data can offer more accurate boundaries of burned areas than fire registry detecting also those small, burned area often not officially reported.

2.1.3 Primary Productivity (PP) temporal trend of grassland

Methodology

The analysis of PP was based on two different proxies as listed in Table 1: inter-annual time series of, both, MSAVI2 vegetation spectral index extracted from Landsat 5-7-8 and PPI based on Sentinel-2 for the period 2000-2018 and 2017-2020, respectively. The first data set was analysed with a Bayesian harmonic model, while the second one was analysed using TimeSat model based on a double exponent modelling approach (Vicario et al., 2020).

For the 2000-2018 data set, 3 summary statistics are recorded: mean value, standard deviation of the year and day of maximum. Only the day of maximum is directly comparable between the two approaches since the first one is based on the astronomical year, whereas TimeSat on the identification of the vegetative season.

For the first time series, due to the long time span, three different times were considered (2001, 2004, 2018) to identify grasslands pixels that, then, were classified in 8 categories given the 2^3 possible combinations.

All data are relative to the grasslands coverage identified on 2018 Sentinel-2 image (see subsection 2.1.1) within a 5-km buffer around the Alta Murgia National Park.

Results

Vegetation Phenology Index (MSAVI2)

The long-term inter-annual MSAVI2 time-series, extracted from Landsat data at 30 m spatial resolution for the period 2000-2018, identifies a similar trend among the different 8 classes of grassland presence over time and among the 3 quartiles for which the distribution was explored. Figure 9 shows the trend of annual statistics over the period 2000-2018 investigated.

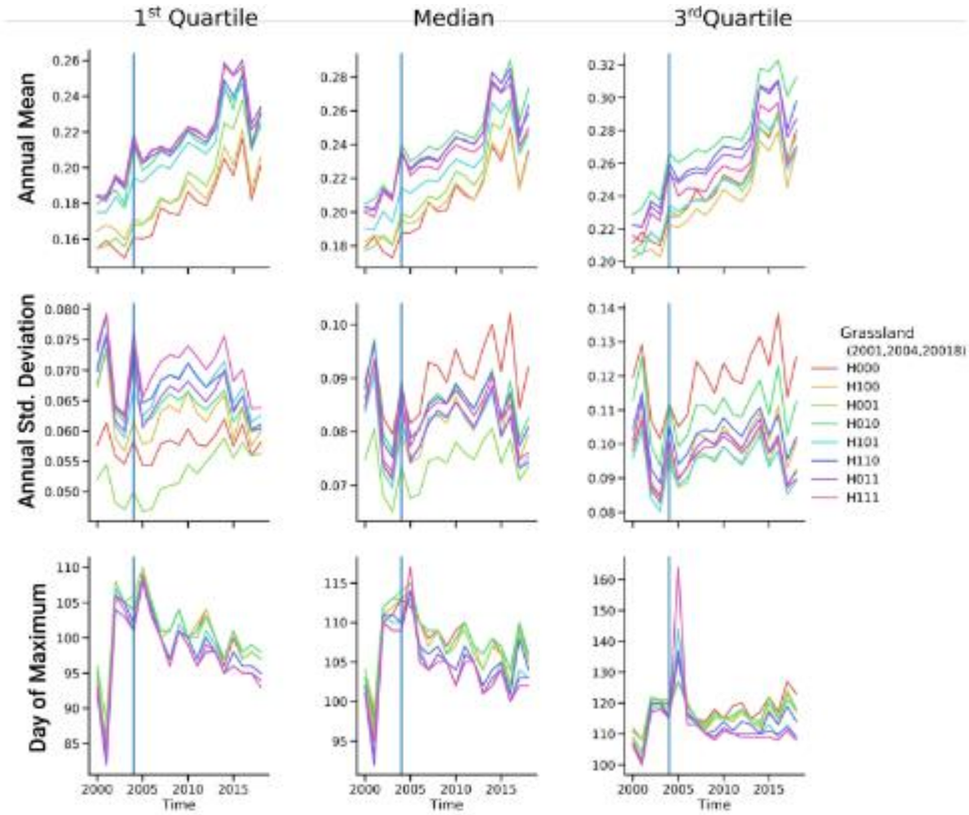

Figure 9. Trend of annual summary statistics over 2000-2018 period. The code starting with H refers to pixels that are or not considered grasslands in the 3 available time of mapping. H000 and H111 identifies the pixels that were never and always grasslands, respectively.

The following considerations can be inferred:

- The annual mean is increasing;
- The annual variation, expressed by the standard deviation, is more or less stable over time with some large single-year anomalies;
- The day of the maximum from 2002 onward has a small anticipation whereas in 2000 and 2001 very anomalous early date appear.

Plant Phenology Index (PPI)

For the period 2017-2020, the inter-annual PPI time-series from Copernicus services was considered. Data were collected from WEKEO service (https://www.wekeo.eu/), Copernicus platform, and formatted as single NetCDF (Network Common Data Form) file. Only 16 statistics (8 per season, see Table 6) were collected from the original 26 statistics (13 for each of the two vegetative seasons taken in consideration within a year) because four of them were considered not relevant (i.e., the slope of the curve in green-up and green-down for each season) and the others could be already calculated from the 16 collected as shown in Table 7.

Table 6. Name of the statistics downloaded.

Acronym	Meaning
MAXV	Value of the maximum of the season
MAXD	Day of the maximum of the season
MINV	Value of the minimum of the season
SOSV	Value of the start of the season
SOSD	Day of the start of the season
EOSV	Value of the end of the season
EOSD	Day of the end of the season
TPROD	Total productivity of the season (integral of the season using zero as base value)

Table 7. Further statistics referred to those of Table 3.1.

Statistics (acronym)	Formula
Length (LEN)	EOSD-SOSD
Amplitude (AMPL)	MAXV-MINV
Seasonal Productivity (SPROD)	TPROD-MINV*Length

The NetCDF file consists of 8 variables since the values of the first and second vegetative season were stored as dimension within the same variable. The dimension for each variable were: latitude and longitude (expressed in meter within a UTM projection), time (in years), and vegetative season (first and second).

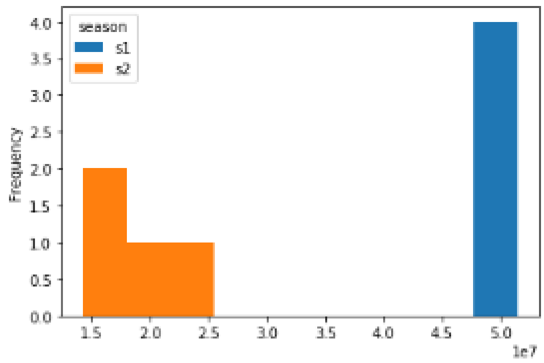

Figure 10. Number of pixels that have first and second season across 2017-2020.

From Figure 10 is possible to notice that not all pixels have data for the second vegetative season given that within the HR-VPP algorithm the second season is optional. Depending to the year, pixel with a second seasonality, within the one selected as grasslands, are between $1/_3$ and $1/_2$ of the total number of pixels.

In Figure 11 the start and the end of the vegetative season, within the pixels evaluated as grasslands coverage in 2018, are shown using 5 quantiles (0.025, 0.25, 0.5, 0.75, 0.975) as measure of the spread of the measure in each time.

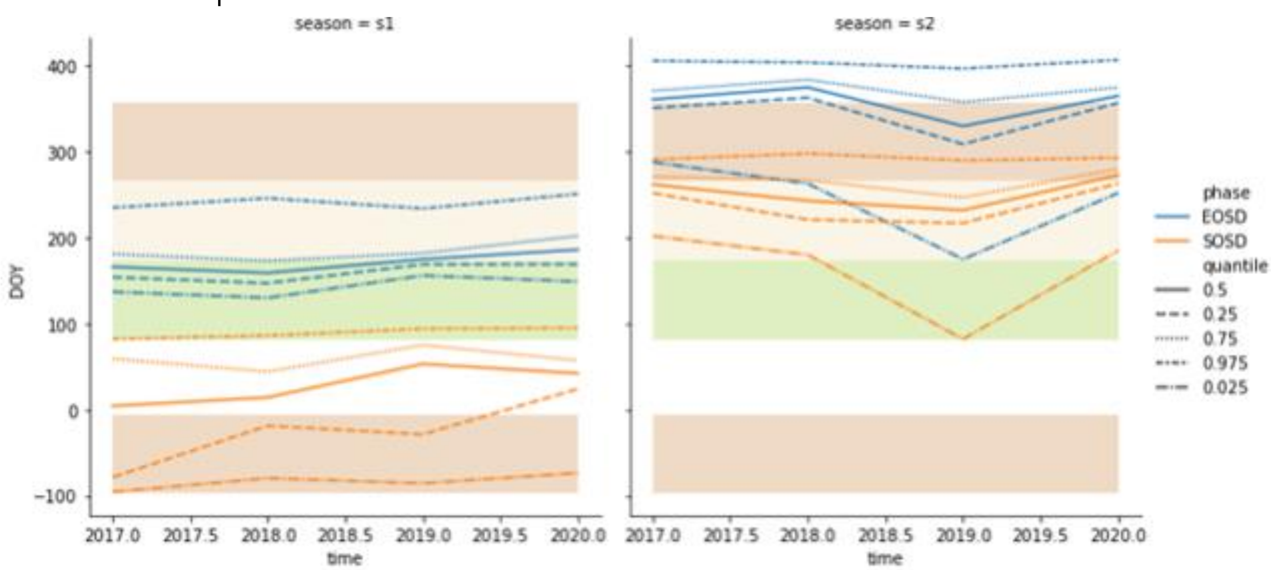

Figure 11. Start and end of season for both yearly seasons over years. Notice that DOY is expressed as day since the start of the year in consideration, for this reason its values could be negative, if season started the year before, or bigger than the year length if season ended the year after. Season is attached to the year where the maximum lays. In background the astronomical season (fall, winter, spring, summer respectively in white, green, light brown and brown).

The first season starts between the fall of the year before the start of spring, depending on the quantiles, and it ends within spring for the four first quantiles and at the end of summer for the last quantile. The secondary season covers in general from the end of summer to the mid of the next winter, except for 2019. In this year some pixels (quantile 0.025) have a secondary growth starting from the begin of spring, probably due to winter vegetative season has the maximum value in winter and not in fall that cause the switch of name between first and secondary vegetative season.

This is confirmed looking at Figure 12, where indeed the maximum value (MAXV) for the last quantile (0.975) of the secondary season is higher than primary season in 2019 only. In general (see Figure 11) the minimum value in the primary season is well detached from the maximum value while the two distributions do overlap for the secondary season.

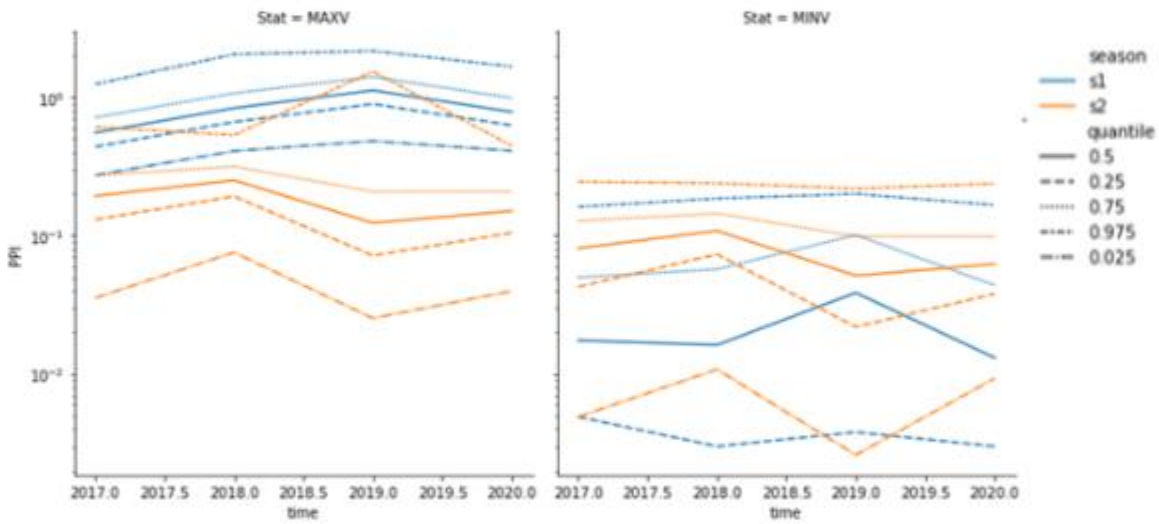

Figure 12. Value of the PPI across maximum and minimum (out of season).

Remembering the time coverage of the two vegetative seasons it seems to indicate that the majority of grasslands has only a short break somewhere in summer and for the rest is quite active, although secondary season is not very different from background. This consideration can be confirmed looking at the amplitude (Figure 13 on the left) where the sum of the median length of first and second season is 220 days, while for quantile 0.75 the sum of the length is about 320 days.

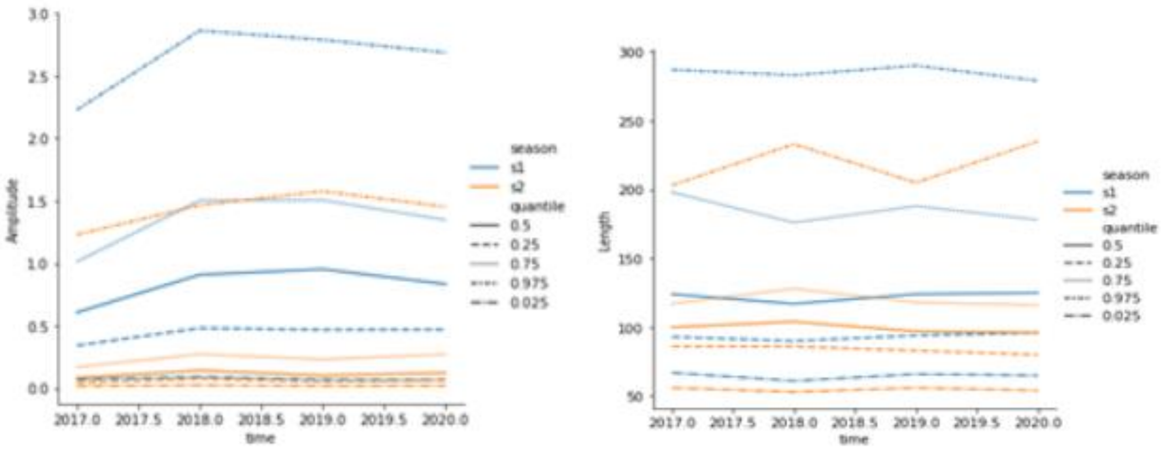

Figure 13. Length and amplitude of season across year and seasons.

Within the HR-VPP framework is always complex to define the best summary statistics to show space variability. Looking at productivity as a main ecosystem function, it becomes interesting to look at TPROD that is the integral of the value of the vegetation index PPI across a vegetative season. To get a more general overview, TPROD was summed in each pixel across season and then averaged across the 4 years of the HR-VPP data set. Limiting the observation to grasslands, the results in Figure 14 were obtained.

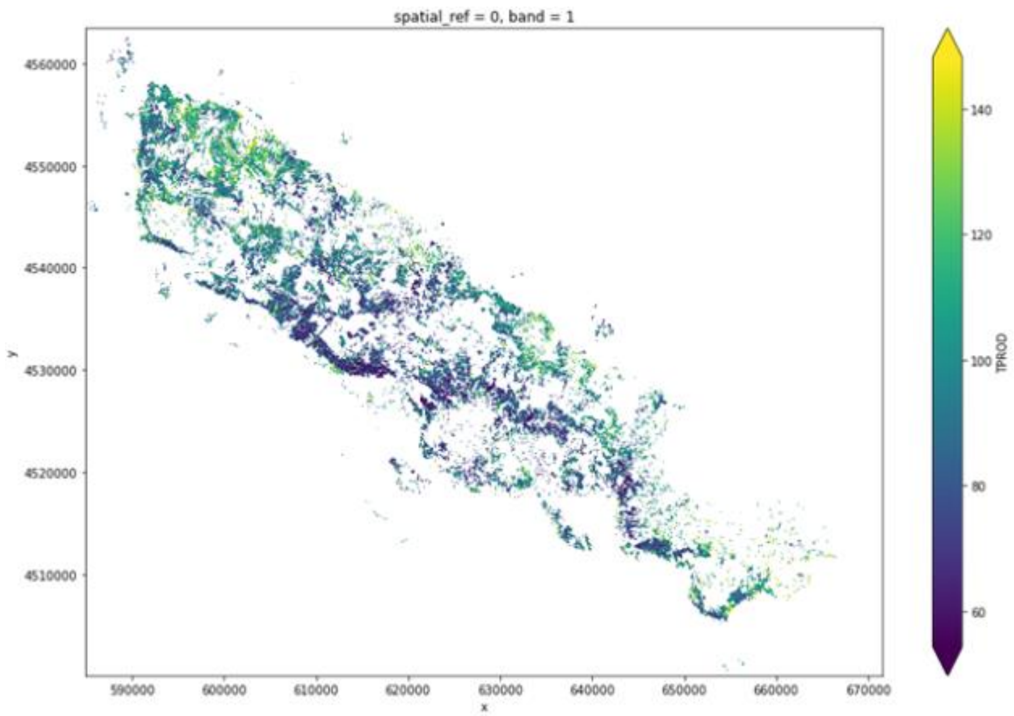

Figure 14. Map of the integral of PPI across seasons averaged across time.

It is possible to notice that:

- Grasslands has higher productivity on the side of the highlands that look towards Adriatic Sea;
- The central plateau is less productive.

2.1.4 Standardized Precipitation Evapotranspiration Index (SPEI) temporal trend

Methodology

The evaluation of SPEI for Alta Murgia National Park captures the main impact that the increase in temperature has on water availability for vegetation and it is used to identify and monitor the phenomena of dryness by evaluating two different time scales, monthly and quarterly. This index is based on the ratio between precipitation and potential evapotranspiration (Hargreaves & Zohrab, 1985; McMahon et al., 2013; Chad et al., 2019). The climate data used as input come from three weather stations within the park (Figure 15): data from stations of Minervino Murge and Mercadante, cover the time range between 2002 and 2020; data from the station of Masseria Modesti covers the time range between 2010 and 2020. The extracted data were average temperature, minimum temperature, maximum temperature, and precipitation.

Figure 15. Location of the weather stations of the Alta Murgia National Park (marked by a point). In yellow the Park’s boundary and in red the N2K boundary.

Results

The dryness trends are reported for the Mercadante and Minervino Murge weather stations with a monthly integration (Figure 16). Analyzing and comparing the two weather stations with the longest time series it is possible to observe that SPEI trend is associated with precipitation events. From the Mercadante control unit results that precipitation has decreased starting from the end of 2012 and aridity has increased, especially in the hottest months. For both control units, on average, 21.5% of the daily data show moderate aridity, of which 14% for Mercadante and 12.5% for Minervino Murge show phenomena of severe aridity. From the monthly integration, it appears that from June to August the area is affected by strong aridity; in the last 10 years starting from the summer of 2011, it also touches average monthly values below -2 for the Mercadante station classifying as "extremely arid" area. In Minervino Murge weather station, the phenomena of extreme aridity seem to have been triggered already since 2007.

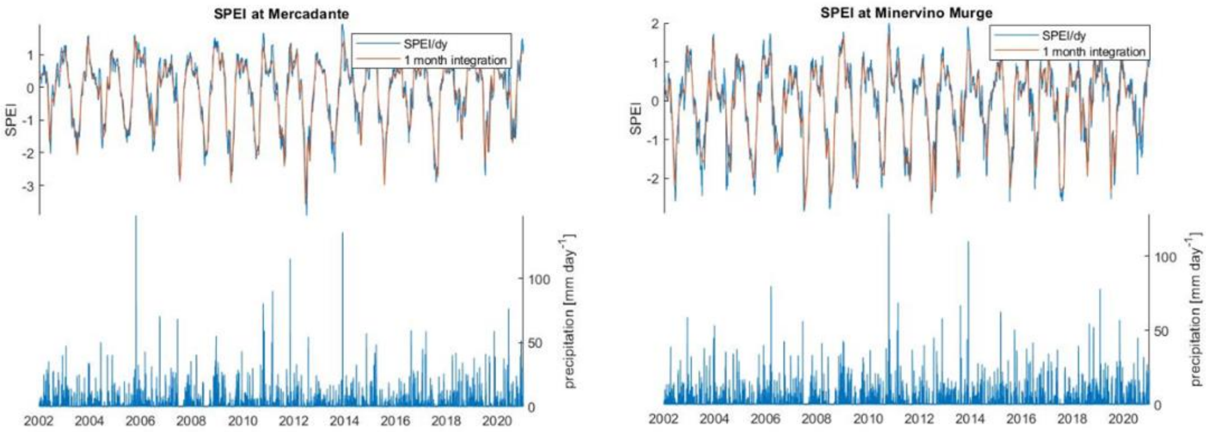

MERCADANTE

MINERVINO

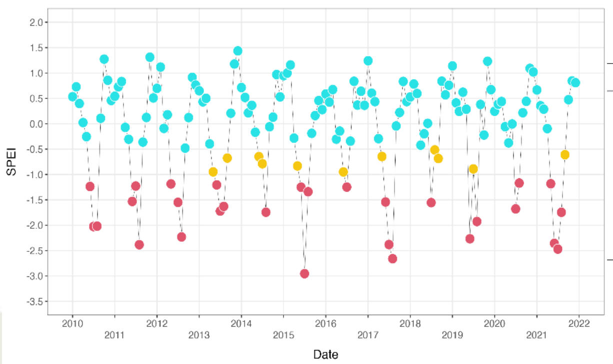

Categorization	SPEI values
Extremely wet	SPEI ≥ 2
Severely wet	1.5 ≤ SPEI < 2
Moderately wet	1 ≤ SPEI < 1.5
Mildly wet	0.5 ≤ SPEI < 1
Normal	−0.5 ≤ SPEI ≤ 0.5
Mild drought	−1 < SPEI < −0.5
Moderate drought	−1.5 < SPEI ≤ −1
Severe drought	−2 < SPEI ≤ −1.5
Extreme drought	SPEI ≤ −2

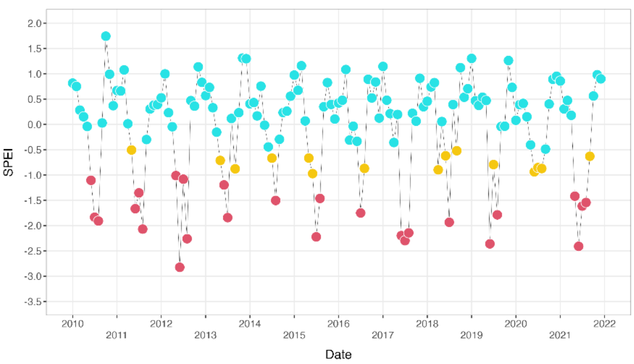

Figure 16. Daily and Monthly integration of SPEI for weather station of Mercadante and Minervino Murge compared with the respective rainfall distributions.

The SPEI with quarterly integration (Figure 17) confirms that the two central quarters of the year, in conjunction with the vegetative period, result the driest, especially starting from 2015 for Mercadante (Figure 17-left). It can be noted that they are not counterbalanced by exceedingly prolonged periods of absence of aridity; even where the SPEI does not reach negative values, it always stands at values below 1, therefore, classified as "near normal/mild drought" rarely higher than 1 and therefore never "moderately wet" suggesting that the availability of precipitation is never so high. Slightly different seems to be the situation of Minervino Murge (Figure 17-right) where, as already stated, the aridity is strong since 2007 but balanced by values of good water availability in the less arid months due to more frequent rainfall until 2015 (values above 1).

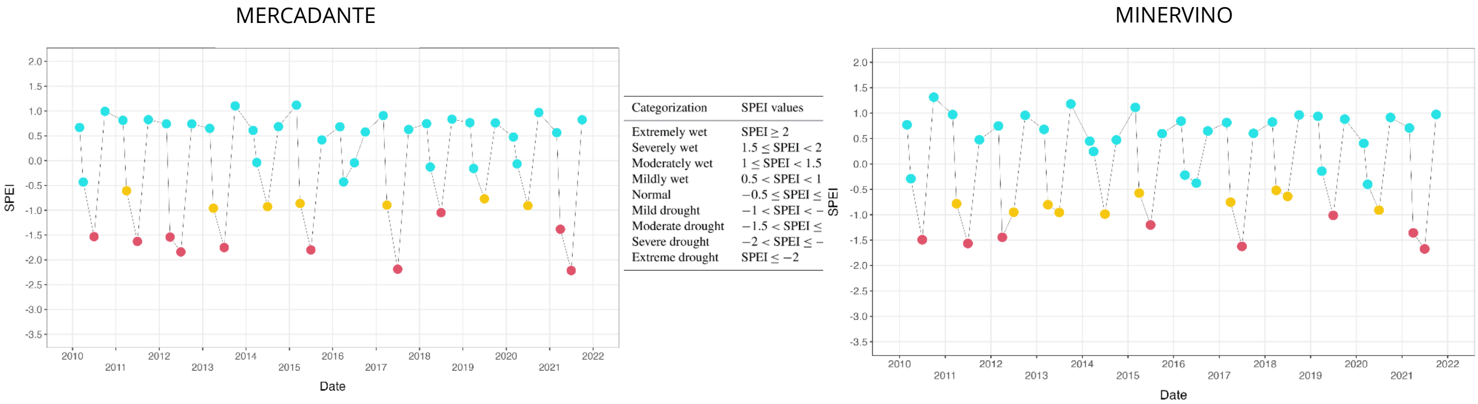

Figure 17. SPEI trends with Quarterly integration calculated by Minervino Murge and Mercadante weather stations.

Concerning Masseria Modesti control unit, the climatic series available is less extensive as it goes from 2010 to 2020, but the trend is remarkably similar to that of Mercadante and Minervino Murge and gives us a clear view of the aridity phenomena that affect this area. In fact, from the entire series, it emerges that 20.5% of the values show moderate aridity 11% of which show phenomena of severe aridity, both for the monthly and quarterly integration (Figure 18), confirming thus strong aridity, especially in the summer months that in 2012 and 2015 and 2017 reach values between -2 and -3 (extreme aridity). Therefore, from the quarterly integration, it is possible to note that starting from 2015 there is no evidence that during the non-arid months they can balance the summer aridity defined by extremely high SPEI values.

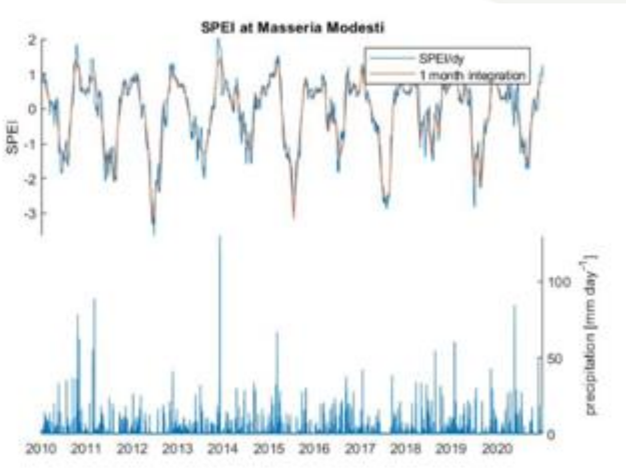

MODESTI

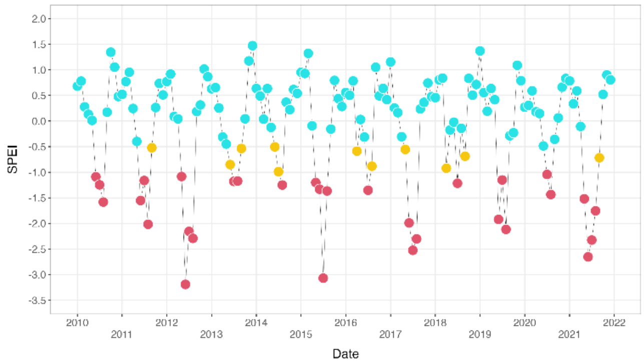

Categorization	SPEI values
Extremely wet	SPEI ≥ 2
Severely wet	1.5 ≤ SPEI < 2
Moderately wet	1 ≤ SPEI < 1.5
Mildly wet	0.5 < SPEI < 1
Normal	−0.5 ≤ SPEI ≤ 0.5
Mild drought	−1 < SPEI < −0.5
Moderate drought	−1.5 < SPEI ≤ −1
Severe drought	−2 < SPEI ≤ −1.5
Extreme drought	SPEI ≤ −2

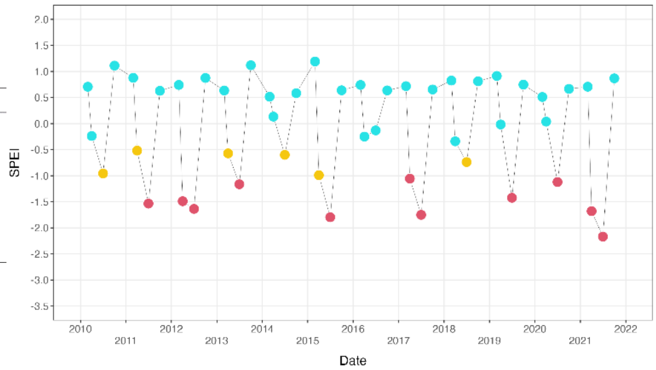

(a) (b)

Figure 18. Daily, Monthly and Quarterly integration of SPEI for weather station of Masseria Modesti compared with the rainfall distribution.

2.1.5 Soil Organic Carbon (SOC) temporal trend

Methodology

The extraction of SOC temporal trend was performed by using *Trends.Earth* plugin within the open- source QGIS tool according to Giuliani et al. (2020). As reference SOC map the most recent (update in June 2016) and improved version of *SoilGrids* (Hengl et al., 2017) product was considered. It was produced at 250 m spatial resolution and assessed for organic carbon and other soil properties available under the Open Data Base License. This product was primarily derived from MODIS satellite land products, SRTM DEM derivatives, climatic images and global landform and lithology maps by a machine learning supervised approach. Two different LC mappings were needed related each one to the years to be compared and, first, reclassified in

7 main classes: cropland, tree-covered, grassland, artificial, water body, other land, no data. Then, according to specific coefficients related to the type of LC transition, a SOC map was produced for each LC map and, lastly, the SOC temporal trend mapping between the two years considered, for the whole PA, was computed.

For SOC losses greater than 10% degradation was considered.

Results

Table 8 and Figure 19 shows the SOC temporal trend mappings produced for the period before and after 2004 when National Park was instituted.

Table 8. List of periods considered for the SOC temporal trend mappings and results. The percentage is related to the whole N2K PA (126175 ha).

Period	Spatial resolution (m)	Objectives	Degradation	Improvement
1990-2004	30	Before National Park institution (2004)	2348 ha (1.86%)	5090 ha (4.00%)
2004-2018		After National Park institution (2004)	1059 ha (0.84%)	4515 ha (3.60%)

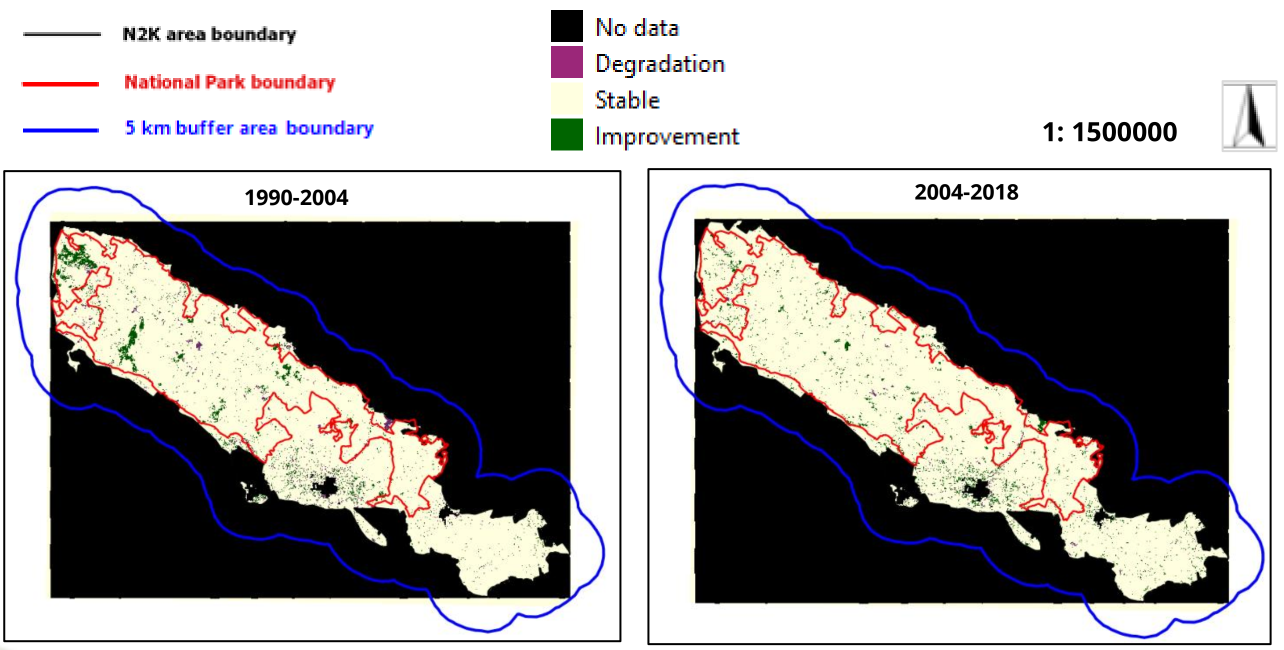

Figure 19. SOC degradation mappings produced for Alta Murgia.

The following considerations can be derived:

- In both period improvement can be appreciated mainly due to the grasslands regrowth on burned areas at time T_1;
- After the Alta Murgia National Park establishment SOC degradation was reduced;

2.1.6 SDG 15.3.1 computation and land degradation mapping

Methodology

According to UNCCD guidelines (Sims et al., 2021), SDG 15.3.1 indicator is obtained by considering 3 sub-indicators: LC trend, PP trend, and SOC stocks trend. In this study additional sub-indicators related to the pressures and threats affecting each site was integrated.

In the computation of SDG 15.3.1 indicator, according to UNCCD guidelines (Sims et al., 2021), the following steps were addressed:

- for each sub-indicator the temporal trend was computed with a 3-values output such as *Degradation, Improvement, Stable*;
- the final SDG 15.3.1 mapping was obtained combining all sub-indicators according to the principle "*one out, all out*" (1OAO) such as an OR combination where:
  - ✓ as long as one of sub-indicators has Degradation value, the result will be Degradation;
  - ✓ in case of sub-indicators have only Improvement or Stable values, the results will be Improvement, as reported in Figure 20;

Aggregating SDG 15.3.1 sub-indicators - 1OAO

Land Productivity	Land Cover	SOC	SDG 15.3.1
Improving	Improving	Improving	Improving
Improving	Improving	Stable	Improving
Improving	Improving	Declining	Declining
Improving	Stable	Improving	Improving
Improving	Stable	Stable	Improving
Improving	Stable	Declining	Declining
Improving	Declining	Improving	Declining
Improving	Declining	Stable	Declining
Improving	Declining	Declining	Declining
Stable	Improving	Improving	Improving
Stable	Improving	Stable	Improving
Stable	Improving	Declining	Declining
Stable	Stable	Improving	Improving
Stable	Stable	Stable	Stable
Stable	Stable	Declining	Declining
Stable	Declining	Improving	Declining
Stable	Declining	Stable	Declining
Stable	Declining	Declining	Declining
Declining	Improving	Improving	Declining
Declining	Improving	Stable	Declining
Declining	Improving	Declining	Declining
Declining	Stable	Improving	Declining
Declining	Stable	Stable	Declining
Declining	Stable	Declining	Declining
Declining	Declining	Improving	Declining
Declining	Declining	Stable	Declining
Declining	Declining	Declining	Declining

Figure 20. Possible values of the 3 main sub-indicators to be aggregated for SDG 15.3.1 indicator computation.

- for SDG 15.3.1 percentage computation, the total proportion of grasslands that is degraded over total grasslands area was computed, according to (Sims et al., 2021, page 9), as:

$$P_n = \frac{A(Degraded)_n}{A(\text{Total})}$$

where:

P_n is the proportion of grasslands that is degraded at time t_n since the baseline period t_0=1990;

$A(Degraded)_n$ is the total area degraded at t_n computed as:

$$A(\text{Degraded})_n = A(\text{Recent Degraded})_n + A(\text{Persistent Degraded})_n - A(\text{Improvement})_n$$

In particular the term $A(\text{Persistent Degraded})_n$ implies the analysis of a period prior to the one being analysed.

In details the specific choices for Alta Murgia site are the following:

- different temporal ranges to be monitored, according to the main meaningful events in the site, were identified such as: 1990-2004 (this latter as year of National Park institution) and 2004-2018;
- the spatial scale of 30-meters was chosen according to the need of local scale investigation and spatial resolution of Landsat images which represent the main satellite data analysed;
- only the trend for Grasslands (the main threatened ecosystem) LC was considered;
- for the additional sub-indicators, the following range values were considered:
    - ✓ BS mapping: all the pixel with values greater than 0.15 or 0.25 for the case of July or August as post-fire image, respectively, for each year, were considered degraded (burned areas). Respect to grasslands cover changes the use of BS can allow to take into account for those burn areas at time T_1 which are not covered by grasslands regrowth at time T_2 so representing "Persistent Degraded" as discussed above;
- A(Total) is the total grasslands area at t_0=1990.

PP trend is itself split in other three sub-indicators called: Trajectory, Performance and State. To estimate PP in Alta Murgia site we used Landsat data, given that it has a large time extent and a better spatial resolution than MODIS proposed by UNCCD as source. We choose, as PP indicator, MSAVI2 that allows a good discrimination between bare soil and vegetation, which characterize the land pattern in the arid upland of Alta Murgia.

Trajectory was evaluated with Mann-Kendal Trend test with critical value 0.05 and two tails, to obtain a tree valued image with zero for no significant change in trend, 1 for significant increase and –1 significant decrease. As reference time we took the period 2000 to 2004. This reference time was chosen because this period is the one with less change in LC per year than any other in Figure 4. As analysis we chose the 2004-2018 to see the effect of the onset of the National Park.

From figure 9 we expect that Trajectory index should include several pixels with an increasing trend but using the stringent critical value of 0.05 this is not true. Infact, only not giving assuming that the null hypothesis is no trend, using a critical value of 0.5, then, we find that most pixels have an increasing trend. In any case the number of pixels with decreasing trend stay low and constant (2.7% of the total grassland).

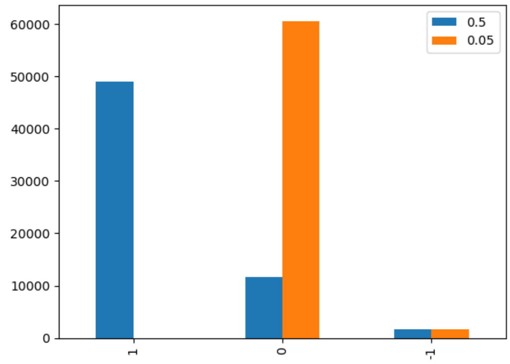

Figure 21. The number of hectares that are flagged with increasing trend (1), no trend (0) or decreasing one (-1) using the two different critical values (0.5 and 0.05).

The State sub-indicator is defined as the difference between the mean reference time value with the mean analysis period time. The discretize and make the indicator more robust, this difference is quantized identifying the 10 quantile that describes the full reference distribution and assigning the two mean values at each bins. More than two bins of difference are considered that the area is not stable.

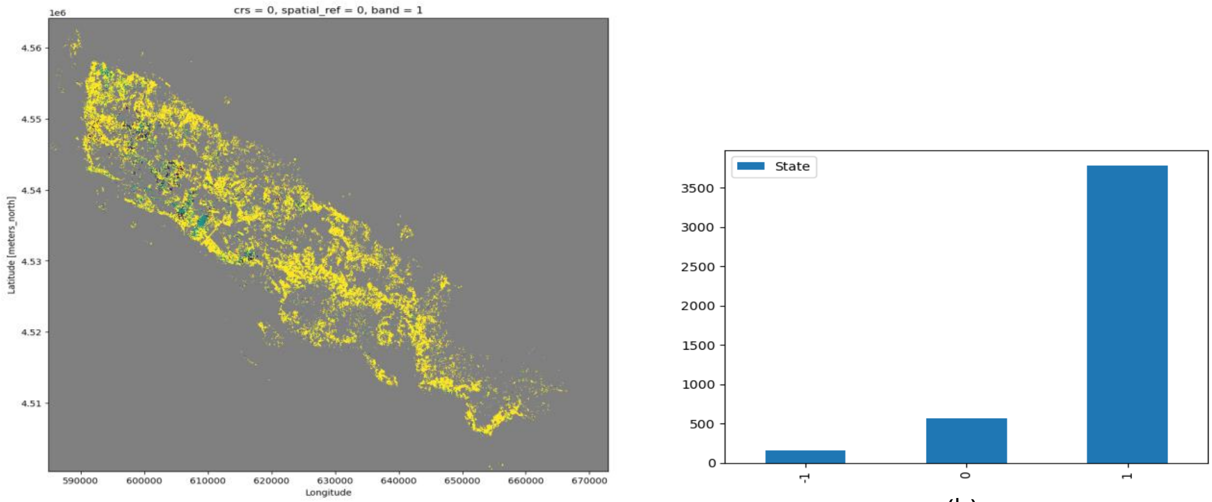

(a) (b)

Figure 22. (a) State sub-indicator over the period 2004-2018 using as reference 2000-2004. In yellow the state is increasing, green is stable, while blue is decreasing. (b) In the graph, the histogram shows the results in hectares.

The Performance sub-indicator looks at the ratio between mean observed value in a pixel and a high value (90 percentile) of the same kind of LC. We used grasslands cover of 2004 and 2018 to produce 3 classes of grasslands that had the same history. For each such a class we applied the performance pipeline. The grasslands "10", grasslands in 2004 but not in 2018, is the one with slightly larger PPI value of 90th% (0.34 versus 0.32 for the other two classes). As for the other sub-indicator, degraded land is very small.

Table 9. Hectares that have stable (0) or degrading (-1) for each grassland habitat with different history

	01	10	11
0	1109.15	587.69	3365.28
-1	16.85	18.51	8.39

Results

The degradation mappings for the 2 periods considered are reported hereafter.

1. For the period 1990-2004 the degradation mapping is shown in Figure 23:

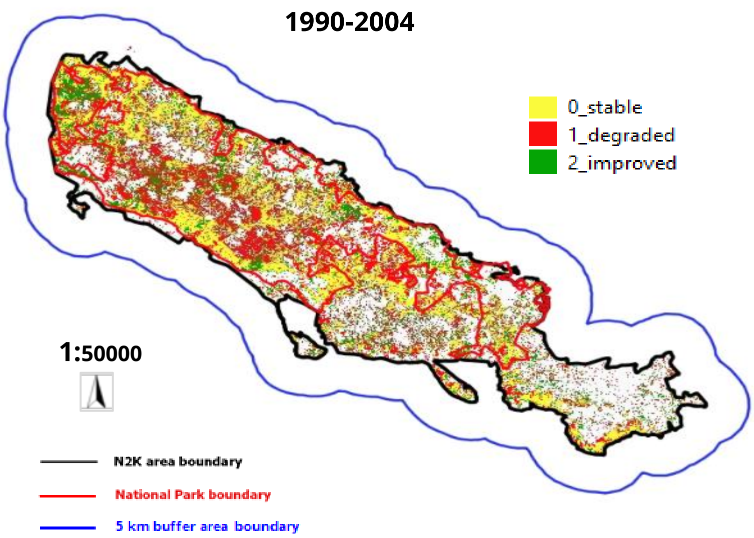

Figure 23. Land degradation mapping for Alta Murgia PA for the period 1990-2004.

For this period the PP sub-indicator was considered only for 2000-2004 for computational complexity.

The resulting SDG 15.3.1 indicator percentage was equal to 34.78%.

2. For the period 2004-2018 the degradation mapping is shown in Figure 24:

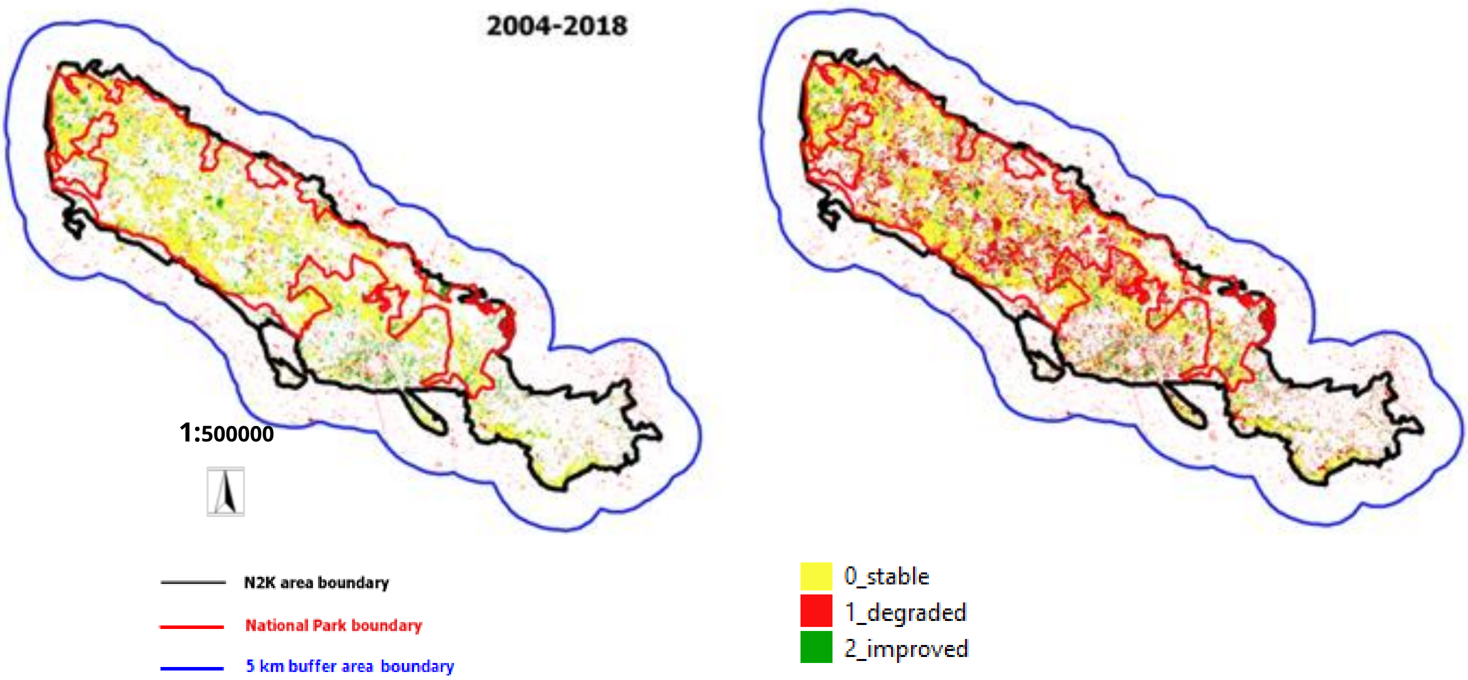

(a) (b)

Figure 24. LD mapping for Alta Murgia PA for the period 2004-2018. (a) Mapping without “Persistent Degraded”; (b) Mapping with “Persistent Degraded”.

The resulting SDG 15.3.1 indicator percentage was equal to: 15.63% for Figure 24.a and 33.56% for Figure 24.b.

SPEI sub-indicator should be integrated into the SDG 15.3.1 indicator computation to take into account the contribution of drought conditions (i.e., extreme drought conditions for SPEI < -1.5) in terms of, for example, number of monthly values with drought conditions for year. Due to the absence of a network of weather stations across the territory that would allow for any data spatialisation, (indeed the availability of only 3 weather stations results not enough), remains to be considered the presence of additional drought conditions, according to SPEI analysis at section 2.1.4, which could contribute to complete the degradation framework provided by the SDG 15.3.1 indicator. This considerations can be considered for all the study sites.

2.2 Palo Laziale (Italy)

The study site "Bosco di Palo Laziale" (SAC IT6030022), shown in Figure 25, is characterized by a Mediterranean coastal forest ecosystem. During summer, high temperatures and low precipitations give rise to a dry period and negative soil water balance due to high evapotranspiration.

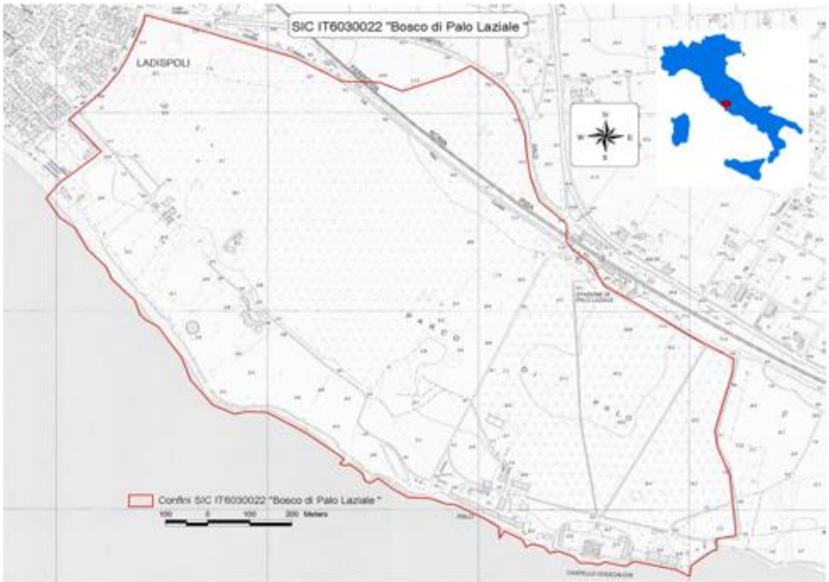

Figure 25. Boundary of N2K site Bosco di Palo Laziale (Ladispoli), Rome, Italy.

The area hosts one of the last remaining patches of an ancient Mediterranean floodplain forest of oaks and ash trees forming 91M0, 9340, 91B0 habitat types (Annex I, Habitats Directive 92/43/EEC) that, from its pristine coverover the entire coastland of central Italy, was progressively reduced over the centuries by reclamation and deforestation activities.

Over the last three decades, the area has been increasingly exposed to significant changes in the climate regimes that altered the balanced fluctuation of precipitation and drought. As a result, due to constantly increasing temperatures and extreme fluctuations of the rainfalls, the site has been affected by a tremendous case of aridity, especially at the soil level, which also turned into an increasing vulnerability of the forest stands to direct and indirect disturbances, including bush encroachment, over-competition for trophic resources, extreme weather events, fires and fungal diseases. This has generated a severe case of forest dieback in Palo Laziale causing widespread mortality in trees at the end of summer 2003, about 40% of the adult trees were found died – and high canopy loss (about 80%).

From 2018, a set of restoration interventions have been carried out on the site in the framework of the EU-funded project LIFE PRIMED (LIFE17 NAT/GR/000511). At that time, the forest looked more like a savanna than a floodplain oak woodland, with only few stands having the original canopy density and the survived trees showing high senescence and low seed production. Most of the topsoil freed by the dominant tree layer was occupied by thorny shrubs (e.g., *Rubus spp.*), with only limited accessible areas available for new saplings to grow. There was forest regeneration (plants at least three years old), but the shrubs were suffocated the growing seedlings. Such an encroachment strongly inhibited forest recovery and threatened the area occupied by other important habitat types such as the Mediterranean temporary ponds, (3170*). Such an invasion caused burial of the shallow ponds, decreasing photosynthesis sunlight and limiting gas exchange between the water surface and the atmosphere. Thus, selective trimming treatments were carried out annually on the site over three consecutive years to unleash oak and ash tree seedlings from the understory. The intervention also benefited fire prevention by recovering former fire-cutting strips and pathways for fire-fighting vehicles.

Figure 26. Manual and machinery field operations to trim encroaching shrubs out from Palo Laziale's topsoil.

The following RS indices and sub-indicators, reported in Table 10, were extracted to investigate all the pressures described above. Due to the small size of the site (< 50 ha), archive VHR satellite images were purchased, one image per year from 2002 to 2021: the only available imagery were nearly acquired mainly during summer season.

Table 10. Indices and sub-indicators selected for Palo Laziale study site.

Sub-indicators		Sensor	Spatial resolution (m)	Spatial frame	Temporal frame
LAND COVER MAP		Pleiades	2	N2K +1 km buffer	2021
VEGETATION STATUS	**VEGETATION INDEX (NDVI/MSAVI2)**	Quickbird	2.4		2002;2003;2005; 2008;2009
		Pleiades	2		2014;2015;2016; 2018;2020;2021
PRIMARY PRODUCTIVITY	**PLANT PHENOLOGY INDEX (PPI)**	Sentinel-2	10		2017-2020
STANDARDIZED PRECIPITATION EVAPOTRANSPIRATION INDEX (SPEI)		1 meteo station			1951-2020
SOC		Soilgrids+ LC maps	2		2002-2014; 2014-2021

2.2.1 LC temporal trend

LC mapping for 2021

Methodology

Table 11 presents the data set of Pléiades images (RGB-NIR, 2 m spatial resolution) used to produce the LC map of Palo Laziale site for 2021. The input images were pre-processed for converting the Digital Number values in Top-of-Atmosphere reflectance and then geometrically co-registered.

Table 11. List of VHR images considered for 2021 for Palo Laziale site. Information on the flush period is given.

Sensor	Date of Acquisition for 2021	Flush Period
Pleiades	January, 11th	Pre-Peak of Biomass (PrePoB)
	April, 4th	Peak of Biomass (PoB)
	July, 9th	Dry Season
	October, 9th	Post-Peak of Biomass (PostPoB)

A Knowledge-driven object-based approach has been used to extract LC for the site in FAO-LCCS2 taxonomy. This method includes two different steps: a preliminary segmentation and a successive classification (Adamo et al., 2020; 2016; 2014). The hierarchical scheme adopted by the FAO–LCCS2 taxonomy was implemented for class discrimination.

The classification in LCCS has two main phases: (1) the Dichotomous phase and (2) the Modular-Hierarchical phase. The Dichotomous phase includes three classification levels as shown in Figure 27 (Tomaselli et al., 2013).

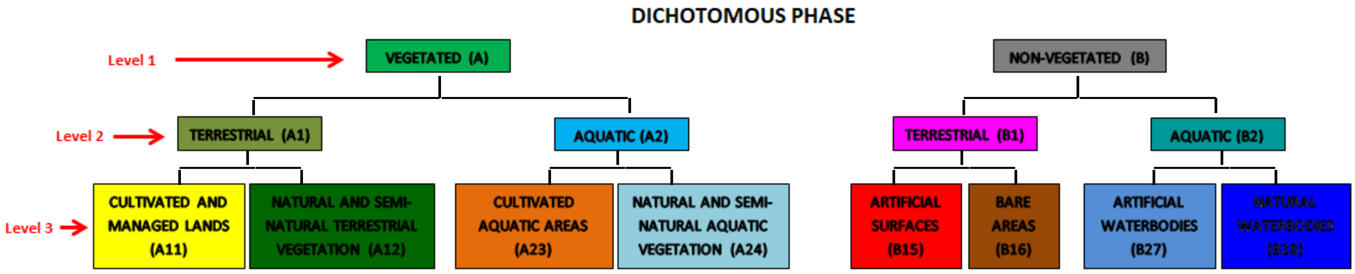

Figure 27. FAO-LCCS2 dichotomous phase.

The Modular-Hierarchical phase combines of a predefined set of classifiers to provide more detailed land cover classes (Level 4).

The eCognition tool (Trimble, 2019) spectral differences algorithm was applied for the segmentation step. This algorithm merges neighbour pixels that fall within a user-defined maximum spectral difference. The spectral difference between adjacent pixels is calculated by considering their spectral values in the RGB-NIR bands of both the PostPoB and PrePoB images. The maximum spectral difference was set to 0.019 by a trial-and-error procedure. The main criteria for such a trial-error process were to recognize some of the finest elements (e.g., tree crowns) of the landscape, without over-segmenting the scene. Thus, visual interpretation of the different output segmented scenes addressed the parameter selection.

Then, LCCS2 classifiers were implemented in the classification algorithm developed for satellite image analysis along with expert knowledge rules from ecologists related to class description. First, Vegetated or Not-Vegetated objects (LCCS2 Level 1) and then, for each one, Terrestrial or Aquatic areas, were recognized (LCCS2 Level 2) (see Figure 27).

Then class descriptions provided by ecologists were used to go through the LCCS2 scheme including the Class phenology, Water Seasonality and Agricultural Practices. Vegetated class discrimination depends on different periods of biomass and plant development. Agricultural class discrimination is based on the periodicity of agricultural practices (i.e., ploughing, harvesting/mowing). Aquatic class discrimination requires water seasonality information.

Expert knowledge exploitation was carried out by the implementation of if-then rules set based on selected spectral indices and context-sensitive features.

The set of selected spectral indices includes: 1) NDVI, 2) Blue/NIR Ratio (BNR), which performs well in discriminating water covered pixels (Morris et al., 2010); 3) Brightness index, which was proven to be effective in identifying non-vegetated areas.

Concerning context-sensitive features, the texture first order entropy (occurrence measure) (Anys et al., 1994), from the green band of the PostPoB image was used to discriminate herbaceous and woody vegetation. The window size used to compute entropy was selected to match the scale of heterogeneity related to variations in vegetation height, distribution and structure.

Results

Figure 28 and Table 12 show the LC map and its related legend, respectively.

Table 12. LC classes legend according to FAO-LCCS2 taxonomy

	Description	Code
	B_NotVegetated (road, bare soil, sand)	B
	Unclassified	
	Artificial or Natural Waterbodies	B27 OR B28
	Shadow	
	Natural or Artificial Aquatic Vegetation	A24 OR A23
	Natural Terrestrial Vegetation/Herbaceous.Graminoids or Cultivated Land/Herbaceous	A12/A2.A6 OR A11/A3
	Natural Terrestrial Vegetation/Herbaceous.Forbs	A12/A2.A5
	Natural Terrestrial or Aquatic Vegetation/Trees.Broadleaved.Evergreen	A12 OR A24/A3.D1.E1
	Artificial Surfaces_Buildings	B15/A13
	Natural Terrestrial or Aquatic Vegetation/Trees.Broadleaved.Deciduous	A12 OR A24/A3.D1.E2
	Natural Aquatic Vegetation/Herbaceous.Graminoids	A24/A2.A6
	Road or Wet Sand	B15/A7 OR B16

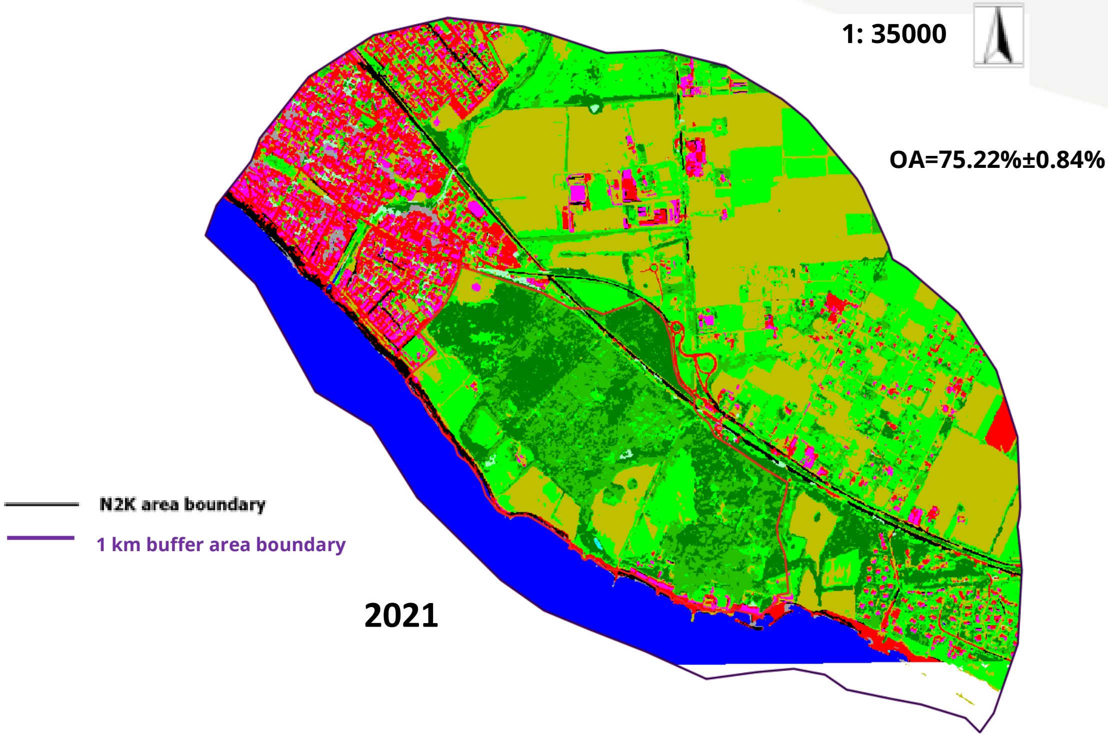

Figure 28. FAO-LCCS2 Modular-Hierarchical phase.

Spectral categories mapping temporal trend

Methodology

Due to the availability of only one annual archive image at VHR per year from 2002, NDVI was extracted from Pleiades and Quickbird data to identify spectral categories of vegetation.

The aim was to extract vegetation coverage from 2021 LC mapping and analyse degradation in vegetation going back in time using the summertime series.

The VHR images were acquired in summer season as shown in Table 13.

Table 13. List of VHR imagery considered for Palo Laziale site.

Sensor	Date of Acquisition
Quickbird	June 26^{th}, 2002
	July 12^{th}, 2003

	June 3rd, 2005
	July 9th, 2008
	July 30th, 2009
Pleiades	July 6th, 2014
	June 3rd, 2015
	August 7th, 2016
	July 7th, 2018
	June 26th, 2002
	January, 23rd; April, 4th July, 5th; October, 5th 2020
	January, 11th; April, 4th July, 9th; October, 9th 2021

NDVI always ranges from -1 to +1: for negative values, it is likely water. On the other hand, NDVI values close to +1mainly stands for dense green leaves. In case of NDVI close to zero, there are likely no green leaves, and it could even be an urbanized area. NDVI is an index of vegetation "greenness," sensitive to the chlorophyll content of vegetation, therefore, indicative of vegetation health, which can be considered vigorous for NDVI values not less than 0.4. The legend associated with the different thresholding applied is reported in Table 14 (https://www.agricolus.com/en/vegetation-indices-ndvi-ndmi/).

Table 14. Thresholding applied to NDVI value

Thresholds	Description
0,1≤x>0,2	Very Poor Vegetated
0,2≤x>0,4	Poor Vegetated
0,4≤x>0,6	Medium Vegetated
0,6≤x>0,8	Strong Vegetated
≥0,8	Very Strong Vegetated

In particular, 4 sub-areas were identified within the wood as reported in Figure 29.

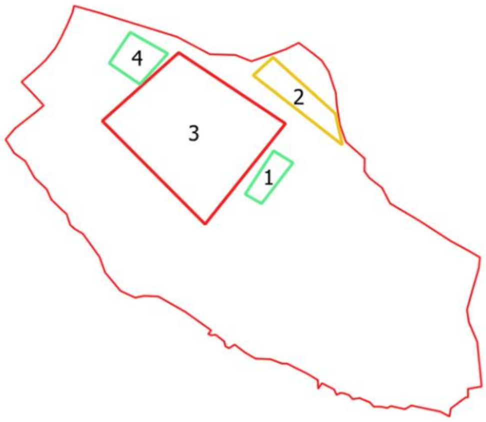

N°	Description	Sub-Area (ha)
1	Wood portion not degraded	1.27
2	Wood portion interested by fire in 2017	2.68
3	Wood portion interested by ecological degradation	18.51
4	Wood portion not degraded	1.85

Figure 29. FAO-LCCS2 dichotomous phase.

Since these areas have a dominant forest presence, thus, dense leaf cover, MSAVI, which applies a correction for the contribution of soil presence, was not found to be the most suitable spectral index (Borgogno-Mondino et al.; 2020).

Results

The following histograms, in Figure 30, report the percentage value obtained from the pixel count of NDVI, for each spectral category, in the specific sub-area, expressed in hectares and normalized with respect to the whole considered sub-area. Therefore, it represents a spatial distribution information of vegetation quality.

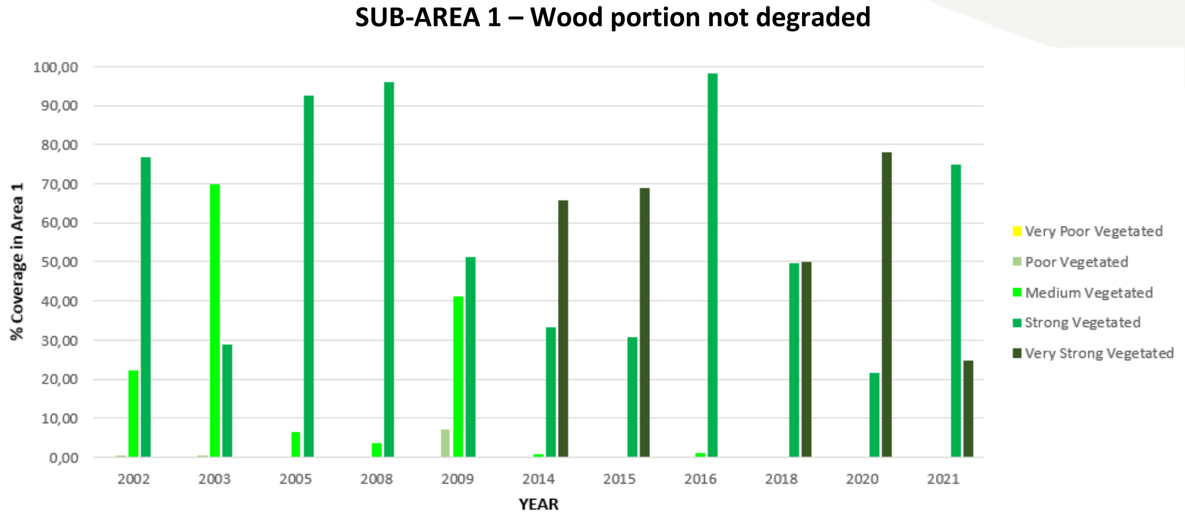
SUB-AREA 1 – Wood portion not degraded
% Coverage in Area 1
YEAR
Very Poor Vegetated
Poor Vegetated
Medium Vegetated
Strong Vegetated
Very Strong Vegetated

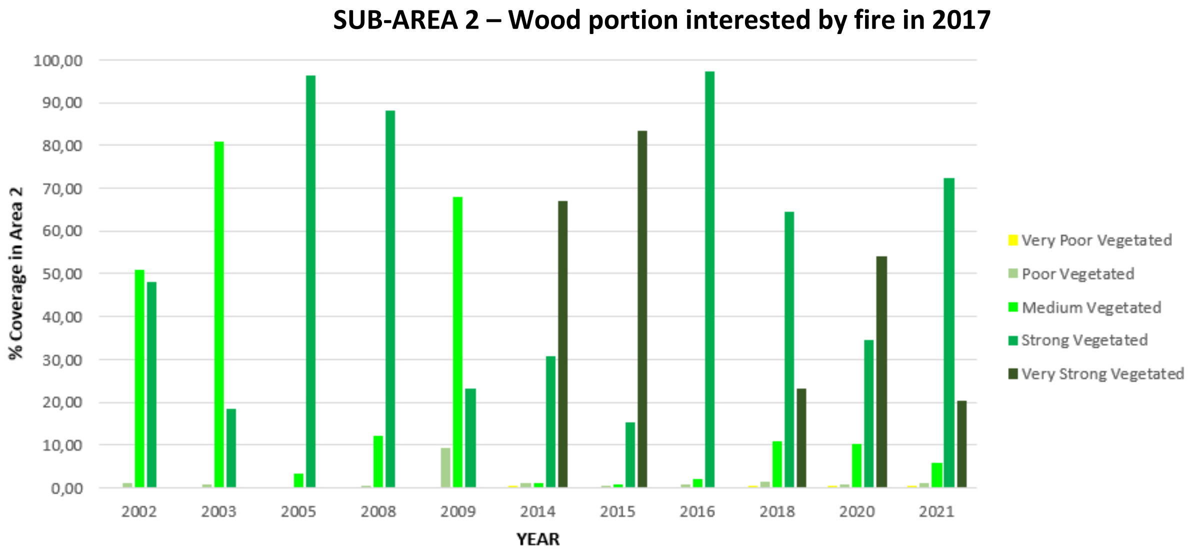
SUB-AREA 2 – Wood portion interested by fire in 2017
% Coverage in Area 2
YEAR
Very Poor Vegetated
Poor Vegetated
Medium Vegetated
Strong Vegetated
Very Strong Vegetated

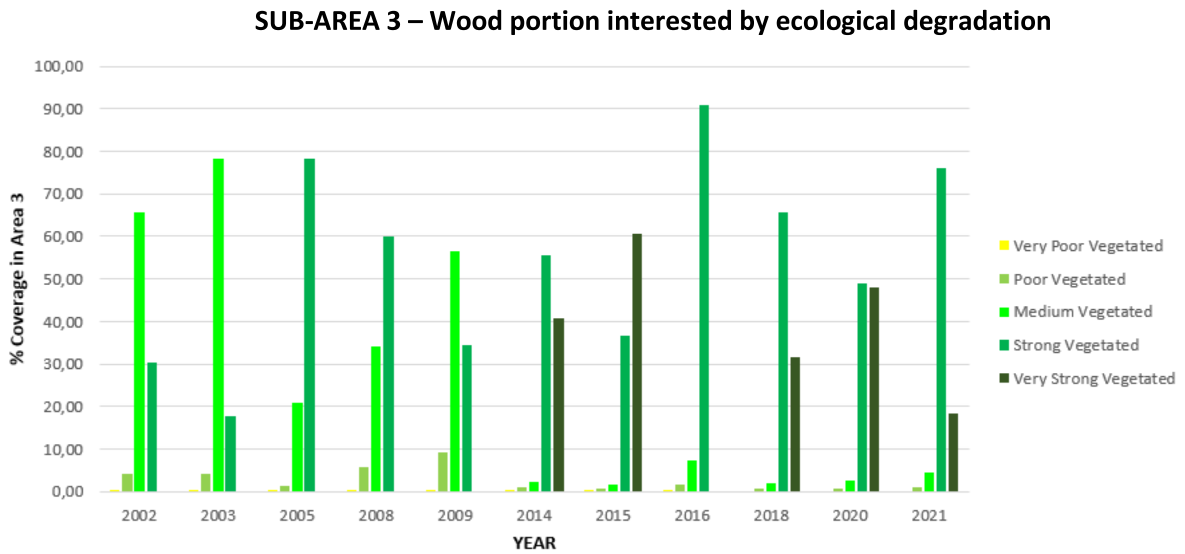
SUB-AREA 3 – Wood portion interested by ecological degradation
% Coverage in Area 3
YEAR
Very Poor Vegetated
Poor Vegetated
Medium Vegetated
Strong Vegetated
Very Strong Vegetated

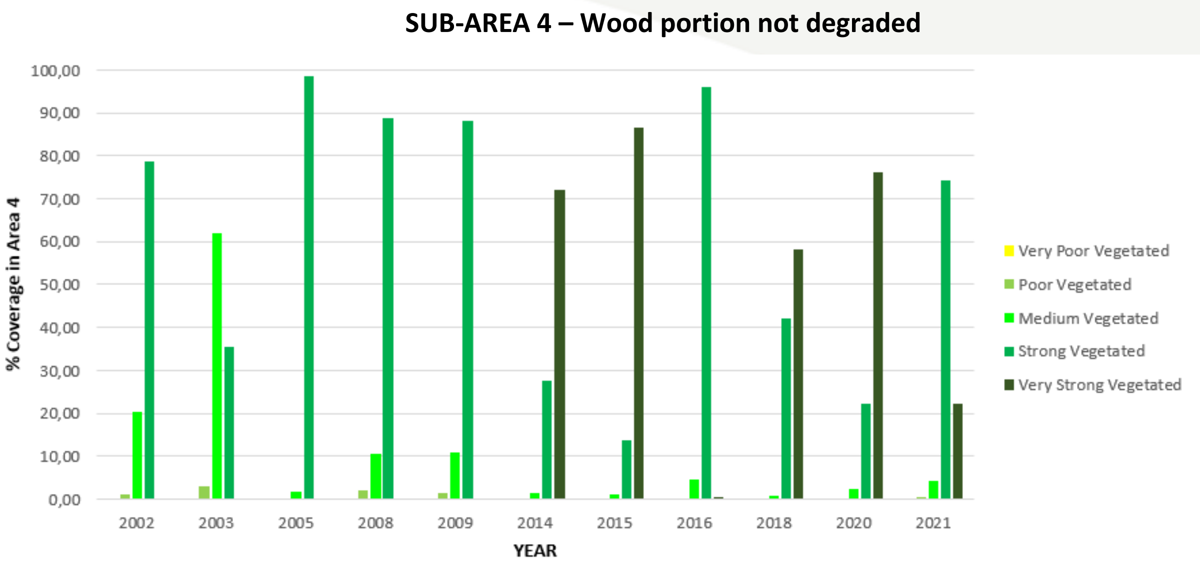

Figure 30. Histograms reporting percentage value of pixel count of NDVI, for each spectral category, in the specific sub-area.

The following considerations can be assessed:

- Before 2014 vegetation does not appear to have been in optimal condition;
- From 2014, vegetation health improved;
- Particularly, the woodland portion affected by degradation due to heat waves and fungal infection by the forest dieback (sub-area 3) turned its canopy cover down for about a decade after the early signs of ecological degradation in 2002;
- Particularly, the woodland portion affected by degradation due to heat waves and fungal infection (sub-area 3) turned its canopy cover down for about a decade after the early signs of forest dieback in 2002. In that period, vegetation appears mainly in a medium health status (medium vegetated) with a greater presence of poor vegetated status than in other sub-areas. Later on, the recovery of vegetation status remained lower than in other sub-areas;
- In 2018 sub-area 2 vegetation status is lower than elsewhere, presumably due to the fire event in 2017;
- Extremely low rainfall regimes of the annual and vegetation period (1st April-30th October of 2020), 540 mm and 277 mm, respectively, remarkably hindered the forest recovery process in 2021.

2.2.2 PP temporal trend

Methodology

The analysis of PP was based on the proxy PPI. As for Alta Murgia site, HR-VPP products from WEKEO were downloaded for Palo Laziale for the period 2017-2020 and a NetCDF file with 8 variables (MAXV, MAXD, MINV, TPROD, SOSD, SOSV, EOSV, EOSD) and 4 dimensions (vegetative season, time, latitude and longitude) was built. The data were grouped by the available habitat map, produced by LIFE PRIMED in 2020 and converted to FAO-LCCS taxonomy. Within the protected area, 9 classes were identified. Due to the limited extension of the site compared with Alta Murgia where 5 quantiles over a single habitat class were reported, for Palo Laziale only the mean value for all the habitat classes was reported.

Results

Plant Phenology Index (PPI)

Figure 31 shows the PP estimator (TPROD) for 2018 in the two different vegetation seasons in the same year.

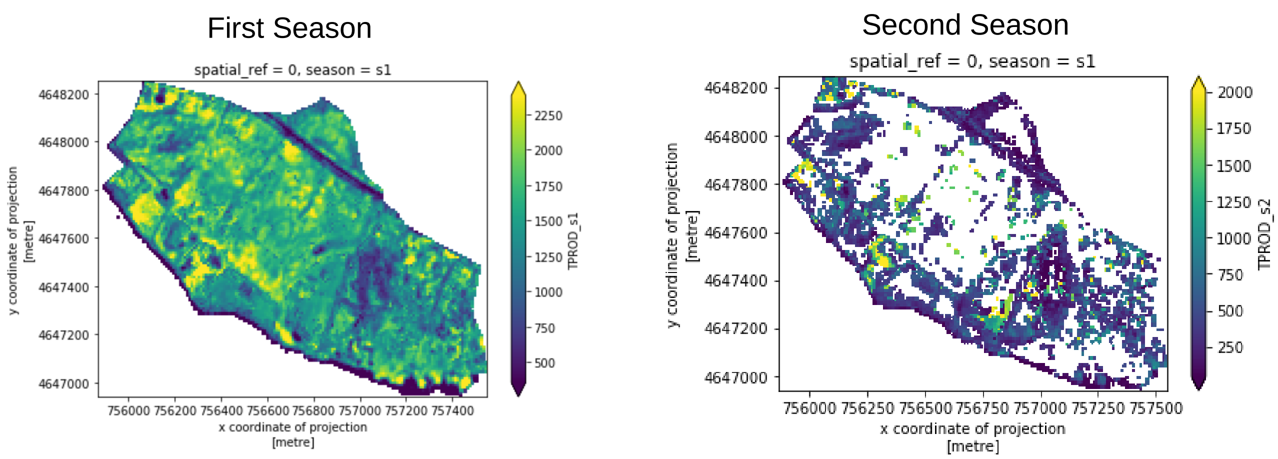

Figure 31. Overall view in Palo Laziale Tprod, integral of Seasons, for 2018.

Looking at Figure 32 is possible to notice that the first season has clearly more productivity than the second, although there is a trend of increase in the second season in 2020 for as many 4 classes over 8 for which the second season productivity closes the gap with the first season. This is untrue for herbaceous forbs in which productivity results relatively low in both seasons.

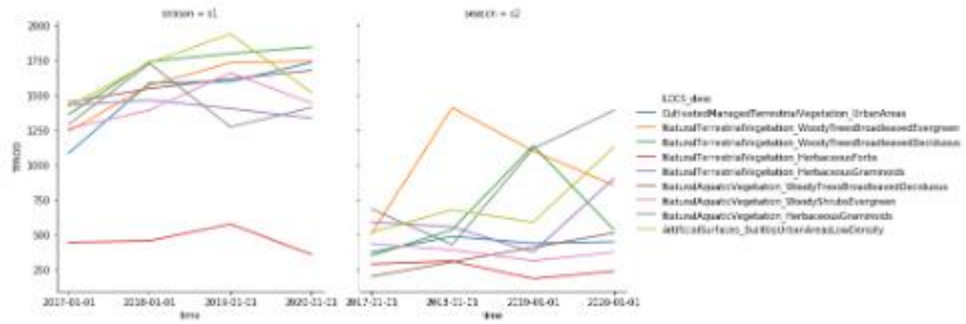

Figure 32. Trend of productivity over years, season and habitat cover.
Index is scaled as PPI multiplied for the day of the season.

From Figure 33 it is easy to notice that the average value of the end of the first season overlaps with the start of the second season, so very few times is occupied by the inter-seasonal minimum. The same for the end of the second season which quite overlaps the onset of subsequent first season.

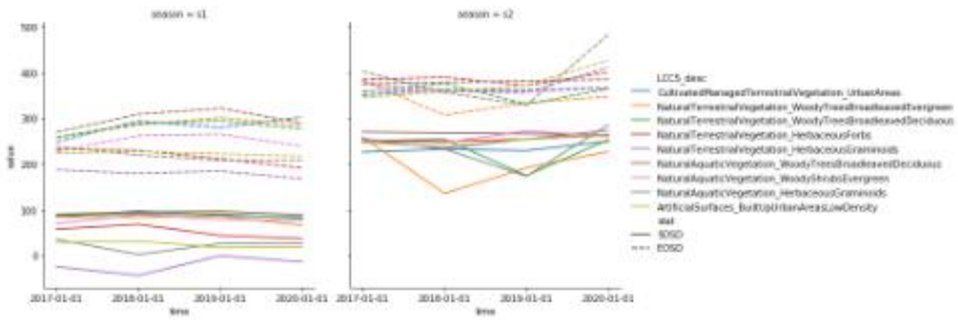

Figure 33. Average trend of start and end of season date over years, season and habitat classes.

Figures 34 and 35 show changes of PP in the period 2017-2020 for the two different vegetation seasons.

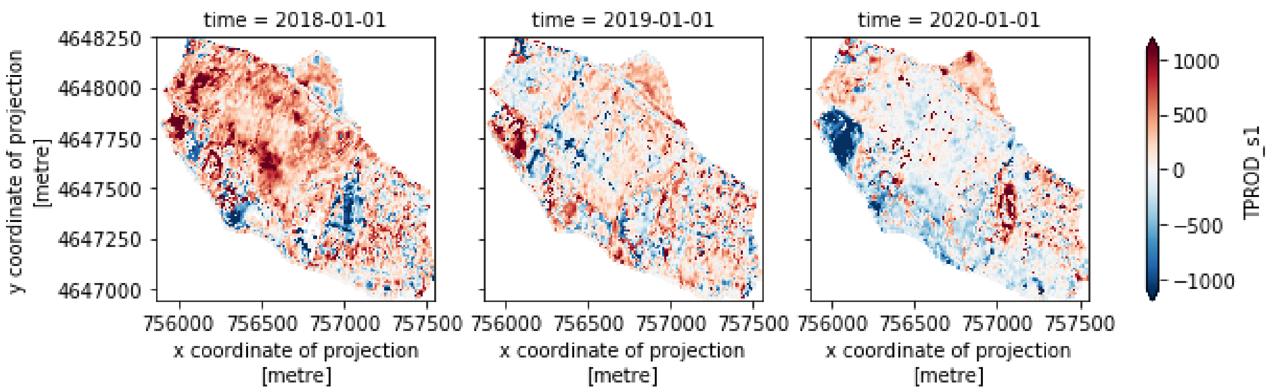

Figure 34. Change Across 2017-2020 in integral under the curve of first Season.

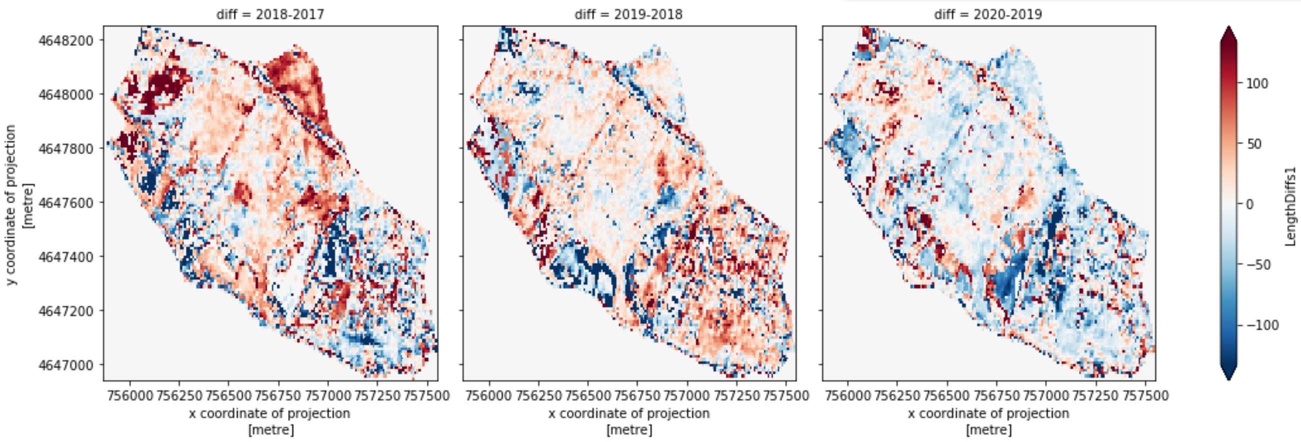

Figure 35. Change Across 2017-2020 in integral under the curve of first Season.

2.2.3 SPEI temporal trend

Methodology

The evaluation of SPEI on the “Bosco Palo Laziale” area outlines the main impacts that the increase in temperature has on water availability for vegetation and is used to identify and monitor the phenomena of dryness by evaluating two different time scales, monthly and quarterly. The choice of time integration is due to the large amount of data available for the site lasting from 1951 to 2020 for the following parameters: average temperature, minimum temperature, maximum temperature, and precipitation. The climatic data were recorded by a network of nearby weather stations, i.e., Maccarese (1951-2018), Cerveteri (1951-2018) and Palo Laziale (2019-2021) managed by the Regional Agency for Development and Innovation in Agriculture (ARSIAL). An alteration in the climate regime of the area embedding Palo Laziale wood emerges clearly from the series. Data shows annual warmer conditions of 0.6 C° from 1994 to 2018 and extreme rainfall oscillation from year to year, although from 2018 to 2021 it has been registered a worrying decrease in annual precipitation from 1328 to 468 mm.

Results

Looking at Figure 36, it is possible to compare the monthly and quarterly SPEI trends, where 31.5% of the monthly values show a tendency to aridity, having values below -0.5. The abundance of precipitation shows an opposite trend in some parts of the time series; where rainfall is more or less abundant, it impacts differently the cumulative monthly and quarterly integrations of the SPEI.

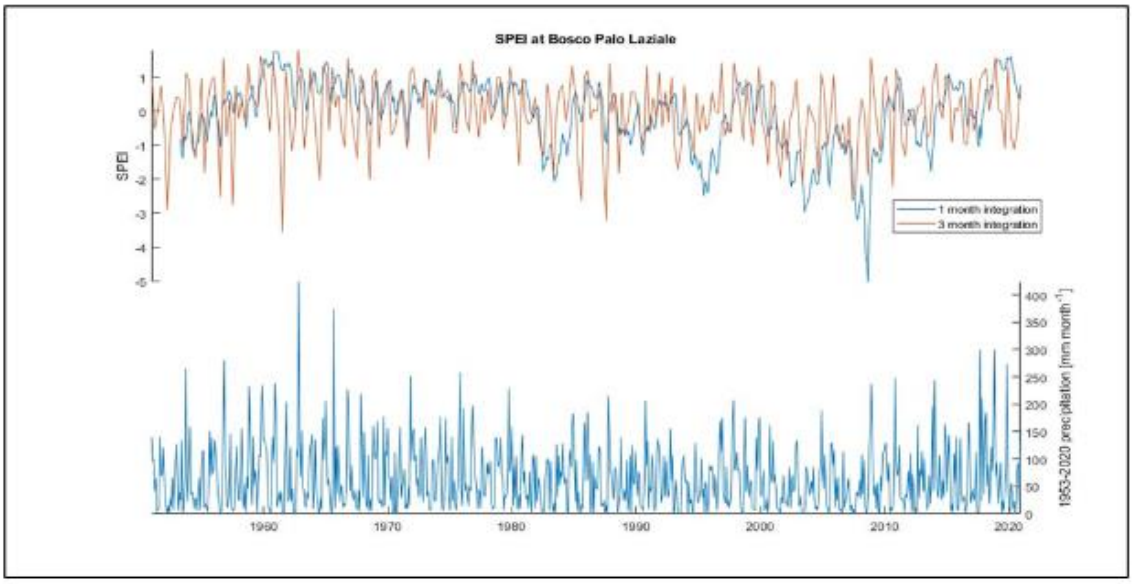

Figure 36. Monthly and quarterly integration of SPEI index for the reconstructed historical series of Palo Laziale wood.

What is evident in Figure 37 is an increase in intensity and duration of seasonal drought period. The phenomena of extreme aridity are frequent not only in the summer but also in the autumn and winter quarterly; such phenomena increase its frequency over time starting from the end of the 90s.

Categorization	SPEI values
Extremely wet	SPEI ≥ 2
Severely wet	1.5 ≤ SPEI < 2
Moderately wet	1 ≤ SPEI < 1.5
Mildly wet	0.5 < SPEI < 1
Normal	−0.5 ≤ SPEI ≤ 0.5
Mild drought	−1 < SPEI < −0.5
Moderate drought	−1.5 < SPEI ≤ −1
Severe drought	−2 < SPEI ≤ −1.5
Extreme drought	SPEI ≤ −2

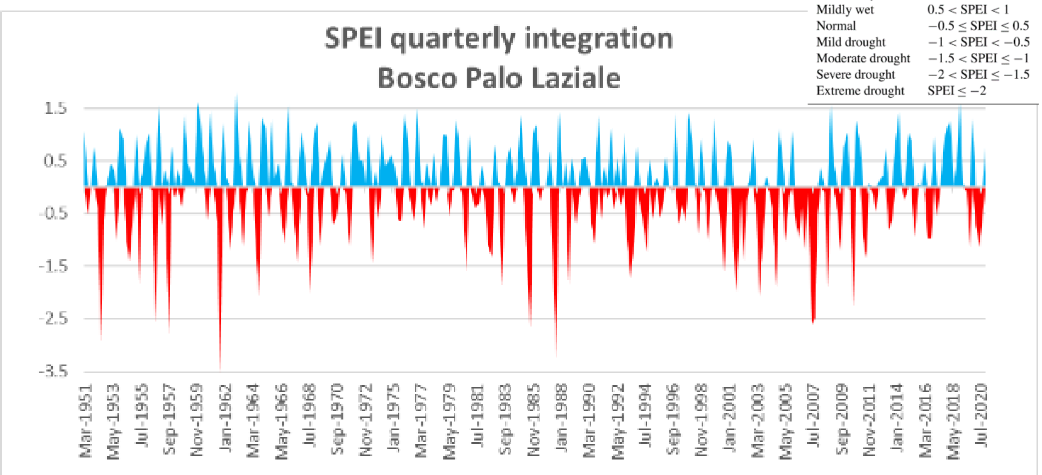

Figure 37. SPEI quarterly integration in the Palo Laziale wood since 1951.

This is confirmed by the decreasing trend of precipitation in the last 20 years (Figure 38), although extreme events counterbalance the SPEI values in the wettest months, these are insufficient to prevent aridity from becoming an increasingly frequent phenomenon throughout the year.

Categorization	SPEI values
Extremely wet	$\text{SPEI} \geq 2$
Severely wet	$1.5 \leq \text{SPEI} < 2$
Moderately wet	$1 \leq \text{SPEI} < 1.5$
Mildly wet	$0.5 < \text{SPEI} < 1$
Normal	$-0.5 \leq \text{SPEI} \leq 0.5$
Mild drought	$-1 < \text{SPEI} < -0.5$
Moderate drought	$-1.5 < \text{SPEI} \leq -1$
Severe drought	$-2 < \text{SPEI} \leq -1.5$
Extreme drought	$\text{SPEI} \leq -2$

(a) (b)

Figure 38. SPEI in the Palo Laziale wood in the last 20 years: (a) monthly; (b) quarterly integration.

2.2.4 SOC temporal trend

Methodology

The extraction of SOC temporal trend was performed by following the same procedure as for Alta Murgia site (section 2.1.5) applied to the only sub-area 3 subjected to ecological degradation.

Results

The periods reported in Table 15 were considered for SOC temporal trend mappings.

Table 15. List of periods considered for the SOC temporal trend mappings.

Period	Spatial resolution (m)	Objectives
2002-2014	2	Period of ecological degradation
2014-2021		Period of ecological recovery

Figure 39 shows the SOC temporal trend mappings produced.

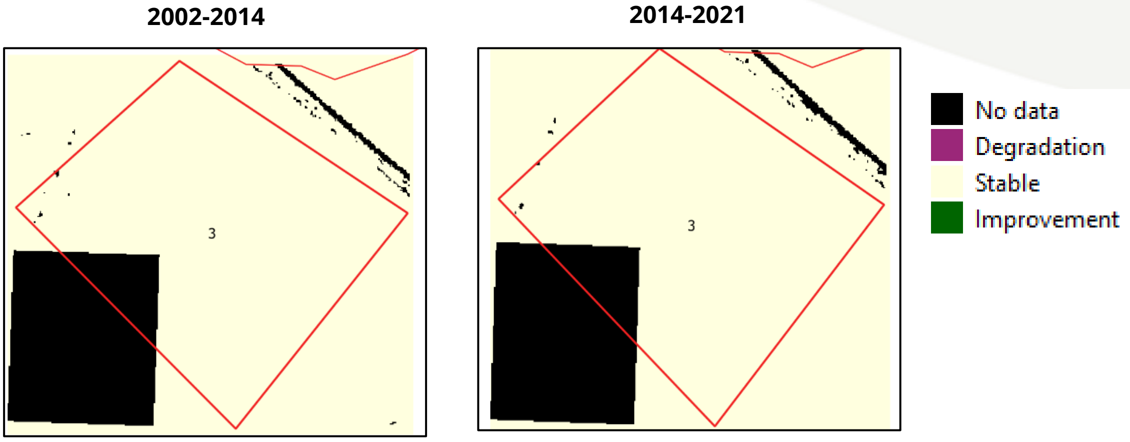

Figure 39. SOC degradation mappings produced for Palo Laziale.

A stable result was obtained in the ecologically degraded sub-area 3. In any case the adopted *Trends.Earth* approach which search for a matching between the reference *SoilGrids* at 250 m with LC maps at 2 m can be considered not so accurate.

2.2.5 SDG 15.3.1 computation and land degradation mapping

Methodology

In the computation of SDG 15.3.1 indicator for Palo Laziale only LC changes were considered due to the too coarse spatial resolution of the other sub-indicators compared with LC mappings. As LC trend the changes in the NDVI categorized values reported in Table 14 in the period 2002-2021 were considered for deciduous vegetation LC class (Table 12) mapped from VHR LC mappings for 2021. This LC class was the main affected by ecological degradation and the followed approach allowed to take into account of a sort of trend for vegetation status.

Hence, SDG 15.3.1 indicator computation for Palo Laziale followed the same steps described in sub-section 2.1.6 with the following specific choices:

- temporal ranges to be monitored: 2002-2003 (period of high degradation declared for the class of interest), 2003-2014 (period of ecological degradation) and 2014-2021 (period of vegetation recovery);
- a spatial scale of 2-meters;

- only the trend for Natural Terrestrial or Aquatic Vegetation/Trees.Broadleaved.Deciduous (the class mainly affected by ecological degradation) mapped for 2021 was considered back in time;
- Vegetation Degradation was assumed for transitions from Strong/Very Strong Vegetated status to Medium/Poor/Very Poor Vegetated spectral categorization;
- The analysis was performed for deciduous vegetation mapped SUB-AREA 3 in 2021 affected by ecological degradation during time.

Results

The degradation mappings for the different periods considered are reported hereafter.

1. For the period 2002-2003 the degradation mapping is shown in Figure 40:

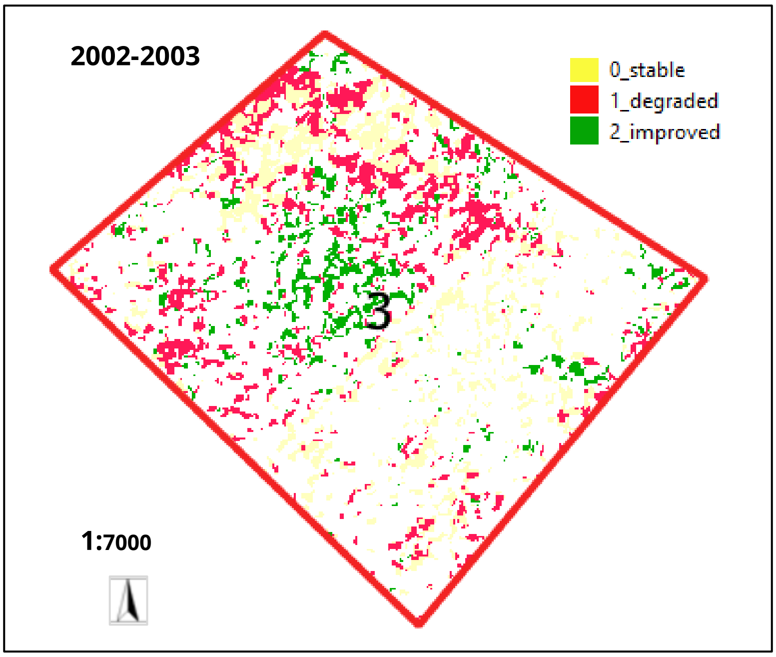

Figure 40. Land degradation mapping for Palo Laziale SUB-AREA 3 for the period 2002-2003.

The resulting SDG 15.3.1 indicator percentage was equal to 6.24%.

2. For the period 2003-2014 the degradation mapping shows only improvement as reported in Figure 41:

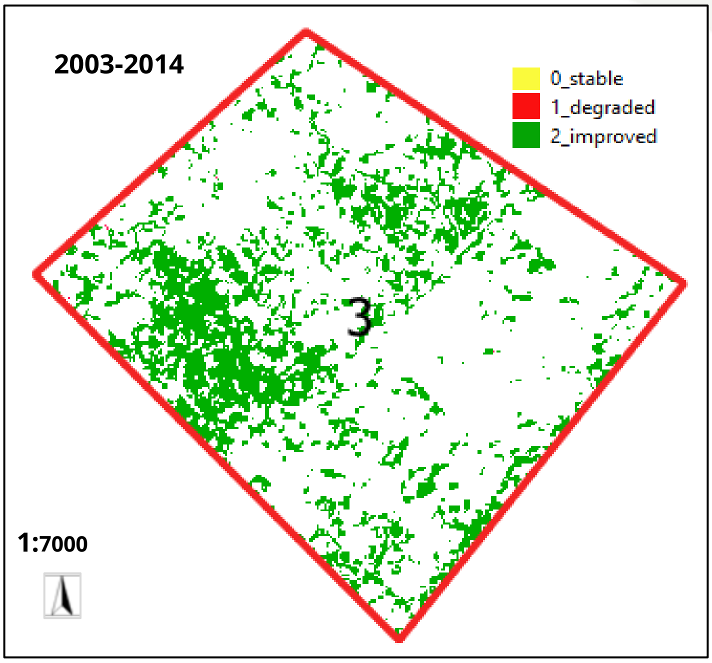

Figure 41. Land degradation mapping for Palo Laziale SUB-AREA 3 for the period 2004-2018.

The resulting SDG 15.3.1 indicator percentage was equal to -24.25%.

3. For the period 2014-2021 the degradation mapping is reported in Figure 42:

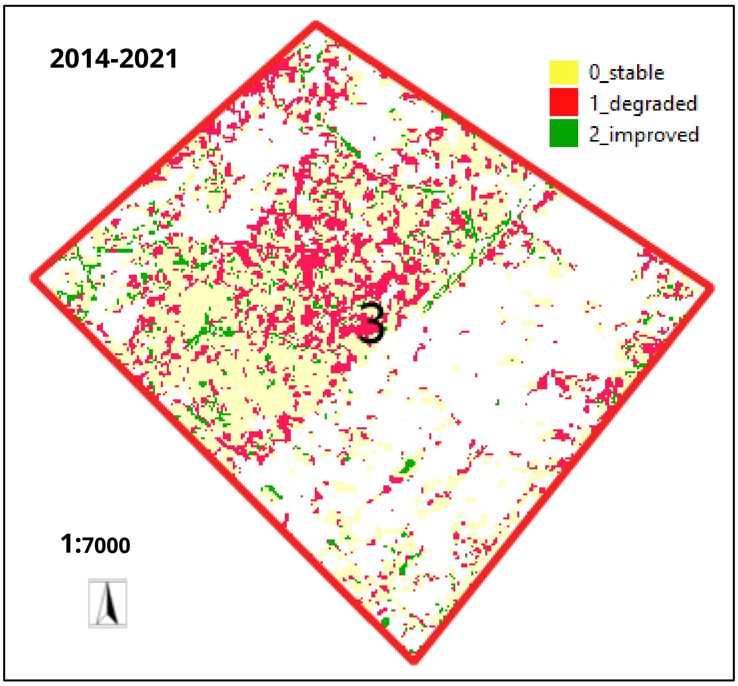

Figure 42. Land degradation mapping for Palo Laziale SUB-AREA 3 for the period 2014-2021.

The resulting SDG 15.3.1 indicator percentage was equal to 11.58%.

3.1 Nestos (Greece)

The Delta of the river Nestos, one of the most important rivers in South-Eastern Europe, is an alluvial plain of high ecological significance for both residential and migratory wildlife. (Figure 43). A significant feature is represented by the riparian forest: even though it has been highly reduced from 12,000 ha in the early 1920s to merely 2,000 ha in strips along both banks of the river it still remain one of the largest natural riparian forest in Greece.

Figure 43. Nestos N2K sites, GR1150001 and GR1150010, in the study area.

The site hosts different habitat types including priority ones such as Coastal lagoons (1150*), Mediterranean temporary ponds (3170*) and Alluvial forests (91E0*).

In the period 1992-2002, a gross natural loss for agricultural purposes was observed, and alluvial areas were further reduced due to two large dams on the Nestos River (170 m and 95 m in height) which reduced the river’s sediment load (Xeidakis & Delimani, 2002). The habitat types of Nestos are, thus, very sensitive to modifications of the hydrological cycle due to both direct and indirect pressures (e.g. inappropriate river management, climate change, respectively) since their life cycle depends on the regular alternation of wet and dry phases. For instance, during winter 2016-2017, some ponds held water for only about 2 months, compared to the average (about 6 months), and their typical vegetation did not have the opportunity to complete its life cycle. On the other hand, in alluvial forest habitat (91E0*), the lack of flooding also means no transport of nutrient-rich sediments, which enrich the soils.

Furthermore, the uncontrolled expansion of shrubs affects both the 3170* and the 91E0* habitat types. Another problem is the illegal logging and trampling that affects the forest structure and the temporary ponds, respectively, which has noticeably increased in recent years because of the economic crisis and lack of local people's awareness about their importance. In the end, there is also the problem of the Invasive Alien Species. The number of these species amounts to three (*A. fruticosa, P. dioica, A. negundo*), and they are outcompeting indigenous species, mainly in 91E0*, but also encroaching on 3170*.

From 2018, these pressures and threats are targeted by a set of restoration interventions implemented by LIFE PRIMED (LIFE17 NAT/GR/000511). These measures include control by removal of invasive plant species, an hydraulic system to make temporary ponds more resilient to unmanageable river loads information boards and awareness-raising campaign to reduce illegal logging and trampling.

In the early 2000s, project LIFE NESTOS (LIFE02 NAT/GR/008489) included reforestation in public lands along the river with indigenous species to increase the size of the forest. In total 60 ha of new forest were created. Parts of the reforested areas were fenced to prevent access and vegetation has grown abundantly. However, large portions of these areas seem to have deteriorated nowadays due to water lacking at river flow and rainfall levels.

The following indices and sub-indicators, reported in Table 16, have been selected to monitor the pressures described above:

Table 16. Indices and sub-indicators selected for Nestos study site.

<table>
<tr><th colspan="2">Sub-indicators</th><th>Sensor</th><th>Spatial resolution (m)</th><th>Spatial frame</th><th>Temporal frame</th></tr>
<tr><td colspan="2" rowspan="2">LAND COVER MAP</td><td>Landsat</td><td>30</td><td rowspan="3">N2K</td><td>2000; 2005; 2010</td></tr>
<tr><td>Sentinel-2</td><td>10</td><td>2017; 2021</td></tr>
<tr><td>PRIMARY PRODUCTIVITY* MAP</td><td>VEGETATION PHENOLOGY INDEX (MSAVI2)*</td><td>Landsat</td><td>30</td><td>2000-2018</td></tr>
</table>

	PLANT PHENOLOGY INDEX (PPI)*	Sentinel-2	10		2017-2020
HYDRO-PERIOD MAP					Oct. 2017 – Sept. 2018; Oct. 2019 – Sept. 2020; Oct. 2020 – Sept. 2021
SOIL SALINITY INDICES					2017; 2021
STANDARDIZED PRECIPITATION EVAPOTRANSPIRATION INDEX (SPEI)			-----------		2019-2021
SOC MAP		Soilgrids+ LC maps	30		2000-2017; 2017-2021; 2000-2021

3.1.1 LC temporal trend

Methodology

LC mappings were obtained by a supervised data-driven approach considering ground truth data for training SVM classifiers acquired by expert knowledge, photointerpretation of HR satellite data and a vegetation map produced by Management Body of the area. A different SVM classifier (Huang et al., 2002; Mountrakis et al., 2011) was trained for multi-class problems, one for each year, due to its effectiveness in high dimensional spaces (Foody & Mathur, 2004) and well-suited when small training data sets are available. Following the recommendations reported by Othman & Gloaguen (2014), in our study a radial basis function was selected as kernel type while the penalty parameter chosen was taken as 100. The gamma in kernel function was chosen as the inverse of the band numbers used in the data input (Yang, 2011).

Input data to the classifier consisted in a multi-temporal dataset composed of satellite time-series images selected among those images with no cloud cover for each year considered, namely 2000, 2005, 2010, 2017 and 2021. From 2000 to 2010, Landsat satellite imagery was considered, at a 30-m spatial resolution, whereas for 2017 and 2021 Sentinel-2 satellite data, a 10-m spatial resolution was used. We chose to produce mappings with higher spatial details (10 m) for recent years to allow local management authorities a more effective tool. (Tarantino et al; 2023).

For each satellite image the spectral bands in the Vis–NIR–SWIR were considered, resulting in 6 bands for Landsat 5 TM and 10 bands for Sentinel-2 A/B data.

Landsat data were freely downloaded from the USGS EarthExplorer portal (https://earthexplorer.usgs.gov/), Collection 2, Level 2, surface reflectance products, thus, atmospherically correct, and orthorectified using ground data by USGS. The whole N2K PA results covered by the track 183, frame 31 and 32, so a mosaicking step was realized after cropping the boundary of interest. Sentinel-2 data were freely downloaded from the ESA Copernicus Open Access Hub (https://scihub.copernicus.eu/dhus/#/home) as L2A products which are surface reflectance and orthorectified products. Even in this case, the entire study area results covered by the tile 35TLF. The bands with native spatial resolution of 20 meters (i.e., B5, B5, B7, B8A, B11, B12) were resampled, by a Nearest Neighbour algorithm, at 10 meters as those natives (B2, B3, B4, B8).

Table 17 shows the whole set of satellite imagery considered jointly with their acquisition dates.

Table 17. List of satellite imagery considered for the LC mappings.

Year	Acquisition date	Sensor	Spatial resolution (m)	Bands
2000	June, 6th; July, 8th; August, 25th; November, 13th	Landsat 5 TM	30	B1, B2, B3 (Vis) B4 (NIR) B5, B7 (SWIR) (6 bands)
2005	March, 16th; April, 8th; June, 4th; June, 27th; July, 29th			
2010	April, 22nd; May, 1st; July, 4th; August, 12th; September, 22nd; October, 31st			
2017	April, 26th; June, 5th; July, 15th; August, 14th; September, 13th	Sentinel-2 A/B	10	B2, B3, B4 (Vis) B5, B6, B7 (Red Edge) B8, B8A (NIR) B11, B12 (SWIR) (10 bands)
2021	March, 31st; May, 10th; June, 24th July, 29th; September, 2nd			

The images of each year, with its own bands each one, were stacked obtaining a multi-season raster dataset composed of 24 layers, in the case of Landsat data, or by 40 layers for Sentinel-2 data. Among mapped LC classes, labelled according to, where possible, FAO-LCCS2 class taxonomy, different types of crops were identified according to their vegetated or barren cover (G or B, respectively, are used in the legend) in the different months. Although images from the same months are not always available in all the years considered, rough discrimination between 4 types of crops (asparagus, corn, alfalfa, wheat soft) was attempted.

The LC class related to reafforestation interventions of poplar plants in the framework of previous initiatives/projects was identified and included as “PREVIOUS_ARTIFICIAL_POPLAR_PLANTATIONS”. Furthermore, a large part of class “NOT NATURAL_TERRESTRIAL_VEGETATION_TREES-SHRUBS_DECIDUOUS” mainly in the south-west part of the image, can be related to a mixed class composed by the human reafforestation (Robinia etc.) intervention, in the framework of LIFE NESTOS project, and invasive allochthonous species.

Results

Figure 44 shows the different LC mappings produced.

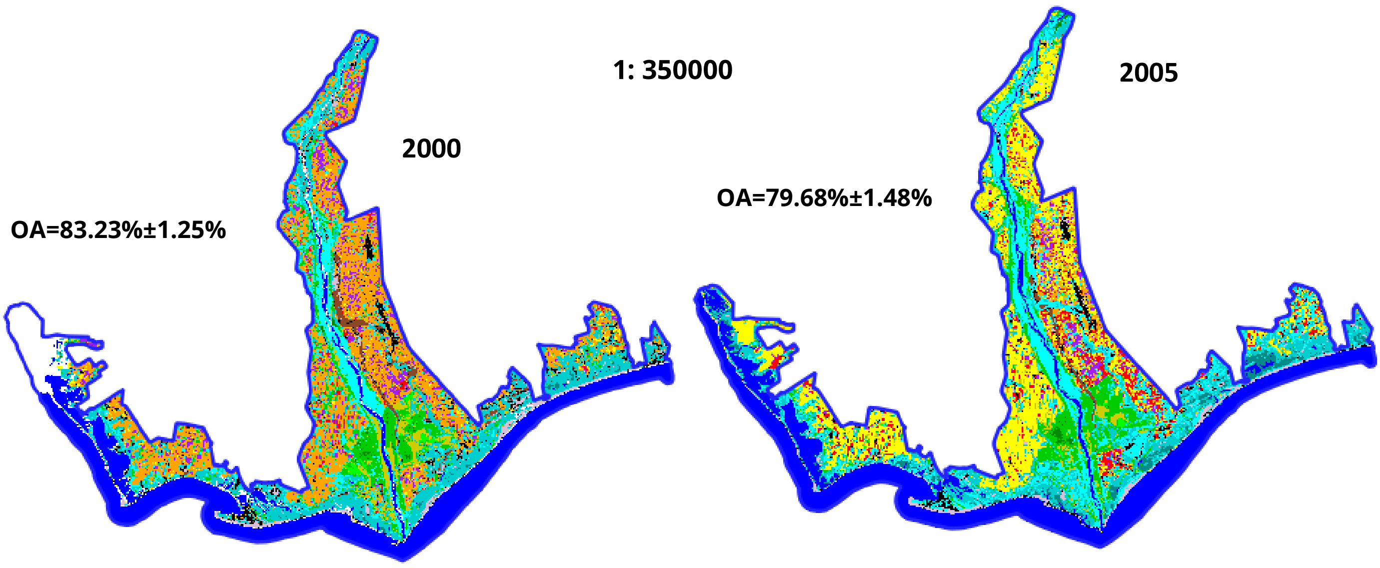

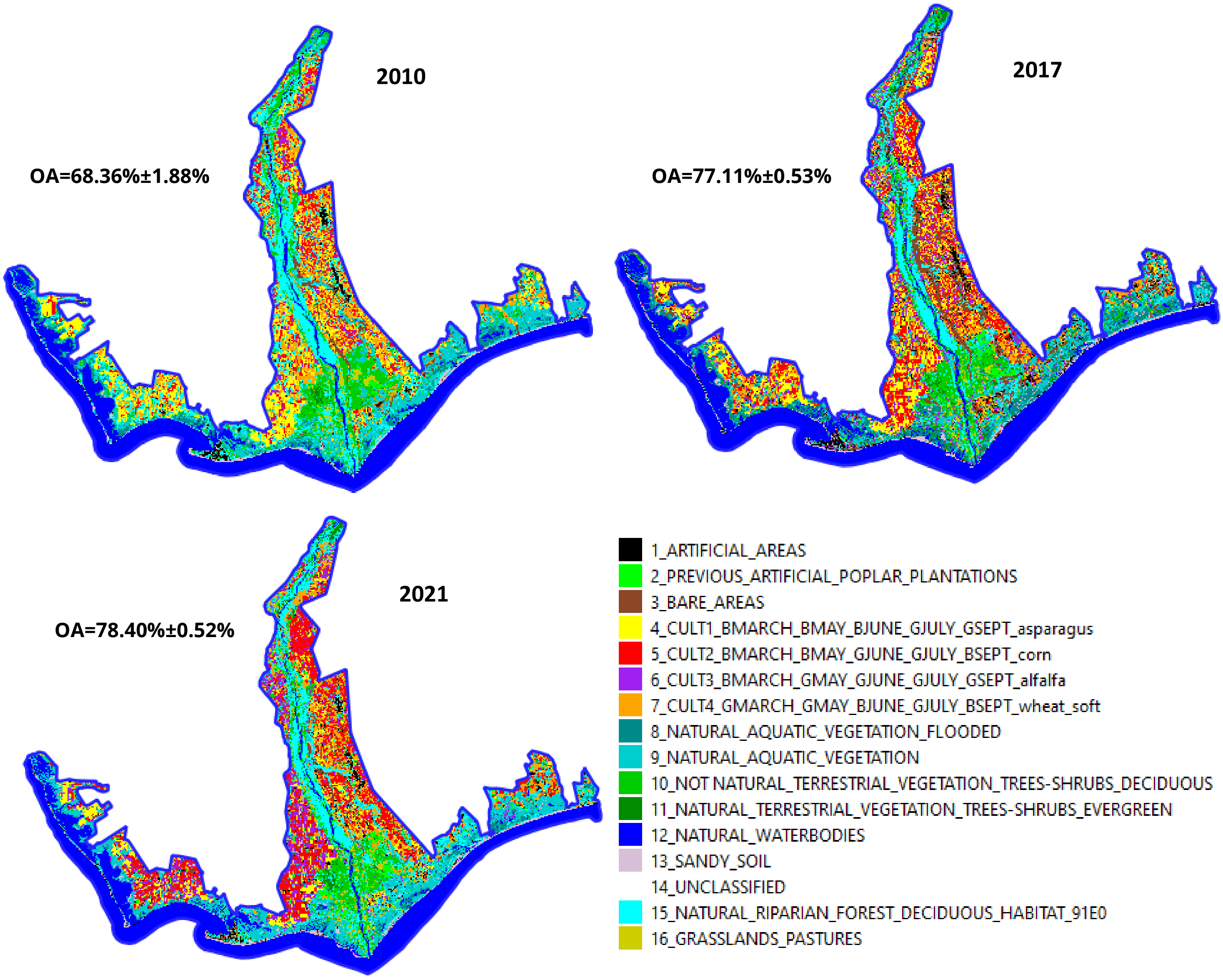

Figure 44. LC mappings for Nestos site.

Figure 45 shows several plots of the presence of several LC classes, among the most significant, during the period 2000-2021 to evaluate their temporal trend.

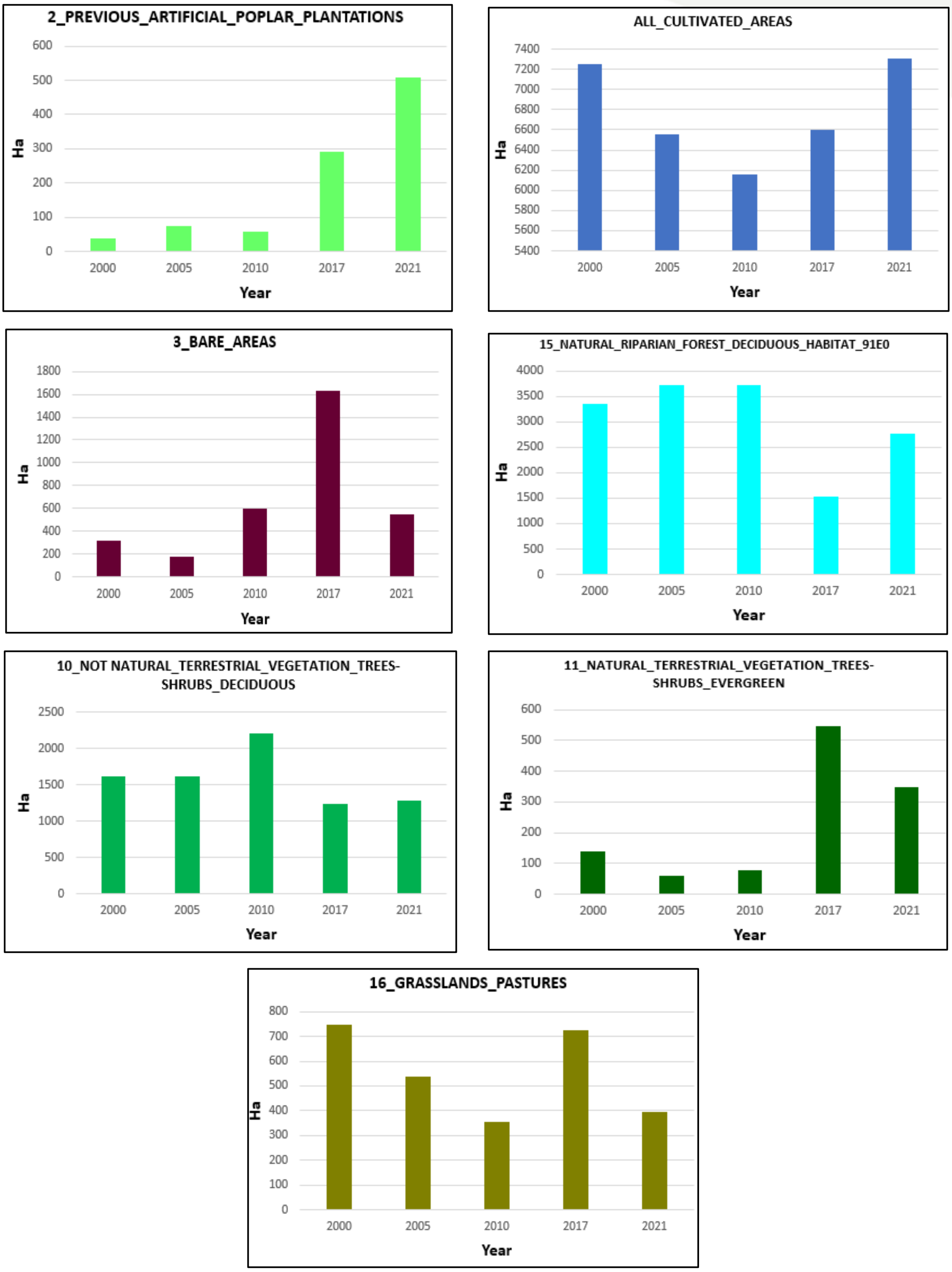

Figure 45. Plots for several significant LC classes trend vs. time.

The following considerations can be assessed:

- Class "PREVIOUS_ARTIFICIAL_POPLAR_PLANTATIONS" has highly increased after 2010, reinforcing the efficacy of restoration activities of the last decades;
- According to pressures and threats identified in the site, the loss of cultivated areas already started in 1992 has continued until 2010: an increase was revealed from 2017 mainly of corn and alfalfa;
- In 2017 the growth in the presence of class "BARE_AREAS", due to a scarcely rainy winter, was identified, even though an adverse water limitation due to the upstream dams cannot be excluded;
- In 2017, according to the lack of flooding causing no transport of nutrient-rich sediments for enriching the soils, a loss in the presence of class "NATURAL_RIPARIAN_FOREST_DECIDUOUS_HABITAT_91E0" was identified whereas in 2021 an increase of that class could be due, probably, to improved conditions in terms of water availability in the topsoil;
- In the terminal section of the river, massive hydraulic and reforestation interventions, including those carried out by LIFE NESTOS from 2002, have converted large patches of grasslands to area covered by broad-leaves deciduous (e.g. Robinia pseudocacia). These areas maintained a good forest cover until the early 2010s but towards 2017, they have been progressively replaced by evergreen woodland species, grasslands and bare soil (i.e., a reactivated old branch of the river, now dried up). From 2017, an overall increase of wetter conditions seems to have favoured an expansion of 91E0* cover in these areas.

Figure 46 shows in cyan colour an area in the west side of the Nestos River where *A. fruticosa* invasive species is being monitored from local experts.

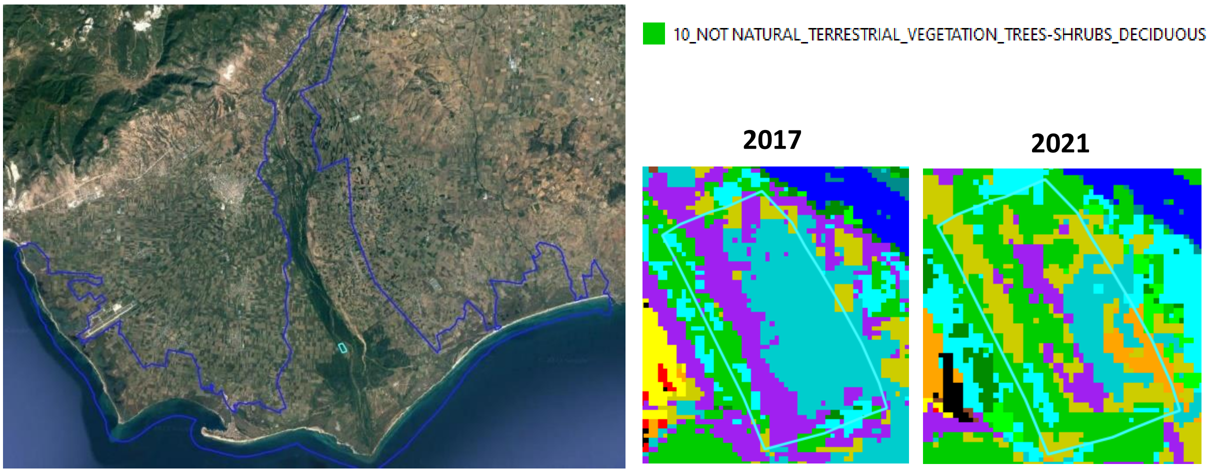

Figure 46. In the cyan colour rectangle, the area where *A. fruticosa* is being monitored. Some close-ups of the related LC mappings for 2017 and 2021.

Comparing 2017 and 2021 LC mappings emerges that the presence of class "10_NOT NATURAL_TERRESTRIAL_VEGETATION_TREES-SHRUBS_DECIDUOUS", to which *A. fruticosa* belongs to, registered an increase from 10.53% to 35.93%, respectively. This is quite in agreement with in-field inspection.

3.1.2 PP temporal trend

Methodology

As for previous sites we make use of HR-VPP dataset from 2017 to 2022 with a reanalysis of the phenology with an harmonic model (Vicario et al. 2020). Given the very different region that encompasses Nestos delta we concentrate only on riparian forest (15_NATURAL_RIPARIAN_FOREST_DECIDUOUS_HABITAT_91E0 class) and to best appreciate the difference we divided the analysis in two parts: the two coastal areas and the central area directly influenced by the river.

Results

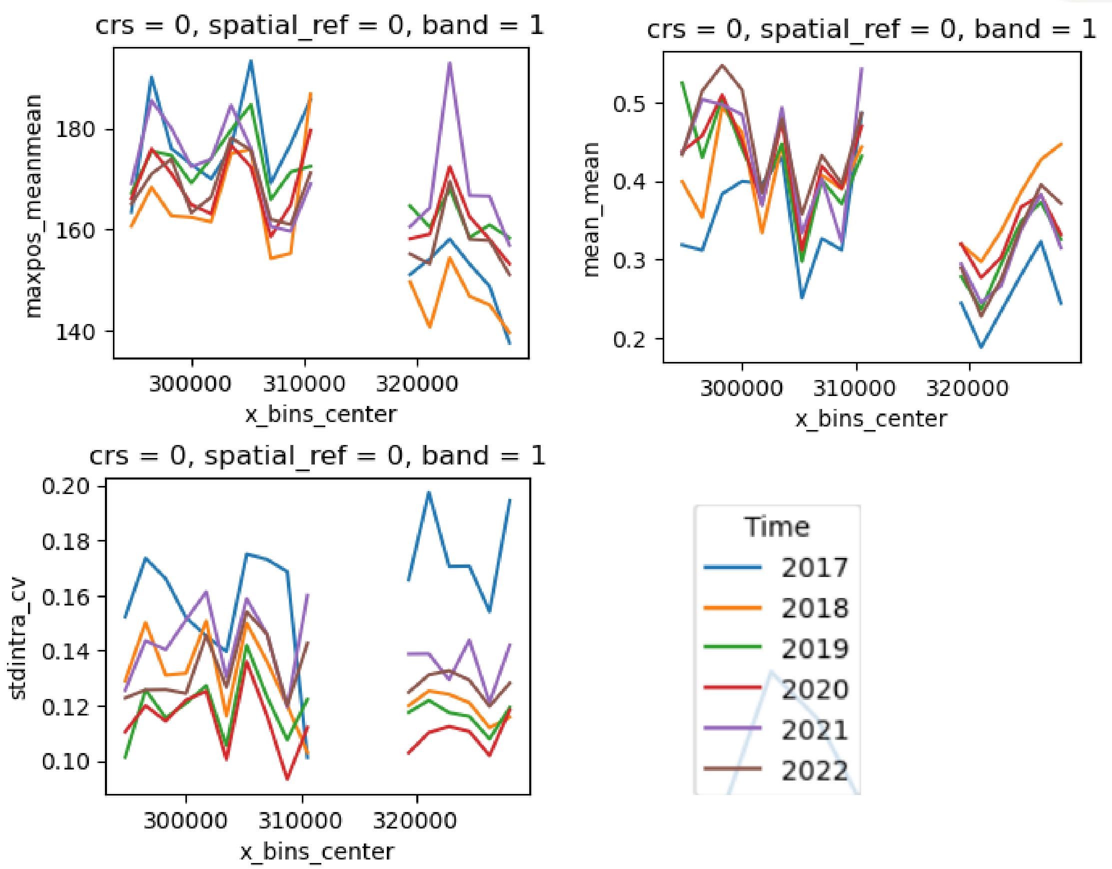

Figure 47. The mean, day of maximum and coefficient of variation of vegetation index across the 6 years of analysis along the east to ovest gradient on the coastal line.

The analysis of the coastal line shows clearly disparity between the two coasts, but the difference is limited today of the maximum and mean value and are stronger in some year as 2017.

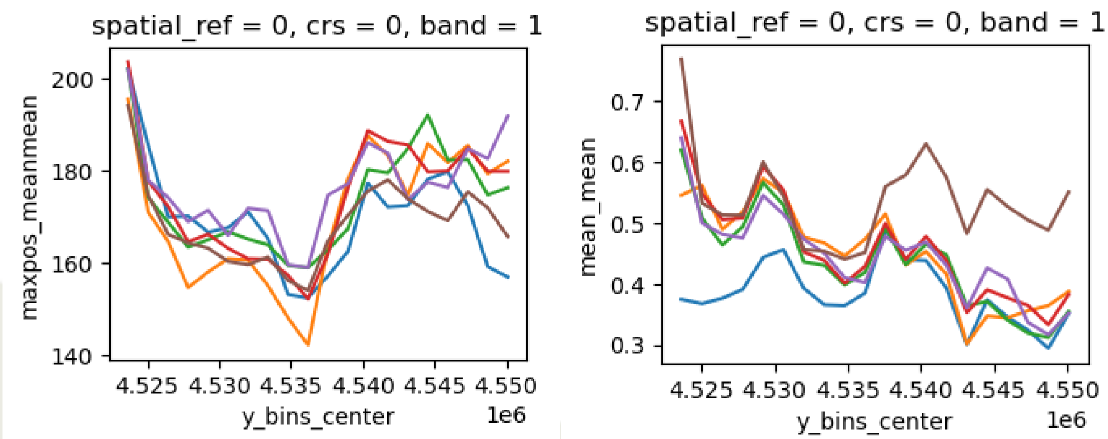

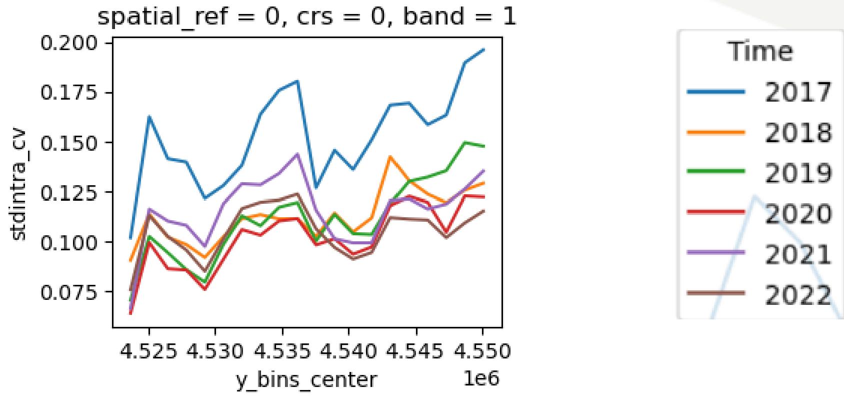

Figure 48. The mean, day of maximum and coefficient of variation of vegetation index across the 6 years of analysis along the south to north gradient on the coastal line.

As it is possible to observe in Figure 49, a clear gradient is possible to observe for coefficient of variation and, with the exception of 2017 and 2022, while for day of the maximum we obtain late day in the year along the coast and the at north.

Looking at the full image is possible to see that is not a simple gradient but it seems that two different riparian forests exist. One characterized by high mean value and late spring maximum near the river and the other with low mean and winter maximum far from the river and more to the north.

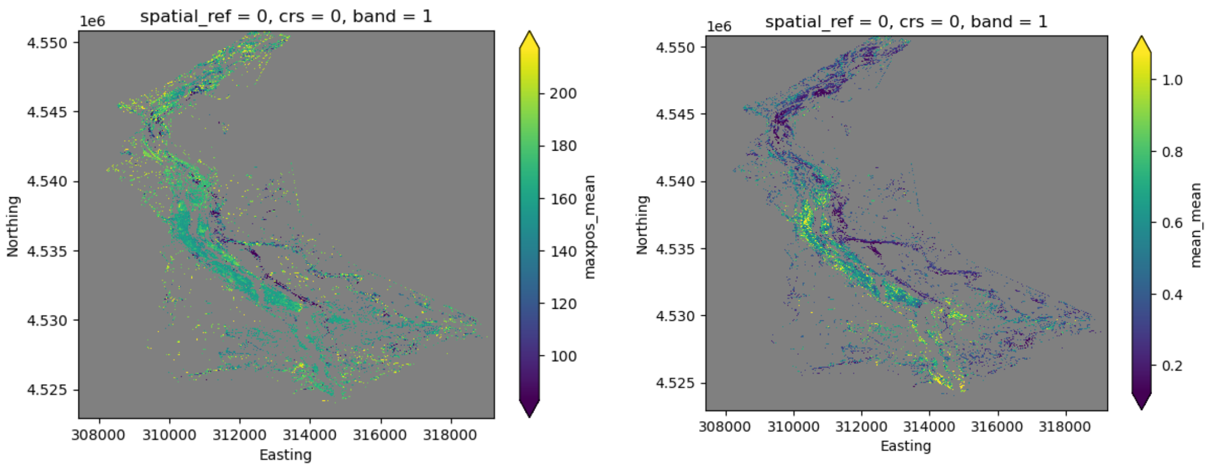

Figure 49. Mean across the 6 years for mean of the year and day of the maximum.

3.1.3 SPEI temporal trend

Methodology

Meteo data for Nestos area comes from only one weather station starting from mid-2019.

Two different time scales monthly and quarterly were evaluated.

Results

Looking at Figure 50, it is possible to identify the presence of values below -1 of the SPEI showing a tendency to aridity.

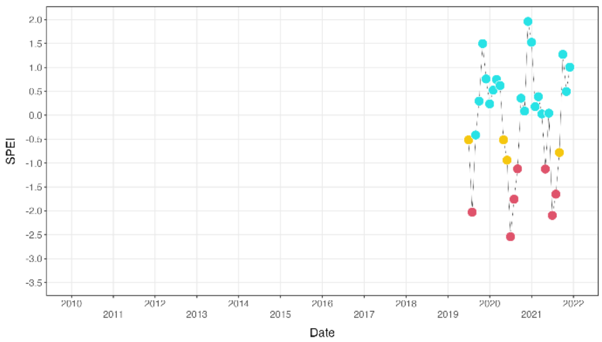

Categorization	SPEI values
Extremely wet	$\text{SPEI} \geq 2$
Severely wet	$1.5 \leq \text{SPEI} < 2$
Moderately wet	$1 \leq \text{SPEI} < 1.5$
Mildly wet	$0.5 < \text{SPEI} < 1$
Normal	$-0.5 \leq \text{SPEI} \leq 0.5$
Mild drought	$-1 < \text{SPEI} < -0.5$
Moderate drought	$-1.5 < \text{SPEI} \leq -1$
Severe drought	$-2 < \text{SPEI} \leq -1.5$
Extreme drought	$\text{SPEI} \leq -2$

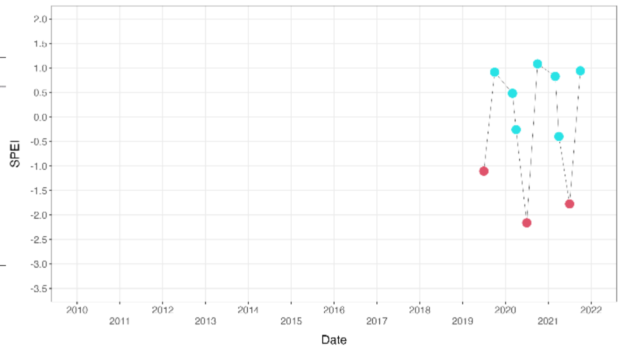

(a) (b)

Figure 50. Monthly and quarterly integration of SPEI index for Nestos study site.

3.1.4 HydroPeriod (HP) temporal trend

Methodology

The Hydroperiod mapping extraction was delivered by CERTH-ITI group not part of the project consortium through an external assignment.

Utilizing the WaterMask and HydroMap modules developed in H2020 ECOPOTENTIAL project (D6.3, http://www.ecopotential-project.eu/results/deliverables.html), CERTH provided high spatial accuracy hydroperiod maps of the area of interest. The WaterMask module detects automatically thresholds on different Sentinel-2 based inputs and on a MNDVI, derived from radiometrically-corrected Sentinel-2 data. Then, it combines them in a meaningful way based on a knowledge base coming out of an iterative trial-and-error process. This approach was validated for its high performance using numerous Sentinel-2 images for Doñana and Camargue Biosphere Reserve areas. These inundation maps, created with the WaterMask module, will be further used in the HydroMap module to calculate the per pixel inundation regime across the given time period. This module generates a hydroperiod map from series of inundation maps, falling within the time period between the starting and the ending date of hydroperiod, by applying an interpolation approach.

One of the limiting factors when using Sentinel-2 data for creating the inundation maps is the cloud coverage of the areas of interest. Cloud coverage may impact the correct classification of the inundated areas and introduce noise or prohibit the creation of an inundation map completely. To further overcome this obstacle, CERTH devised a novel machine-learning fusion approach to generate inundation maps under all circumstances by combining Sentinel-1 and Sentinel-2 images. By taking advantage of the Sentinel-1 data more precise and not affected by the cloud cover presence (MW spectrum) and accurate inundation maps and hydroperiods may be created, but at the same time the processing time and complexity of the methods increases, while the accuracy drops by a few percentages.

WaterMasks module:

- Input: Sentinel-2 intra-annual time-series multispectral data (possibly also Sentinel-1);
- Output: Inundation map (watermask) as a GeoTIFF file containing the classification of the area into inundated and non-inundated classes. An additional option for detecting emergent vegetation (wetland) areas is also offered.

HydroMap module:

- Input: A time series of inundation maps (watermasks)
- Output: Hydroperiod as a GeoTIFF file containing the total number of inundated days for the time period (per pixel).

The period considered started from October to September according to the rainfall cycle for the three years: 2017-2018; 2019-2020 and 2020-2021.

Results

Figure 51 shows the water cover mapping for June, 9th 2021.

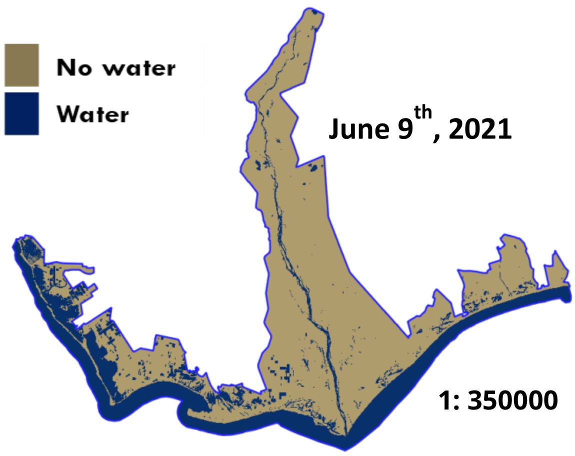

Figure 51. Water Cover mapping of July, 9th 2021 for Nestos study site.

In Figure 52 some temporal trends related to water presence in each year considered are shown.

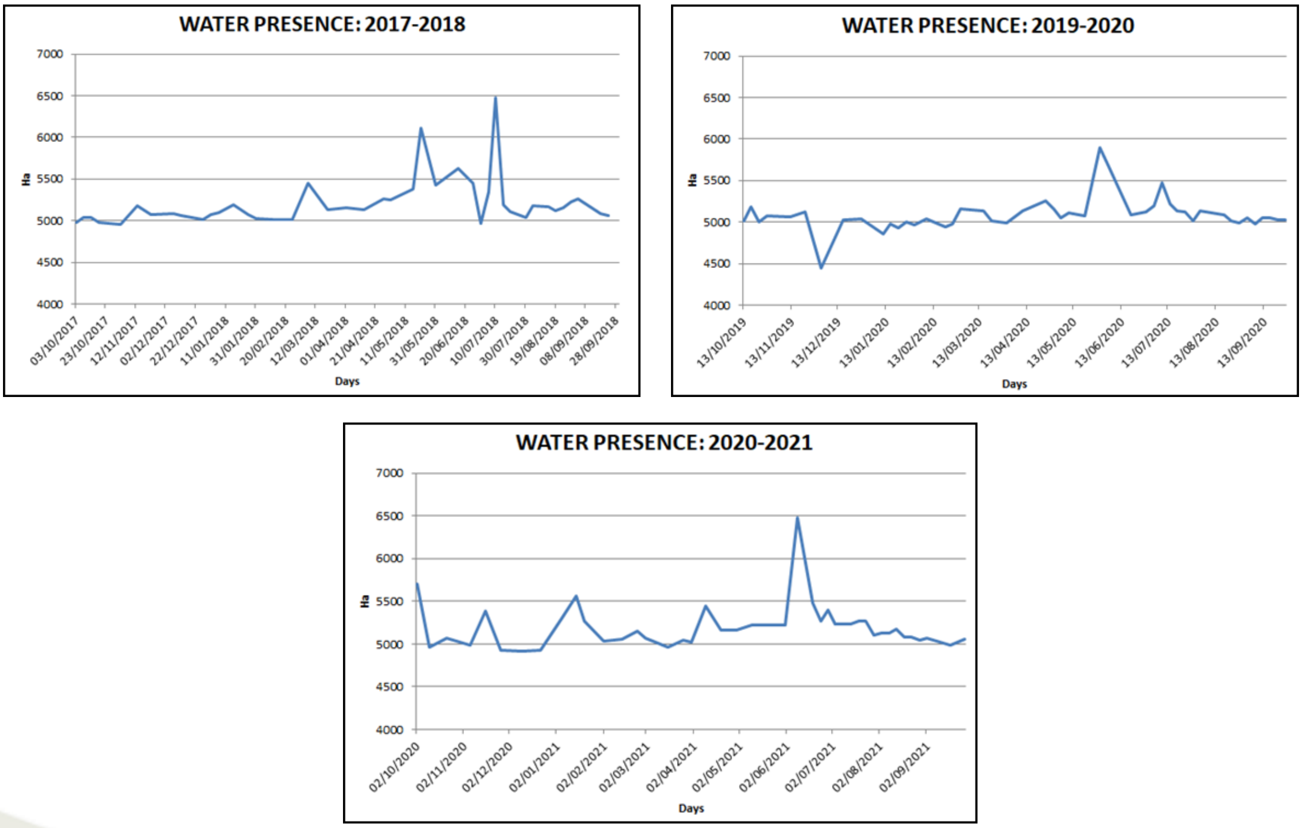

Figure 52. Temporal trend of Water Cover mappings for each year.

Figure 53 shows the comparison of the three temporal trends considered related to water presence in each year and the average annual water presence.

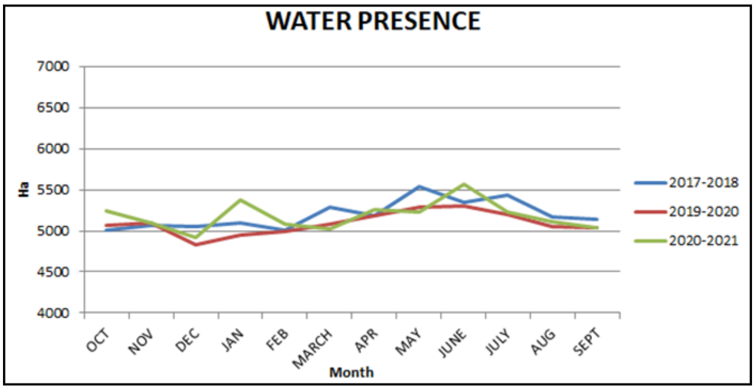

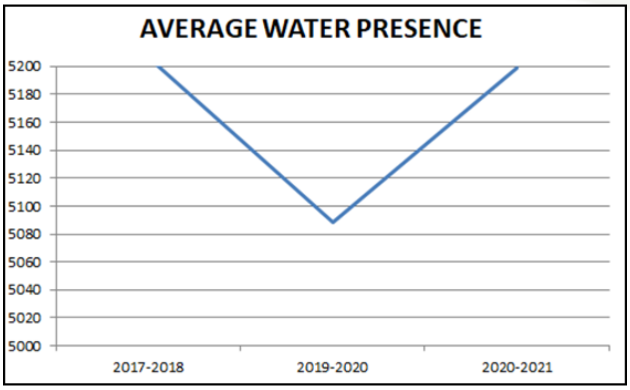

Figure 53. Monthly temporal trend comparison of annual Water Cover mappings for the three years considered.

From the analysis the following results can be assessed:

- The period 2019-2020 registered an average water presence below the average of the previous and successive year;
- December 2019 results particularly poor in terms of water presence;
- The peak of water presence for 2019-2020 remains lower than the other years.

Figure 54 shows an hydroperiod mapping reporting the number of days of the year with water presence for 2020-2021.

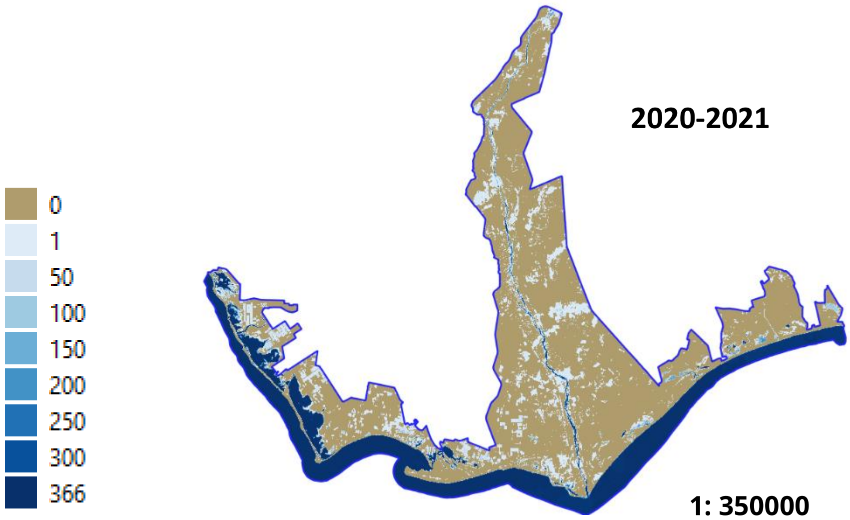

Figure 54. Hydroperiod mapping for 2020-2021

3.1.5 Soil Salinity (SS) temporal trend

Methodology

SS indices mapping was, also, delivered by CERTH-ITI group. Sentinel-2 mission imagery, only for those areas covered by herbaceous vegetation or bare soil in order to extract the soil response, were taken into account for the years 2017 and 2021. Specifically, after producing the LC maps for the study areas and identifying the areas covered by herbaceous vegetation or bare soil, different SS indices from the combination of appropriate spectral band reflectance values, as described in the literature, were computed and consequently SS index maps were produced.

According to the literature, SS indices can be derived from algebraic or Boolean combinations of the reflectance values of the Sentinel-2 mission bands. The following 5 indices were calculated and compared (non-exhaustive list of possible types, see Deliverable A2.1):

- SS Index-1 (SSI1) = $\sqrt{GREEN\ (520-600nm) * RED(630-690nm)}$
- SS Index-2 (SSI2) = $2 * GREEN\ (520-600nm) - (RED\ (630-690nm) + NEAR\ INFRARED\ (770-900nm))$
- SS Index-3 (SSI3) = $\sqrt{RED\ (630-690nm)^2 * GREEN\ (520-600nm)^2}$
- SS (SI) = $\frac{(GREEN\ (530-590nm) * RED\ (640-670nm))}{BLUE\ (450-510nm)}$
- Adapted SS Index (SASI) = $\frac{RED\ (630-690nm)}{100 * BLUE\ (450-520nm)^2}$

where BLUE, GREEN, RED, NEAR INFRARED are the values of reflectance of each pixel at the corresponding wavelengths, as they are mentioned in the parentheses.

The acquisition date of Sentinel-2 images considered are reported in Table 18:

Table 18. Date of satellite imagery considered for SS index computation.

Year	Acquisition date	Sensor	Spatial resolution (m)
2017	August, 14th	Sentinel-2 A/B	10
2021	September, 2nd		

Results

All the different SS indexes seem having the same signal dynamics, hence, SI was preferred for its formulation as a ratio, so it can allow a sort of balance between the bands.

Furthermore, it considers the more common spectral bands combination (GREEN*RED) among the indices analysed. SASI differs from the other for its values less than 1.

Figure 55 shows the two SS index mappings extracted.

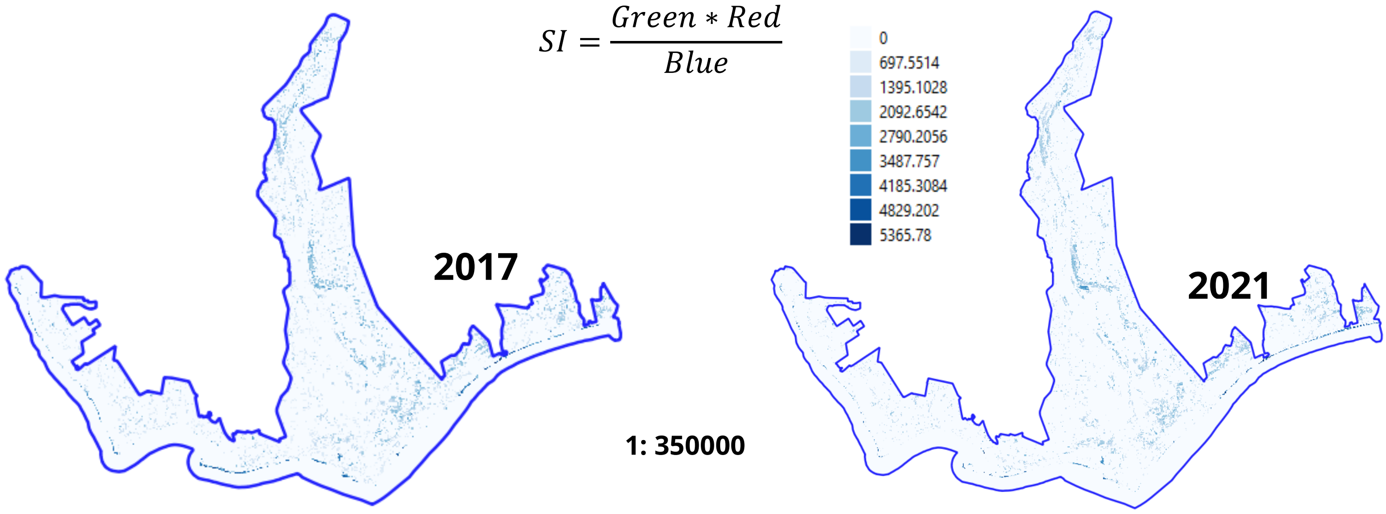

Figure 55. Temporal trend comparison of annual Water Cover mappings for the three years considered.

From the mappings the highest values of SS can be appreciated in several areas along the river as well as along the sea coastline.

3.1.6 SOC temporal trend

Methodology

The extraction of SOC temporal trend was performed by following the same procedure as for Alta Murgia site (section 2.1.5).

Results

The periods reported in Table 19 were considered for SOC temporal trend mappings.

Table 19. List of periods considered for the SOC temporal trend mappings and results. The percentage is related to the whole dry land (21027 ha).

Period	Spatial resolution (m)	Objectives	Degradation	Improvement
2000-2021	30	long-term monitoring	1928 ha (9.17%)	1815 ha (8.63%)
2000-2017		before meteo dry conditions (2017) effects	1581 ha (7.52%)	1630 ha (7.75%)
2017-2021	10	short-term monitoring/after meteo dry conditions (2017) effects	38 ha (0.2%)	132 ha (0.65%)

Figure 56 shows the SOC temporal trend mappings produced.

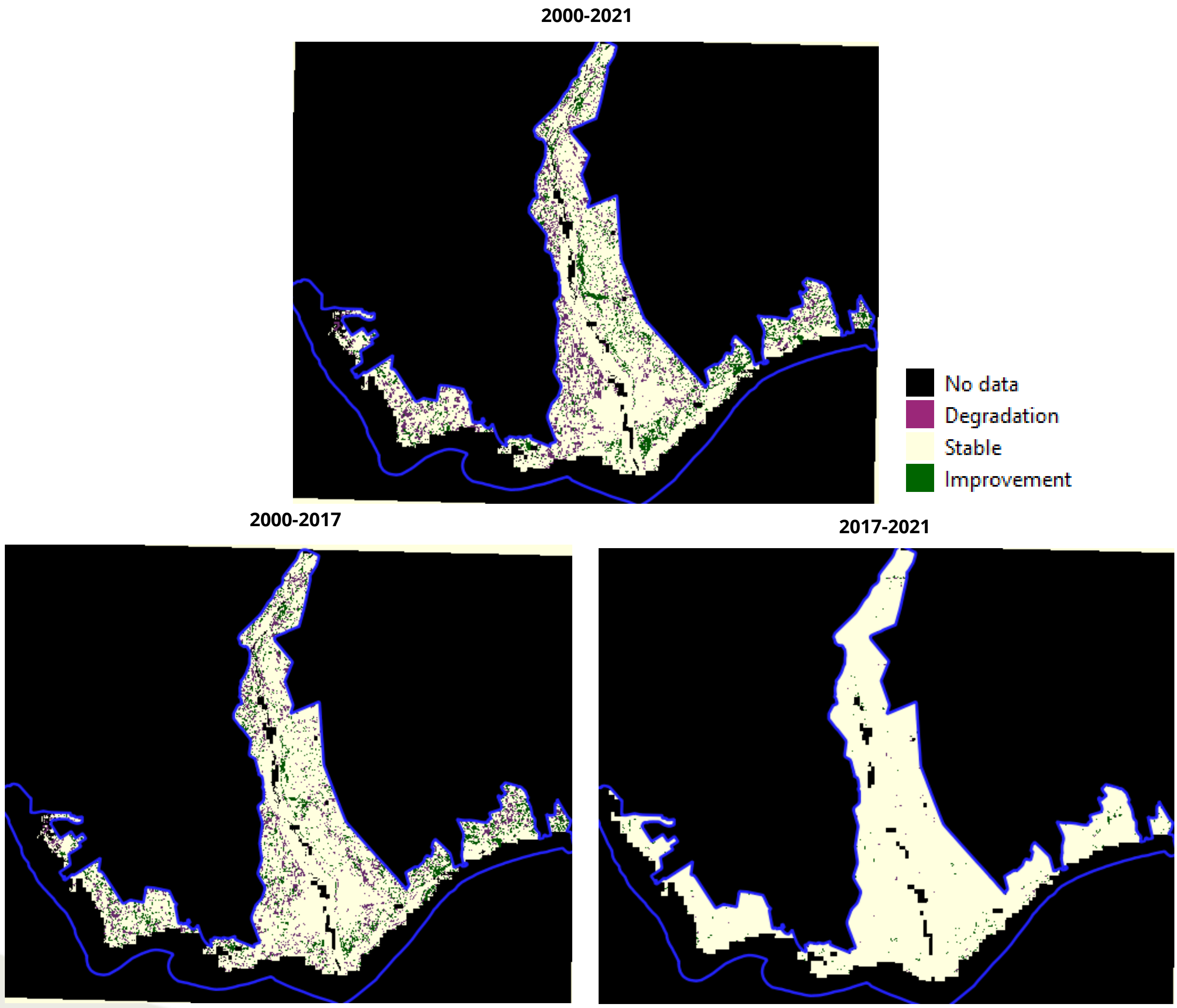

Figure 56. SOC degradation mappings produced for Nestos.

The following considerations can be obtained:

- On long-term period, from 2000 to 2021, high SOC degradation can be evaluated;
- The main degradation happened from 2000 to 2017.

3.1.7 SDG 15.3.1 computation and land degradation mapping

Methodology

In the computation of SDG 15.3.1 indicator for Nestos trend in LC, PP, SOC, HP and SS were considered.

Hence, SDG 15.3.1 indicator computation for Nestos followed the same steps described in sub-section 2.1.6 with the following specific choices:

- temporal ranges to be monitored: 2000-2017 (period before meteo dry conditions of 2017) and 2017-2021 (period after meteo dry conditions of 2017);
- a spatial scale of 30-meters;
- only the trend for NATURAL_RIPARIAN_FOREST_DECIDUOUS_HABITAT_91E0 (the class of main interest) was considered;
- for the additional sub-indicators, the following range values were considered:
  - ✓ HP mapping: all the pixel with values lower than 240 days (corresponding to 8 months without water) were considered degraded (dry areas) even though information about specific month and quantity of meteo precipitations would be required;
  - ✓ SS mapping: all the pixel with values greater than 1000 (empirically corresponding to areas along the sea coastline) were considered degraded (dry areas);
- A(Total) is the total riparian forest at t_0=2000.

Starting from Pheonology data and using the mean annual output we can estimate PP for SDG 15.3.1 computation. As for phenology we keep separate the river itself from the coast. Over the

6 years available with HR-VPP we defined as baseline the first 3 (2017-2019) and under analysis the second group of 3 (2020-2022)

The coast has a strong change of habitat riparian forest 55% that disappear between LC mappings for 2017 and 2022.

This large change does not impact the productivity sensu 15.3.1 where in fact the vast majority of pixel, more than 90% stay with a stable outlook.

Table 20. Percentage of pixels of riparian forest in the three categories (only 2021, [01], only 2017 [10] or present in both survey [11]).

	Hectares
01	0.554578
11	0.244219
10	0.201203

Table 21. Percentage of pixels in the different score categories across the 3 riparian forest categories along the coast.

		01	10	11
Productivity	**-1.0**	4.69	7.15	5.21
	0.0	91.73	91.00	91.54
	1.0	3.59	1.85	3.26
Trend	**-1.0**	0.92	3.99	1.72
	0.0	95.50	94.17	95.02
	1.0	3.59	1.85	3.26
State	**-1.0**	1.37	0.68	0.23
	0.0	78.41	86.78	96.18
	1.0	20.22	12.54	3.59
Performance	**-1.0**	53.22	57.19	49.17
	0.0	46.78	42.81	50.83

For the river part the outlook is more problematic, with 60% of pixel that have lost in productivity and only 3% that have some gain. The impact of change of LC do not impact this signal.

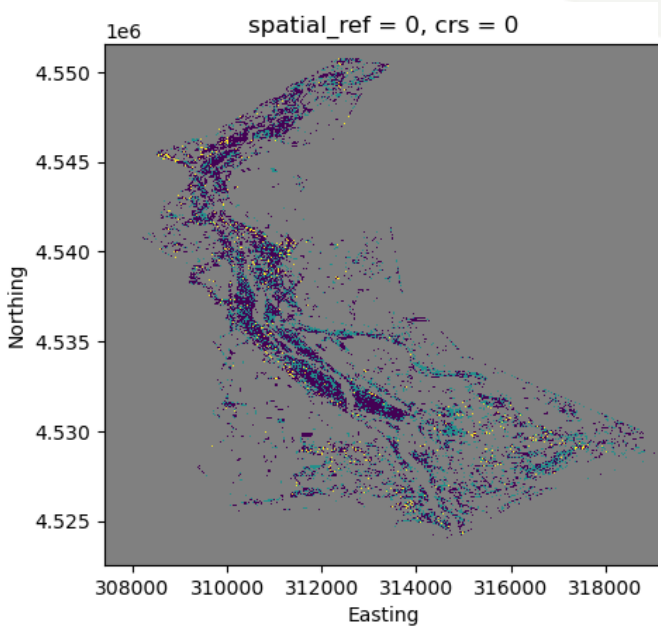

Figure 57. The State sub-indicator.

Table 22. Percentage of pixels in the different score categories across the 3 riparian forest categories along the river.

		01	10	11
Productivity	**-1.0**	58.19	59.23	64.64
	0.0	37.79	37.72	32.34
	1.0	4.02	3.05	3.03
Trend	**-1.0**	58.19	59.23	64.64
	0.0	37.79	37.72	32.34
	1.0	4.02	3.05	3.03
State	**-1.0**	60.03	61.93	67.46
	0.0	35.84	34.27	29.24
	1.0	4.14	3.79	3.30
Performance	**-1.0**	56.56	43.19	29.55
	0.0	43.44	56.81	7.045

Results

The degradation mappings for the different periods considered are reported hereafter.

1. For the period 2002-2017 the degradation mapping is shown in Figure 58:

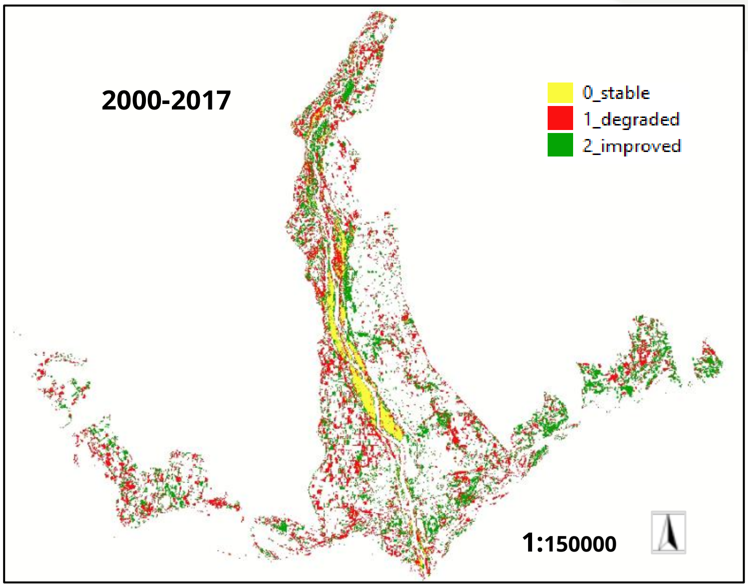

Figure 58. LD mapping for Nestos for the period 2000-2017.

The resulting SDG 15.3.1 indicator percentage was equal to 69.05%.

2. For the period 2017-2021 the degradation mapping is reported in Figure 59:

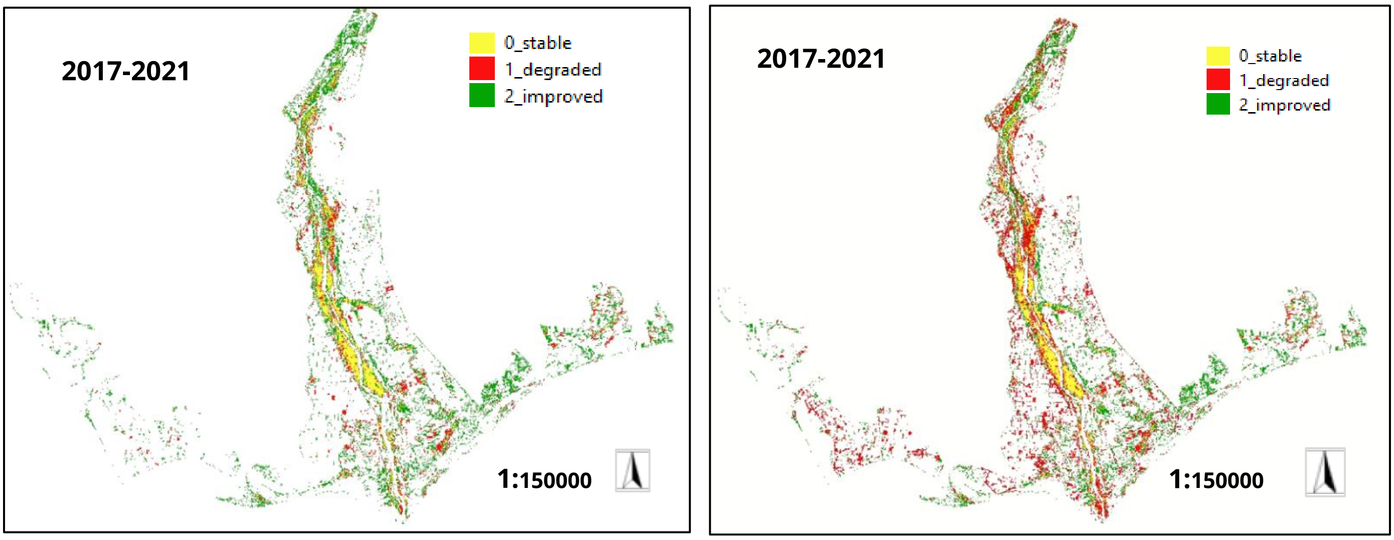

(a) (b)

Figure 59. LD mapping for Nestos for the period 2017-2021. (a) Mapping without "Persistent Degraded"; (b) Mapping with "Persistent Degraded".

The resulting SDG 15.3.1 indicator percentage was equal to 50.80% for Figure 59.a and to 52.38% for Figure 59.b.

3.2 Asterousia (Greece)

The Asteroussia Mt range is located along the southern coastline of Crete. Four subset areas will be analysed in the project (red boundaries in Figure 60).

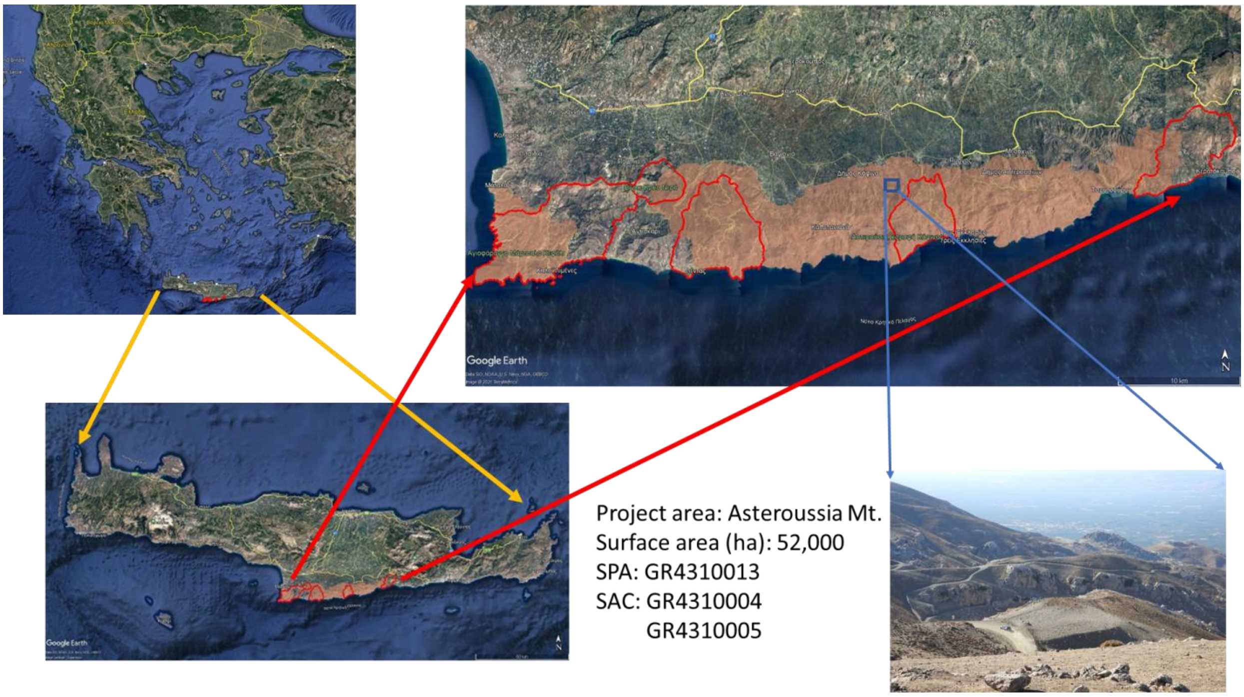

Figure 60. Asterousia site. The four subset areas analysed are overlaid in red boundaries.

The most important land cover types are natural grasslands, sclerophylous vegetation, transitional woodland-shrubland, and sparsely vegetated areas. Natural vegetation consists mainly of shrubs and some isolated maquis and pine forests. In areas with relatively deep soils, old vineyards and continuously expanding greenhouses and olive groves are present.

The Asteroussia Mt range climatic conditions, with long, dry summers and high evapo-transpiration rates, favor desertification. The loss of productive, arable land from soil erosion and degradation and the over exploitation of aquifers are among the key factors posing a desertification risk for the site which is, subsequently, further intensified by climate deregulation and raising global temperatures.

The key pressures and main land degradation processes affecting the study area are: a) decline in vegetation cover/biomass and over grazing resulting from the increase of livestock numbers; b) landscape modification, soil erosion and soil organic matter decline due to anthropogenic interventions such as installation of new olive groves and greenhouses, opening of new roads, expansion of coastal tourism settlements, installation of Renewable Energy Sources facilities; c) accidental or intentional (for scrubland clearance) wildfires; d) hydrological modification; e) soil salinization due to overexploitation of aquifers.

The following indices and sub-indicators, reported in Table 23, has been selected.

Table 23. Indices and sub-indicators selected for Asterousia study site.

Sub-indicators		Sensor	Spatial resolution (m)	Spatial frame	Temporal frame
LAND COVER MAP* BURN SEVERITY MAP*		Landsat	30	4 sub-areas within N2K	2000; 2005; 2010
		Sentinel-2	10		2017; 2021
PRIMARY PRODUCTIVITY	**VEGETATION PHENOLOGY INDEX (NDVI)**	MODIS	250		2000-2021
SOIL SALINITY INDICES		Sentinel-2	10		2017; 2021

3.2.1 LC temporal trend

Methodology

The analysis of land cover maps has been carried out for the years 2000, 2005, 2010, 2017 and 2021. They have been generated by automatic classification processes of images obtained from Landsat series satellites (mainly Landsat-5 and 8) for the years 2000 to 2017, through their TM, ETM+, OLI and MSI sensors. The 2021 maps have been generated using Sentinel-2A and 2B data (tile 31TCG) and the same classification methods (González-Guerrero et al., 2019).

Three types of algorithms have been tested, EODESM, ClasMix and kNN. Best results have been obtained from kNN classification. Therefore, these images, as well as the vegetation and moisture indices, were classified using the kNN algorithm to obtain a map with 5 categories (Table 24): Bare soil, Crop, Dense woody vegetation, Sparse woody vegetation and grassland. For the training of the classifier and the subsequent validation of the output map, a set of training and test areas collected by visual interpretation of the available orthophotos was considered. Validation of the result of the 2021 LC map was performed by computing a confusion matrix to evaluate the result of the classification (Table 25).

Table 24. Categories of the cover map.

Name category	Description
Bare soil or rock	Surface covered by rock or soil with no or very limited vegetation.
Crop	Cover corresponding to agricultural crops mainly without large woody vegetation.
Dense woody vegetation (DWV)	Surface area with abundant woody vegetation (maquis, pine forests, sclerophyllous vegetation and old tree crops)
Grass	Area with a predominance of pastures and no woody vegetation.
Spears Woody vegetation (SWV)	Surface with presence of scattered woody and sclerophyllous vegetation.

Results

Table 25 reports the confusion matrix obtained for validation of LC mapping for 2021.

Table 25. Confusion matrix for Asterousia LC of 2021.

	Bare soil Rock	Crops	DWV	Grassland	SWV	Total	Commission error	User accuracy
Bare soil Rock	1723	156	0	92	456	2427	29.01	70.99
Crops	16	146	1	33	55	251	41.83	58.17
DWV	0	0	420	28	46	494	14.98	85.02
Grassland	0	5	5	5	196	211	97.63	2.37
SWV	18	7	74	30	2866	2995	4.31	95.69
Total	1757	314	500	188	3619	6378		
Omission error	1.94	53.5	16	97.34	20.81		Overall success:	80.90%
Producer accuracy	98.06	46.5	84	2.66	79.19		Kappa Index:	0.69

The analysis of temporal LC trends performed in this area shows the following trends for the specific LC categories (Figure 61). The detail of the cover mapping for 2021 can be seen in Figure 62.

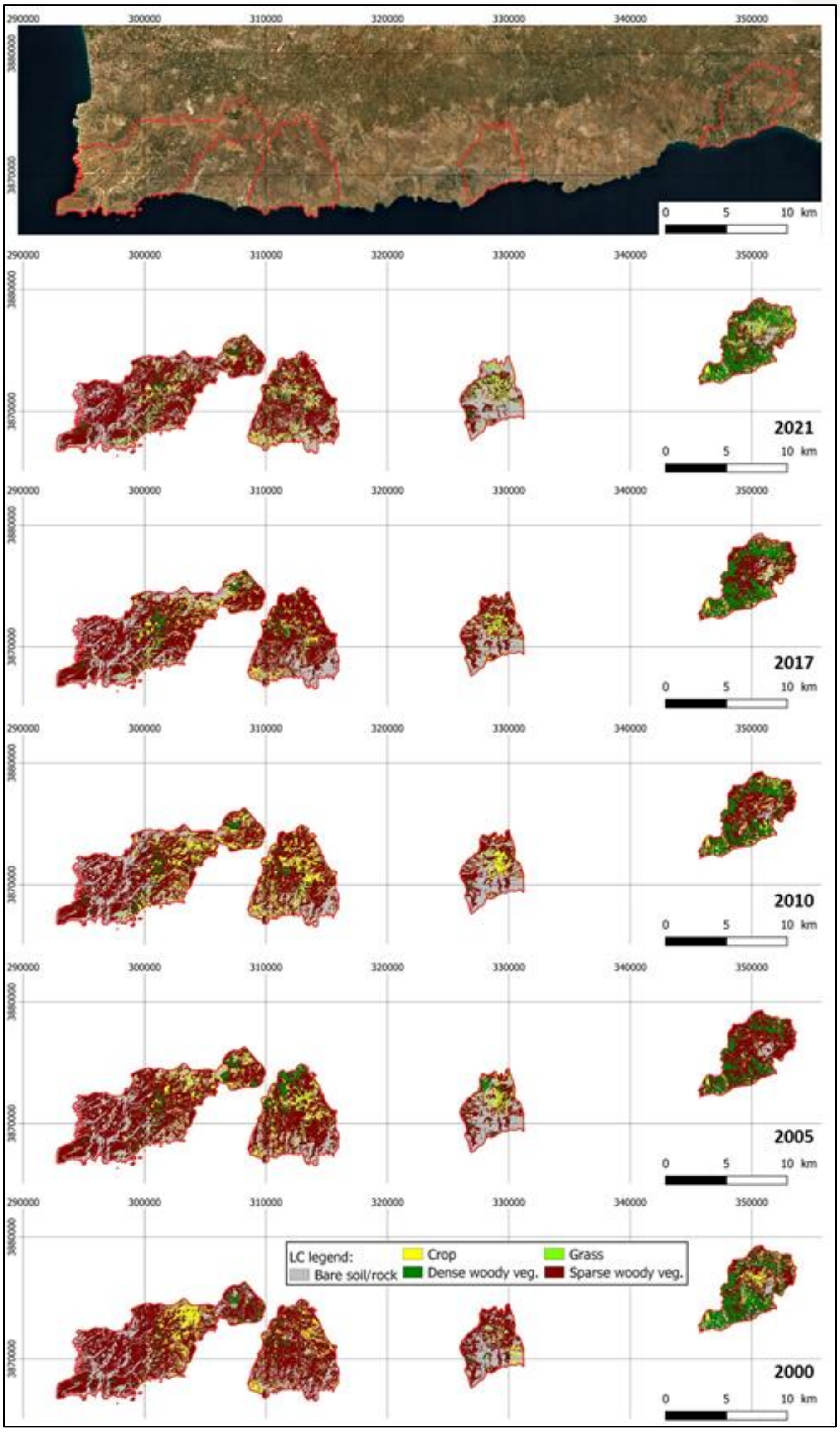

Figure 61. Land cover maps generated. Background image: cloudless Sentinel-2 composition 2021.

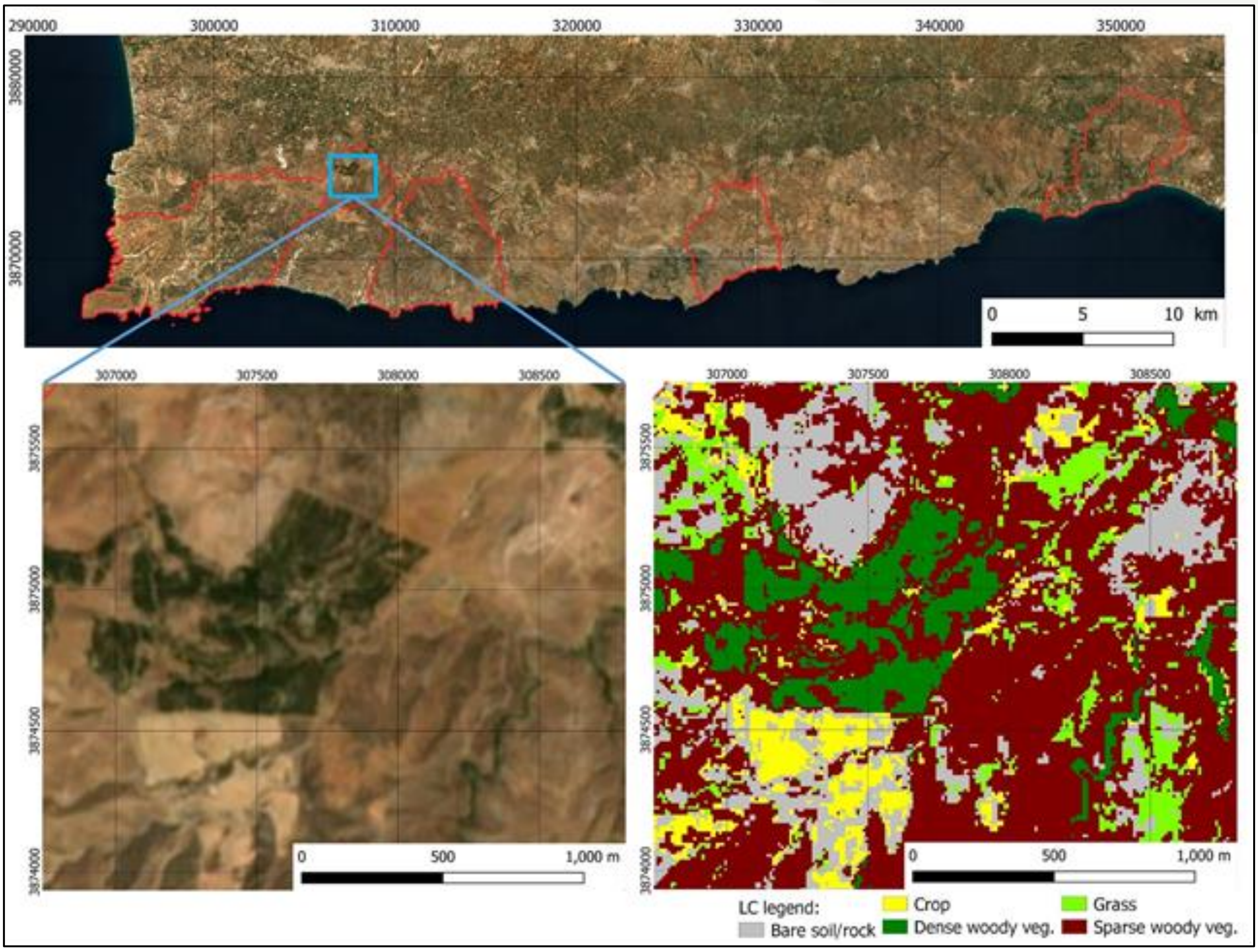

Figure 62. Detail of the LC map for 2021 in the Δάσος Τρυπητών/Trypiton Forest sector. Background image: cloudless Sentinel-2 composition 2021.

From the temporal trend analysis (Figure 63 and Table 26) for the LC classes, the following considerations can be evaluated:

- In general the predominant cover is SWV, with a decay of occupancy over time, while bare ground or rock cover, increases in area over time;

- There is an increase in crop fields in 2010, where it coincides with a decrease in grassland and sparse woody vegetation;

- The dense woody vegetation category is maintained with a slight increase in area in 2021, as well as the grassland category;

- As shown in the confusion matrix, the grassland category is confused with the bare soil, crop fields and sparse woody vegetation categories.

Table 26. LC categories (ha) for each year at Asterousia pilot area.

	2000	2005	2010	2017	2021
Bare soil Rock	3228.93	3574.71	3559.5	3716.37	4420.70
Crops	1894.23	1505.88	2389.41	1431.54	1221.51
DWV	1627.56	1594.44	1622.97	1757.43	1923.74
Grassland	102.33	246.15	93.87	238.41	618.89
SWV	9431.19	9363.06	8618.49	9094.05	8053.29

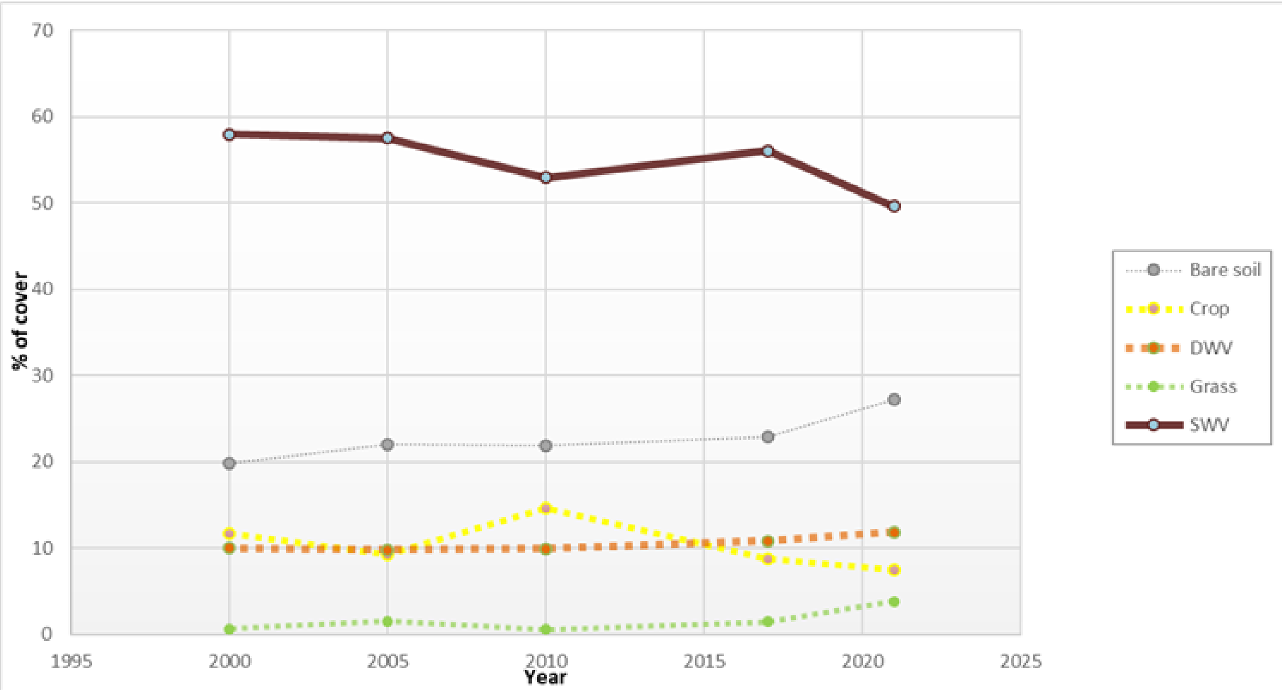

Figure 63. Temporal trend of LC classes presence.

This research also showed that automatic classifications based on EODESM system (http://www.ecopotential-project.eu/products/eodesm.html) in this type of areas present very low thematic detail. For these areas, it is recommended to use other classification systems such as kNN or ClasMix approach, although these algorithms require training areas and test areas that are not always available, specially from the past. In this case, the lack of validated training data returned low accuracy maps for some categories that are essential for monitoring degradation, although the overall accuracy was 80%.

3.2.2 PP temporal trend

Methodology

Primary productivity trends have been computed using *Trends.Earth* plugin for QGIS, based on MODIS annual product (MOD13Q1) at 250 m spatial resolution for the period 2000-2021.

Results

The results show that only for one of the sub-areas, productivity trend is on degradation process (Figure 64).

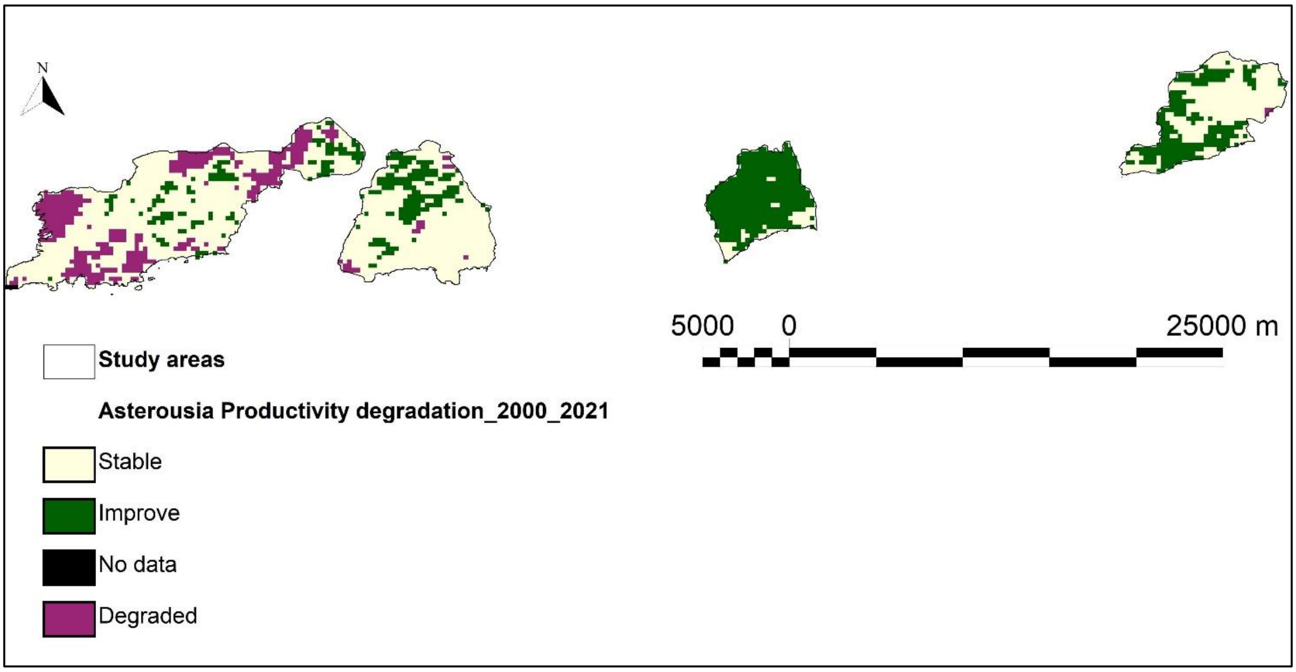

Figure 64. PP temporal trend for the period 2000-2021.

3.2.3 SS temporal trend

Methodology

Production of SS index maps has been done by CERTH-IT taking into account data from the Sentinel-2 mission and Landsat-8, specially in those areas covered by herbaceous vegetation or bare soil for years 2017 and 2021. Five different salinity indices were calculated:

- Soil Salinity Index 1 (SSI1), Soil Salinity Index 2 (SSI2), Soil Salinity Index (SSI3), Soil Salinity (SI), Adapted Soil Salinity Index (SASI).

The time period proposed and selected for the calculation of the indices is between mid-August and early September (see Table 27), when the most arid climatic conditions prevail for the study areas.

Table 27. Dates of satellite images received for the calculation of salinity indices.

Satellite images and sensor	Study area	Date
Landsat-8	Asterousia	02.09.2017
Sentinel-2	Asterousia	25.08.2021

Results

SS indexes present different sensitivity to the area. While SASI results are less sensitive (very small range with values less than 1), SSI1 and 3 are very similar and SS2 is slightly different presenting less accurate results (Figure 65). SI results are similar to SSI1 and SSI3 but more contrasted, so it is recommended as the performance index. In addition, SI is preferred for its formulation as a ratio, so it can allow a sort of balance between the bands. Furthermore, it considers the more common spectral bands combination (GREEN*RED) among the indices analysed.

Figure 65. SI mappings for 2017 and 2021.

From the mappings the highest values of SS can be appreciated in 2017 mainly located along the sea coastline and partially along river course.

3.2.4 SOC temporal trend

Methodology

The computation of SOC trend for a given period is estimated from the LC changes identified in this period and adjusted based on the *SoilGrids* SOC data from 2016. Since the accuracy of LC classifications obtained is quite low, the results obtained for the SOC will also include a high uncertainty and will not be reliable.

Therefore, it is recommended that SOC trends will only be computed if LC maps present good accuracy indicators.

3.2.5 SDG 15.3.1 computation and land degradation mapping

Methodology

The calculation of SDG 15.3.1 for Asterousia is modified based on the procedure included in the UNCCD guidelines, since no SOC trend is available. Therefore, SDG has been computed only considering 2 sub-indicators for the period 2000-2021, the LC trend and the PP trend containing 3 categories: *stable, improved, degradation*. LC sub-indicator has been computed using the baseline maps presented in section 3.2.1 at spatial resolution of 10 m. PP has been computed using *Trends.Earth* plug-in for QGIS software, based on MODIS annual product (MOD13Q1) at 250 m spatial resolution. In order to proceed with the integration of the 2 sub-indicators, PP sub-indicator has been resampled to 10 m using nearest neighbour algorithm, since it is a categorical map.

The SDG 15.3.1 indicator presents 3 categories: *Loss, Gains and No change*. The sub-indicators integration decision criteria were based on the "*one-out, all-out*" rule. If any of the two sub-indicators presented *degradation* for a given pixel, the final category should be *Loss*.

Results

The land degradation mapping obtained for 2000-2021 for Asterousia is shown in Figure 66.

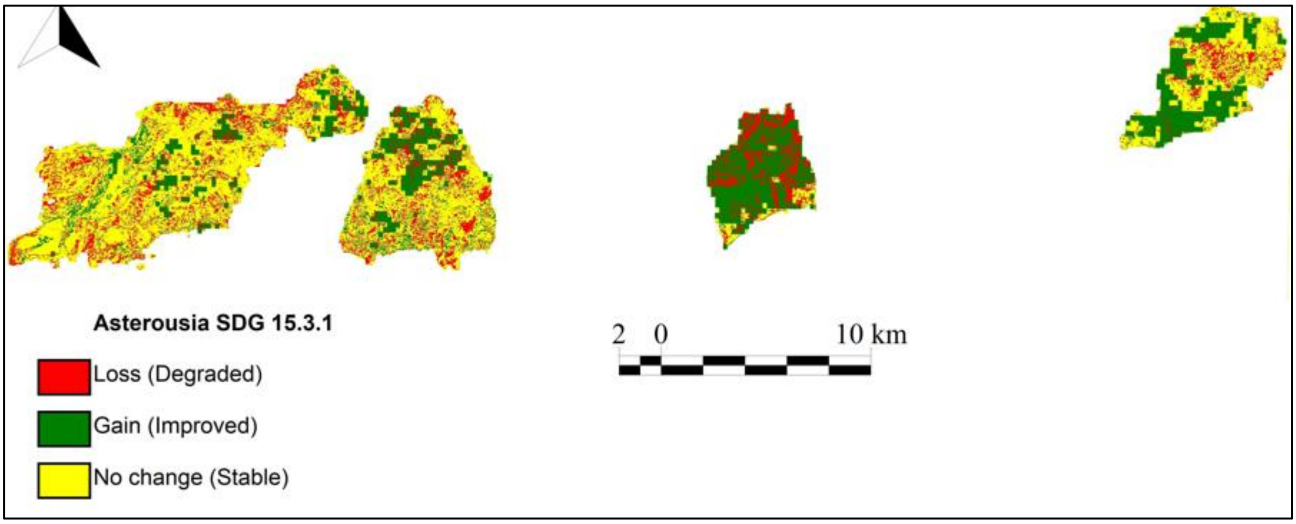

Figure 66. Modified SDG 15.3.1 indicator for Asterousia region for 2000-2021.

Once the indicator obtained, the proportions of land that is degraded over the total land area was also computed. A 27.19% of the area present degradation for the period 2000-2021, a 53.02% present improvement and the rest 19.74% do not present changes in terms of degradation.

4.1 El Bruc (Spain)

The regions of Anoia and El Bages suffered a serious fire in July 2015, which burned 1,235 ha around the municipality of El Bruc, on the perimetral area of the Montserrat Natural Park (included in the Montserrat-Roques Blanques-riu Llobregat N2K site, with code ES5110012). The area affected by the fire is located in the central area of Catalonia (Spain) (Figure 67), characterized by a dry sub-humid climate. A large part of the burned forest was an Aleppo pine forest, which had already suffered a fire in 1986. The pines - which do not have a regrowth strategy, but rather germinate - are having a modest and variable regeneration throughout the region. Within the framework of the LIFE The Green Link project (LIFE15 CCA/SE/125), more than 20 ha of forest and agricultural species were planted (>4,000 seedlings) to recover the most degraded areas and favour the recovery of the agro-silvo-pastoral mosaic, which helps reduce the vulnerability of the area facing upcoming forest fires (Figure 68).

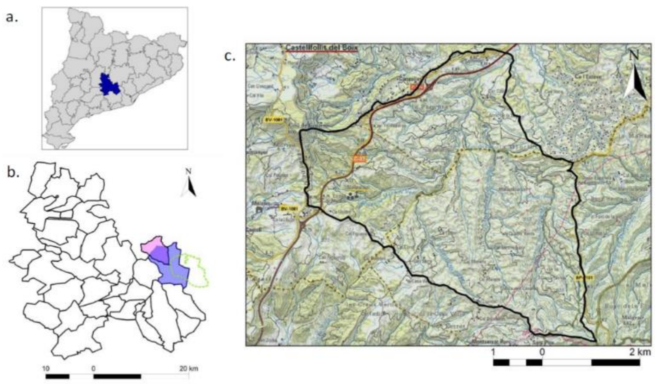

Figure 67. a) General location of Anoia region in Catalonia, Spain; b) Location of “El Bruc” municipality (blue polygon) in the context of Anoia region, Monserrat Natural Park limits (green) and area affected by 2015 forest fire (rose); c) Limits of the area affected by 2015 forest fire represented in 1:50.000 topographic map (ICGC, 2021).

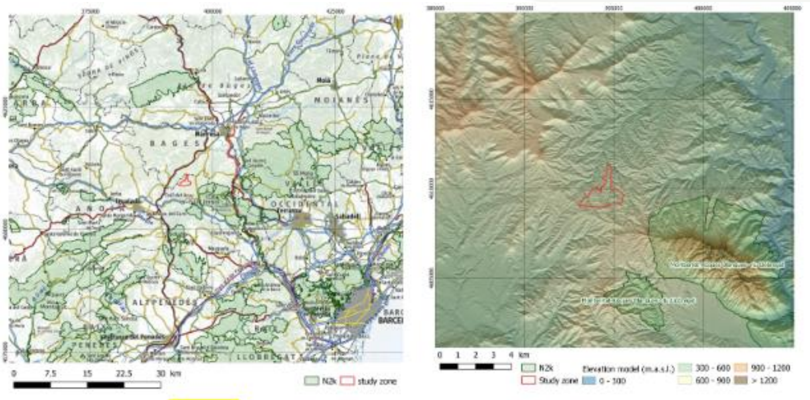

Figure 68. Location, limits (red polygon) and MDE of El Bruc pilot area.

There is an average of less than 50 days of rain per year, with frequent periods of drought and water stress by the plants, which have been increased in recent years. Due to this factor, as well as the high recurrence of forest fires, it presents areas with low natural regeneration and affected by processes of concentrated and diffuse erosion. In addition, like many areas of the Mediterranean, and especially of the Iberian Peninsula, this area is affected by rural abandonment since the beginning of the 19th century, which has caused an expansion of the shrubland and forest, mainly of Aleppo pine, which increases the risk of large forest fires. The clearings in Aleppo pine reforestation not only help the regeneration after fires or other disturbances, but also promote the good structure and dynamics of the forest and the regeneration after severe drought events (Keenan, 2015). A set of indices and sub-indicators were selected to monitor the pressures and processes described above (Table 28).

Table 28. Indices and sub-indicators selected for El Bruc study site.

<table>
<tr><th colspan="2">Sub-indicators</th><th>Sensor</th><th>Spatial resolution (m)</th><th>Spatial frame</th><th>Temporal frame</th></tr>
<tr><td colspan="2" rowspan="2">LAND COVER MAP</td><td>Landsat</td><td>30</td><td rowspan="5">N2K
+5 km
buffer</td><td>1987; 1992; 1997; 2002; 2007; 2012</td></tr>
<tr><td>Sentinel-2</td><td>10</td><td>2017; 2021</td></tr>
<tr><td>PRIMARY PRODUCTIVITY</td><td>PLANT PHENOLOGY INDEX (PPI)</td><td>Sentinel-2</td><td>10</td><td>2017-2020</td></tr>
<tr><td colspan="2">BURN SEVERITY MAP</td><td>Landsat
Sentinel-2</td><td>30
10</td><td>2015</td></tr>
<tr><td colspan="2">SOC</td><td>Landsat/Sentinel-2</td><td>10</td><td>2007-2017</td></tr>
<tr><td colspan="2">STANDARDIZED PRECIPITATION EVAPOTRANSPIRATION INDEX (SPEI)</td><td>Meteorological stations</td><td></td><td></td><td>1950-2019</td></tr>
</table>

4.1.1 LC temporal trend

Methodology

Analysis of land cover maps was performed for years 1987, 1992, 1997, 2002, 2007, 2012, 2017 and 2021. They have been generated by automatic classification processes of images obtained from the Landsat series satellites (mainly Landsat-5/7/8) for year 1987 to 2012, through their TM, ETM+, OLI and MSI sensors and the incorporation of auxiliary information. In the case of the 2007 and 2012 maps this auxiliary information comes from the Urban Map of Catalonia and the DTES Road Chart, as well as from the Forest Fire Cartographic Base of the Department of Agriculture, Livestock, Fisheries and Food and the ICGC LIDARCAT base. Maps of 2017 and 2021 have been generated using Sentinel-2A and 2B data (tile 31TCG) and the same classification methods (González-Guerrero et al., 2019). Bands with native spatial resolution of 20 meters (i.e., B5, B6, B7, B8A, B11, B12) were resampled, by a Nearest Neighbour algorithm, at 10 meters as those native (B2, B3, B4, B8). For 2017 classification, six images distributed between March and September 2017 were selected to obtain a good representation of the phenological dynamics of natural vegetation and crop covers (Moré and Pons, 2007). For 2021 classification, 21 images were considered. Table 29 shows the whole of satellite imagery considered for the 2017 and 2021 classifications with their acquisition dates.

Table 29. List of imagery from Sentinel-2 satellite considered for the LC mappings.

Year	Acquisition date		Sensor	Spatial resolution (m)	Bands/features
2017	March, 17th April, 6th May, 26th	July, 7th August, 14th September, 13th	Sentinel-2 A	10	B2, B3, B4 (Vis) B5, B6, B7 (Red Edge) B8, B8A (NIR) B11, B12 (SWIR) (10 bands) NDVI, NDWI 1 and NDWI2
2021	February, 1st; February, 19th March, 16th March, 23rd March, 31st April, 5th May, 5th June, 9th June, 14th June, 24th July, 14th	July, 19th August, 13th August, 18th August, 28th September, 27th October, 22nd November, 6th November, 18th December, 11th December, 31st	Sentinel-2 A/B		

These images, as well as texture variables, terrain models derived from LIDAR processing and vegetation and wetness indices, were classified using the kNN to obtain a map with 25 categories (Table 30). The categories related to urbanized areas (urban areas, urbanizations and industrial zones/commercial areas), road infrastructures and burned areas were edited using official cartographic datasets of the Catalan Government. A set of training areas collected through visual interpretation of available orthophotos and distributed with a "stratified" sampling to ensure a minimum number of polygons–samples for each class (i.e., stratum) (Congalton et al., 2014) were considered for training the classifier and subsequent validation of the output map.

Results

The results have an overall accuracy greater than 98 %, which was evaluated with a set of more than 8.6 million independent test pixels.

Table 30. LC classes legend.

Road infrastructures	Citrus plantations	Lowland grasslands
Low-density urban areas	Vineyards	Wetland vegetation
High-density urban areas	Sclerophyll forests	Inland waters
Industrial and commercial areas	Deciduous forests	Marine waters
Rainfed herbaceous crops	Needleleaf forests	Permanent snowpacks
Irrigated herbaceous crops	Shrublands	Burned areas
Rice fields	Montane grasslands	Areas with little or no vegetation
Rainfed fruit trees	Middle-altitude grasslands	Sandy areas and beaches
Irrigated fruit trees		

The analysis of temporal LC trends performed in this area shows the following trends for the specific LC categories (Figure 69, Table 31).

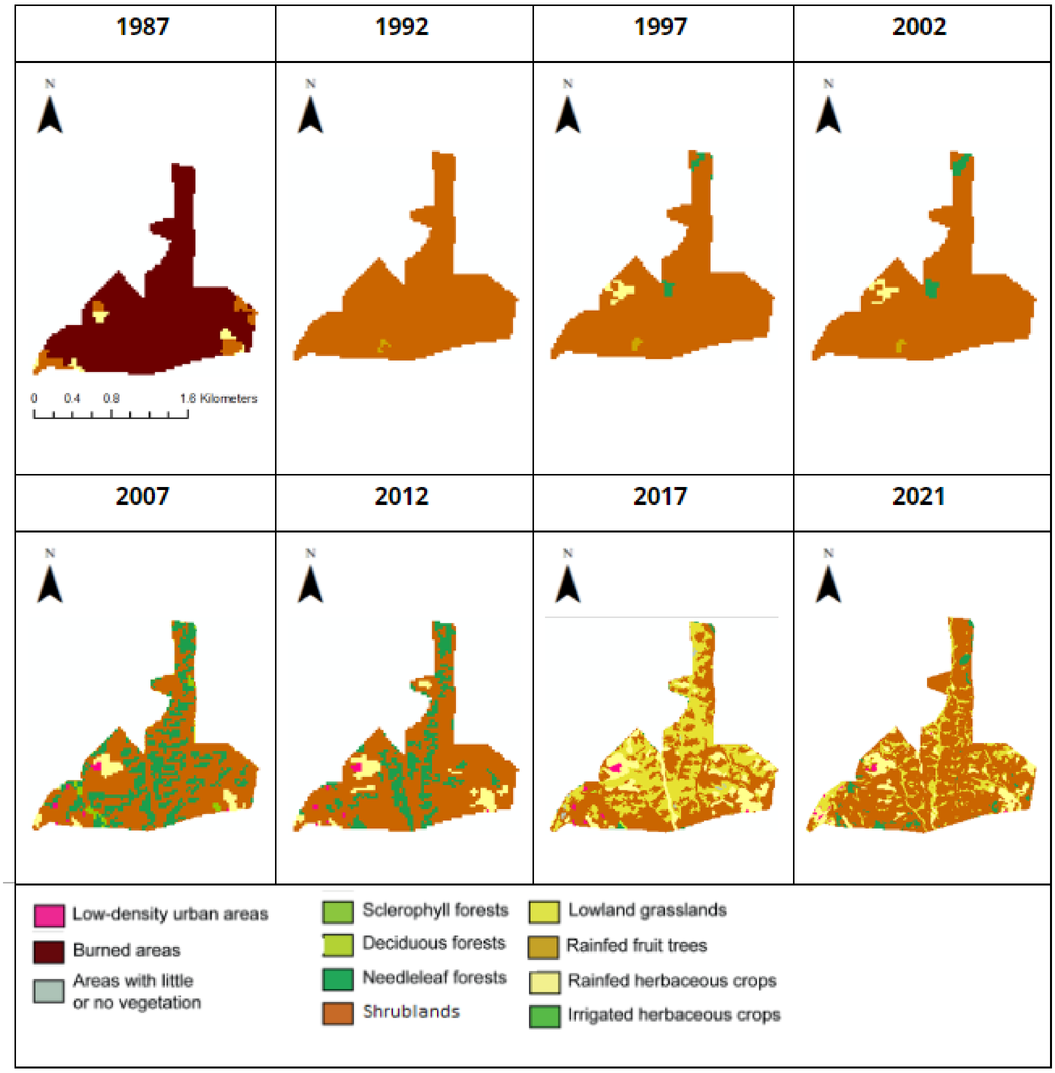

Figure 69. Land cover maps generated.

Table 31. LC categories (ha) for each year at El Bruc pilot area.

CLASSES	FIRE EVENT	1987	1992	1997	2002	2007	2012	FIRE EVENT	2017	2021
Low density urban areas						1.8	1.8		1.77	1.16
Rainfed herbaceous crops		4.95		3.87	3.6	8.55	14.22		28.65	19.52
Rainfed fruit trees			0.9	1.17	1.08					
Irrigated herbaceous crops									0.02	
Shurblands		12.69	223.65	216.18	214.74	146.16	165.33		106.47	162.02
Low altitude grasslands									86.26	36.27
Sclerophyll forests						3.51				
Deciduous forests									0.5	
Needleleaved forests				3.333	5.13	64.53	43.2		0.6	6.53
Areas with low/no vegetation									1.23	
Burned area		206.61								

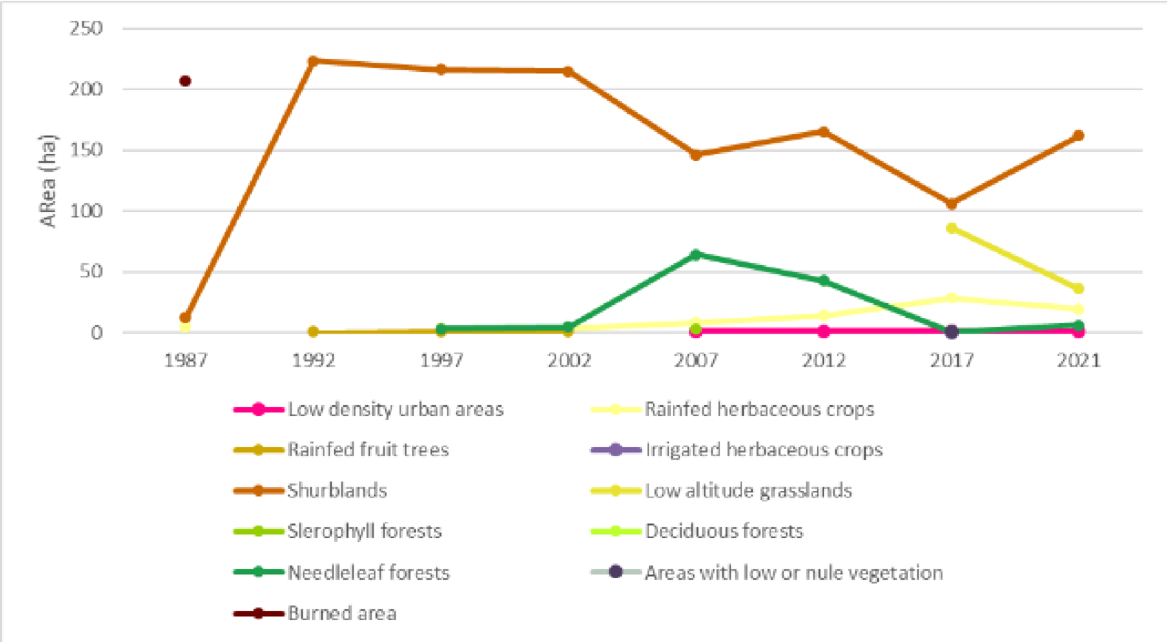

Figure 70. Temporal trend of LC classes presence.

From the analysis of the temporal trend (Figure 70) for the LC classes in the area where restoration practices were performed, the following considerations can be evaluated:

- After both fires in 1987 and 2015, shrublands were progressively recovered after 5 years;
- Increase of shrublands in 2021 agrees with decrease of low altitude grasslands that suddenly appeared after the 2015 fire event;
- Unfortunately, needleleaved forests need more than 15 years to achieve the same mature growth than before the fire-event.
- After 1987 fire, needleleaved forests start to recovery around 2007. Following 2007, two strong drought events occurred, increasing the mortality of such species. Finally, in 2015, the last fire drastically decreased the needleleaved forests of the area.

In terms of Land cover degradation and following the transitions defined by the UNCCD protocol (degradation, stable or Improvement), the evolution of LC of the study area between 2007 and 2017 (before and after the fire event) is showed hereafter (Figure 71):

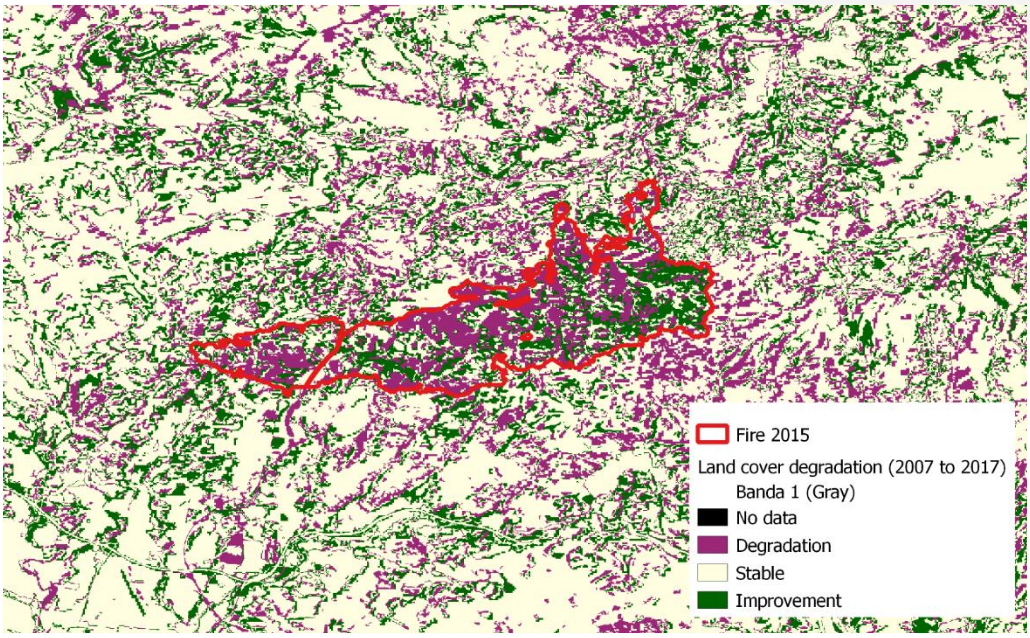

Figure 71. LC evolution in the period 2007-2017.

Changes inside the fire perimeter indicate that around 41% of the area has suffered a degradation process, although in 2017 part of it has already recovered. It is noteworthy that the LC degradation computation using *Trends.Earth* plugin for QGIS reclassifies the original land cover types to 7 categories: grassland, cropland, tree cover, water, artificial wetlands and other lands, but there is not a category related to shrublands or maqui, which should be considered different from tree cover and moreover are a land cover very characteristic for Mediterranean areas.

4.1.2 BS temporal trend

Methodology

El Bruc area suffered a big fire event starting in July, 26th 2015 that affected the study area. An analysis to identify the fire-affected area has been performed using the burn severity mapping, according to Nasery & Kalkan (2020), through the computation of NBR spectral indices (Deliverable A2.1). The NBR has been calculated for a satellite image just before the event and just after the event. Following, the difference between the former and the latter NBRs (dNBR) has been also computed as indicator of burn severity. The analysis has been carried out using both Landsat and Sentinel-2 images, as a way to compare the results. The list of images considered is included in Table 32.

Table 32. List of satellite imagery considered for the BS mappings.

Year	Acquisition date	Sensor	Spatial resolution (m)	Bands
2015	July, 18th August, 3rd	Landsat 8	30	B4 (NIR) B7 (SWIR)
2015	July, 16th August, 2nd	Sentinel-2 A	10	B8A (NIR narrow) B12 (SWIR)

Results

Table 33 and Figure 72 show the different burn severity levels and the mappings obtained.

Table 33. Classification table of severity level based on dNBR range.

SEVERITY LEVEL	dNBR RANGE
Enhanced Regrowth	< -.1
Unburned	-.1 to +.1
Low Severity	+.1 to +.27
Moderate Severity	+.27 to +.66
High Severity	> .66

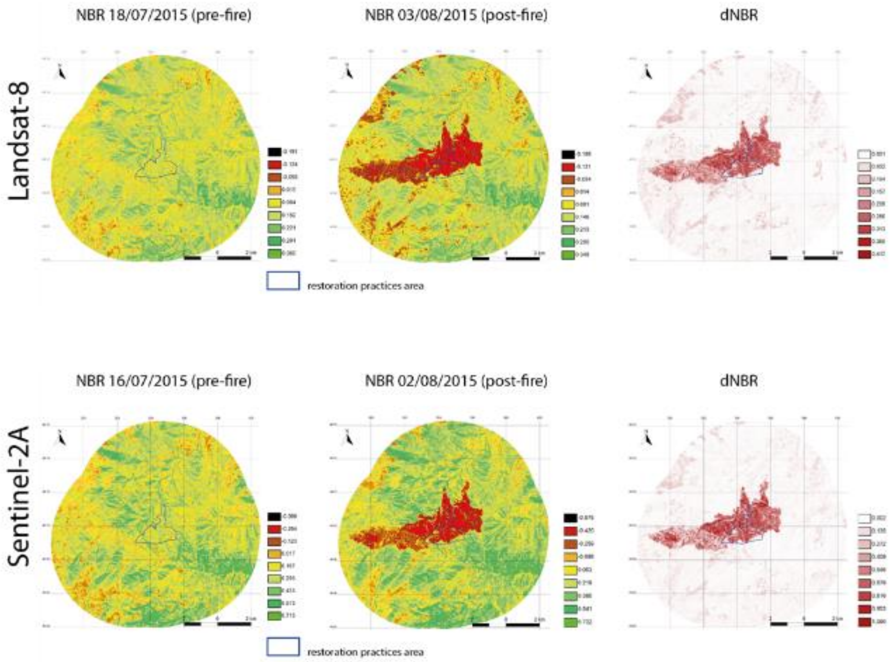

Figure 72. BS mapping for Landsat- 8 on July, 18th 2015 (pre-fire) and August, 3rd 2015 (post-fire) and Sentinel-2 (pre-fire) and (post-fire).

From the analysis of the burn severity mapping, it can be concluded:

- The whole restoration area was affected by the 2015 forest event;
- The severity level of forest event in the restoration area was from moderate to high severity;
- NBR computed based on Landsat data or Sentinel data shows significant differences. These differences might be due to the differences of the atmospheric corrections applied to the different sensors. Sentinel-2 derived data shows higher values than Landsat data;
- The NBR index can be a powerful tool to identify pixels that have a high likelihood or being “burned” but it also shows false positives that should be considered.

4.1.3 PP temporal trend

Methodology

PP has been analysed based on the Copernicus HR-VPP product. TPROD for the 4 available years (2017-2020) has been downloaded from WeKEO platform and combined with the area of the study to monitor its productivity trends. First year of analysis correspond to 2017, two years after the fire event. Unfortunately, since these data is derived from Sentinel-2, data prior 2017 (launch time) is not available.

Results

Figure 73 illustrates the TPROD product and Table 34 and Figure 74 quantitatively analyse the results.

Table 34. Statistics of all pixels included in the study area.

	2017	2018	2019	2020
Mean	447.8692	773.5122	719.0976	989.9331
St. Dev	266.2838	368.8852	323.5487	396.0033
Minimum	0	0	2	37
Maximun	3689	3692	3717	3733
1st quartile	290	559	515	733
Media	393	762	671	945
3rd quartile	519	982	880	1202

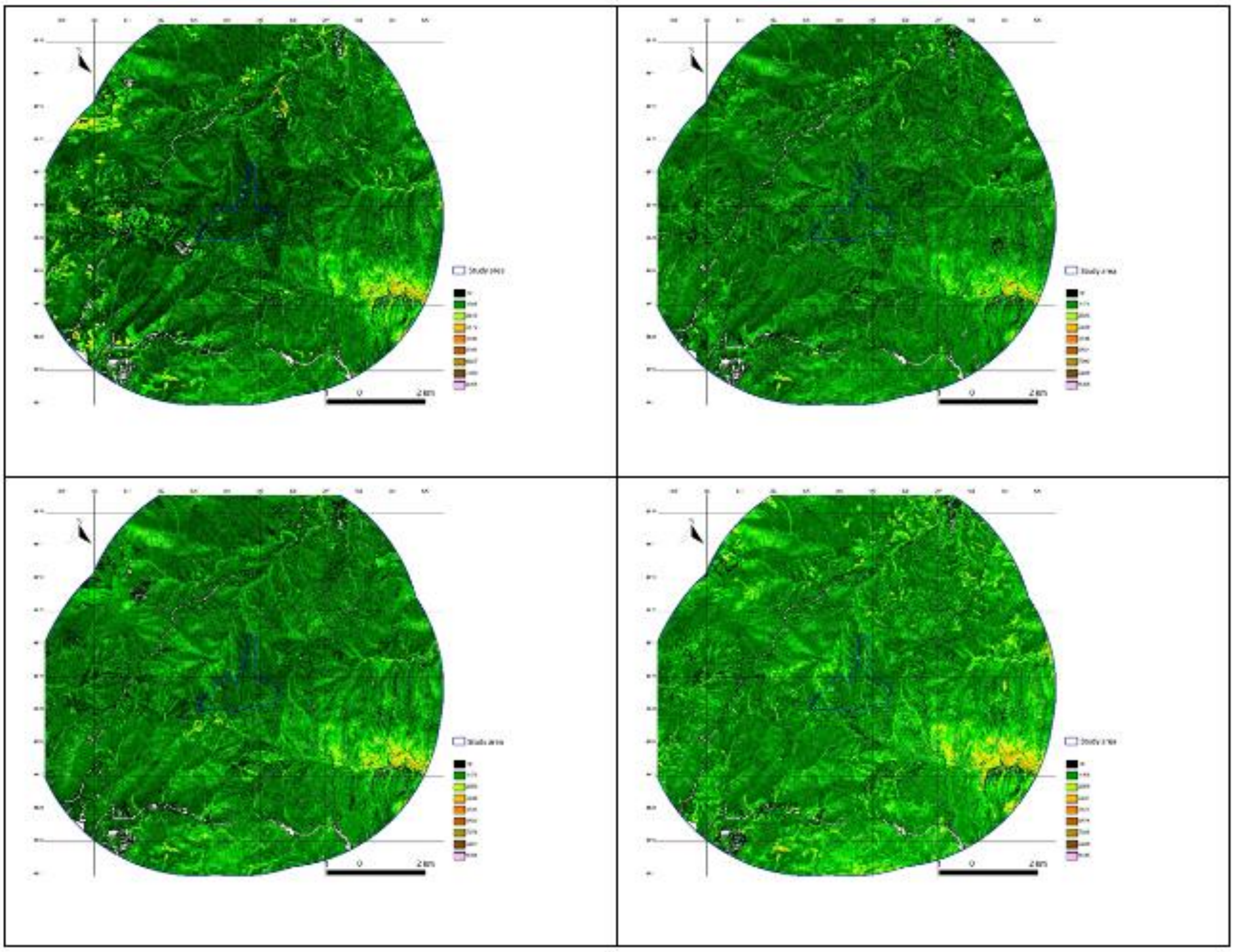

Figure 73. TPROD. The growing season integral computed as sum of all daily values minus their base level value (units: PPI * day).

The trend of productivity clearly increases with time (R^2=0.80). An important aspect to highlight is that although the minimum and the maximum productivity values remain almost constant, the 1st and 3rd quartiles increase significantly with time. This is an indicator of recovery of vegetation in the area.

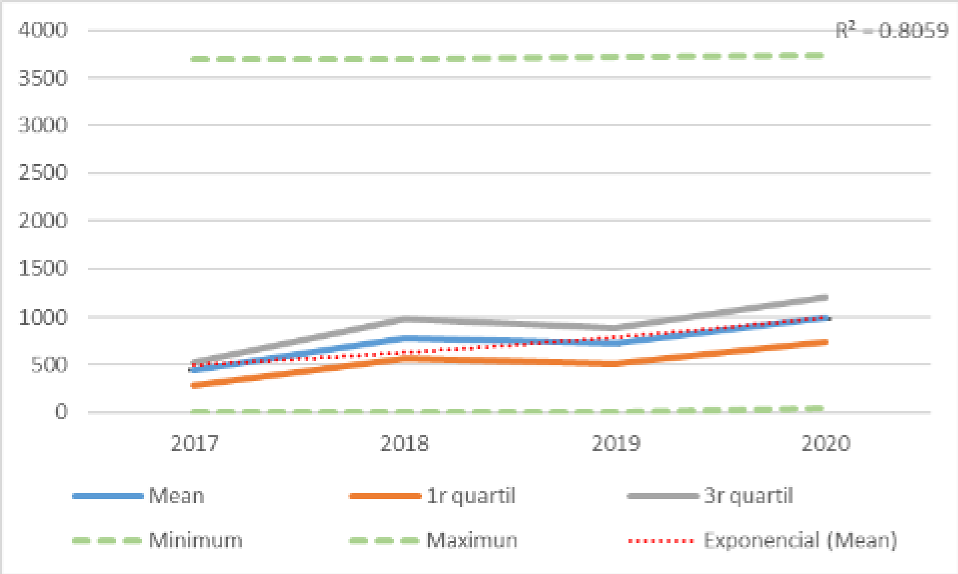

Figure 74. Trends of mean, min, max, 1st quartile and 3rd quartile of TPROD of the area.

From the analysis of TPROD, it can be concluded that:

- HR-VPP TPROD is an interesting product to monitor the evolution of a degraded vegetation area;
- This product demonstrates that data derived from Sentinel-2 is sensitive enough to vegetation productivity changes and should be considered as an essential indicator for monitoring desertified areas.

4.1.4 SPEI temporal trend

Methodology

The evaluation of SPEI for El Bruc has also been performed as an indicator of water availability for vegetation and for monitoring the phenomena of dryness by evaluating three different time monthly scales (3, 6 and 12-months) (Figure 75). This index is based on the ratio between precipitation and potential evapotranspiration. Original data belongs to hundredths of meteorological stations located in Catalonia collecting precipitation and temperature from 1950 to 2019 (Domingo-Marimon, 2016). Precipitation and mean temperature data have been interpolated at 100 m spatial resolution for the full region (32,000 km^2) and spatialized data used to compute the SPEI index.

Results

The independent test result RMSE had a median of 23.5 l/m^2 for precipitation and 1.2ºC for mean temperature.

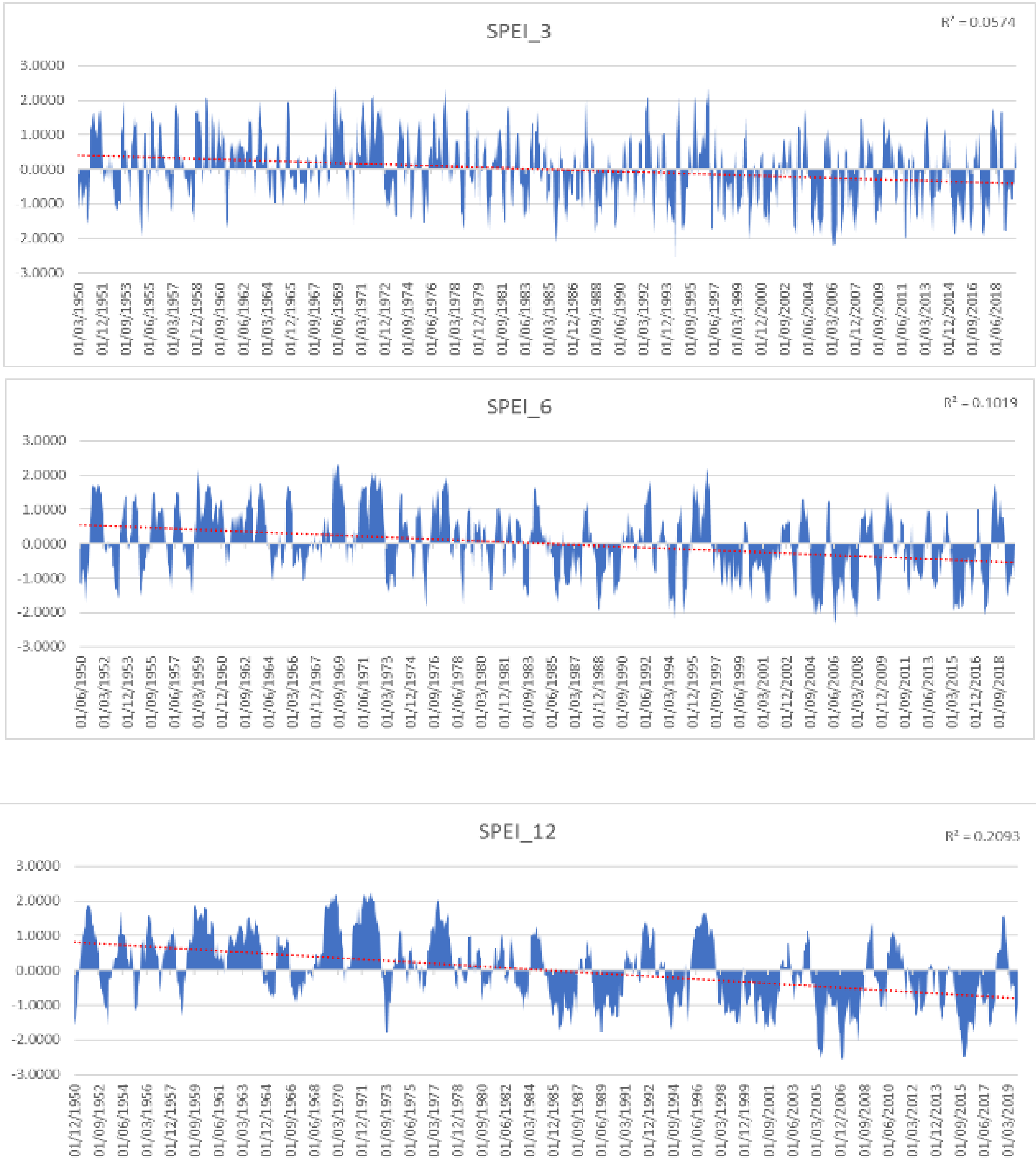

Figure 75. SPEI_3, SPEI_6 and SPEI_12 trend analysis for the study area.

Results show a clear increasing tendency of drought events that are more evident when long SPEI time lags are analysed. Indeed, 1987 and 2015 fire events occurred during a drought event window, thus accentuating the fire severity and its consequences for vegetation recovery. After these two fire events, only one quite long wet window period (from 1993 to 1997 approximately) occurred. A braking point or tipping point is also identified from these results, as a moment of trend change around 1985. This result agrees with the one identified by Carnicer et al., (2019) who identified a tipping point break around 1985. The analysis of several SPEI time scales results essential for characterizing the climate desertification trends of the area and easily identify the periods with water scarcity. The identification of these periods will be useful to plan restoration practices implementation.

4.1.5 SOC temporal trend

Methodology

The extraction of SOC temporal trend was performed by using *Trends.Earth* plugin within the open-source QGIS tool according to Giuliani et al. (2020). The most recent (update in June 2016) and improved version of *SoilGrids* (Hengl et al., 2017) has been used as the reference map product requested by the plugin. Such map was produced at 250 m spatial resolution and assessed for organic carbon and other soil properties available under the Open Data Base License. This product was primarily derived from MODIS satellite land products, SRTM DEM derivatives, climatic images and global landform and lithology maps by a machine learning supervised approach. In order to compute the trends of SOC, the software needs two different LC mappings to be compared, which are initially reclassified in 7 main classes: cropland, tree-covered, grassland, artificial, water body, other land, no data. For El Bruc case study, 2007 and 2017 has been used to be consistent with the other products. Then, according to specific coefficients related to the type of LC transition, a SOC map is produced for each LC map and, lastly, the SOC temporal trend mapping between the two years considered can be computed. For SOC losses greater than 10% soil degradation is considered.

Results

The resulting map of SOC degradation is the following Figure 76:

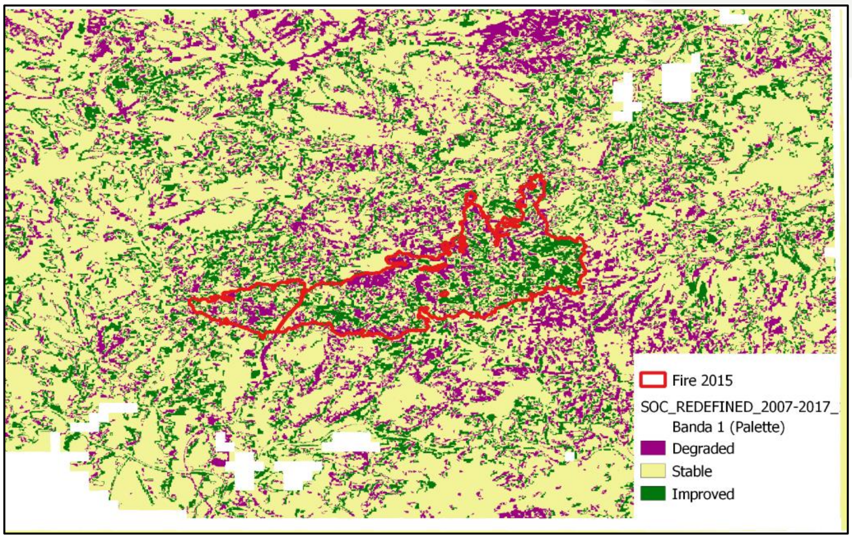

Figure 76. SOC degradation mappings produced for El Bruc.

The following considerations can be obtained:

- A total area of 24.6 % is considered in process of degradation;
- The major degradation process has occurred in areas that were shrublands or forest before the fire event;
- The areas that have improved mainly correspond to crops (Figure 77)

Figure 77. Overlay of ortophoto from 2015 and SOC degradation map. Purple areas are degraded areas mainly corresponding to forested areas while greenish areas are improving and correspond mainly to crops.

4.1.6 SDG 15.3.1 computation and land degradation mapping

Methodology

The calculation of SDG 15.3.1 for El Bruc has been done following the UNCCD guidelines. The 3 sub-indicators have been computed for the period 2007-2017, just after the main fire in 2015, obtaining 3 categorical maps with categories: *stable, improved, degradation*. LC sub-indicator has been computed using the baseline maps presented in section 4.1.1 at spatial resolution of 30 m. PP has been computed using *Trends.Earth* plug-in for QGIS software, based on MODIS annual product (MOD13Q1) at 250 m spatial resolution. SOC has also been computed using *Trends.Earth* based on *SoilGrid* product (2016) at 250 m spatial resolution. Since the computation of the SOC trend is based on the LC changes identified with the LC sub-indicator at 30 m, the output product is at 30 m.

In order to proceed with the integration of the 3 sub-indicators, PP sub-indicator has been resampled to 10 m using nearest neighbour algorithm, since it is a categorical map.

SDG 15.3.1 indicator presents 3 categories: *Loss, Gains and No change*. The sub-indicators integration decision criteria was based on the “*one-out, all-out*” rule. If any of the three sub-indicators presented degradation for a given pixel, the final category should be *Loss*.

Results

The land degradation mapping obtained for 2007-2017 for El Bruc is shown in Figure 78.

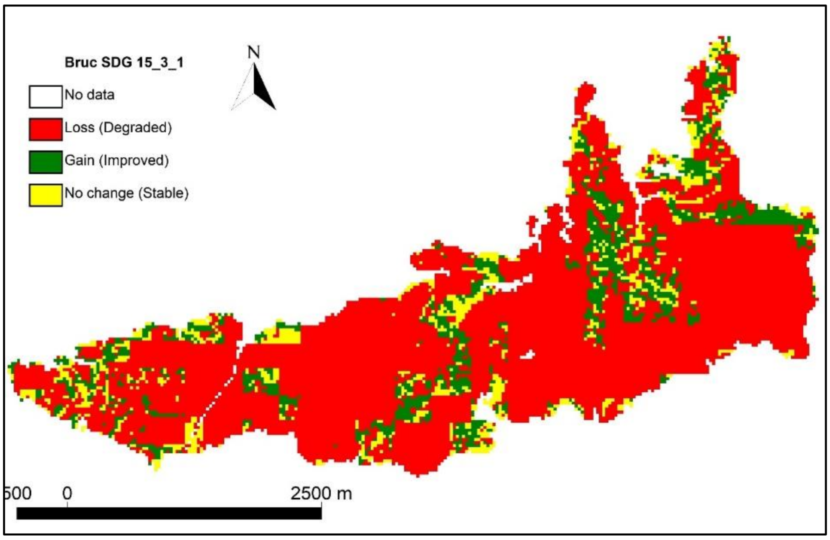

Figure 78. SDG 15.3.1 indicator for El Bruc region for the period 2007-2017.

The results show that the area where the fire occurred in 2015 was still undergoing a strong degradation process in 2017, corresponding to a 76.81% of the total area. The areas that present improvement (12.92%) or remain stable (10.27%) are mainly dedicated to agriculture.

4.2 Tifaracas (Gran Canaria, Spain)

Tifaracás is a desertified area located in the municipality of Artenara, on the island of Gran Canaria (Figure 79). It is located in Nublo II and Tamadaba N2K sites (sites code ES7010039 and ES0000111), within the El Nublo Rural Park, which in turn is included in the Gran Canaria Biosphere Reserve.

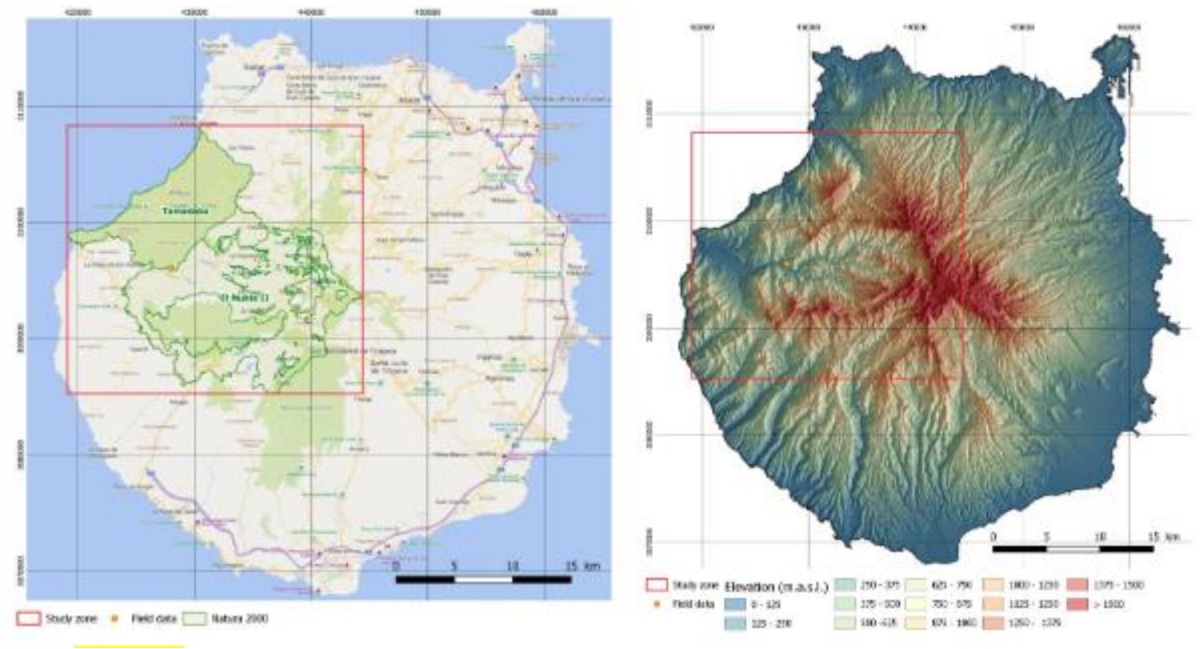

Figure 79. Location map of "Tifaracás" in Gran Canaria Island (red point) and the whole study area including Tamadaba and El Nublo II N2K sites (red square).

We find vegetation typical of the arid and semi-arid environments of the island, with a predominance of herbaceous species, although with a very low cover, for which it has a high risk of desertification. In the framework of the LIFE The Green Link project (LIFE15 CCA/SE/125) more than 4,000 seedlings of native forest species, trees and shrubs, were planted using the "Cocoon" system. The objective of the plantation is to reverse desertification processes protecting the soil against erosion and improve the ecological connectivity of the adjacent Canary pine forests.

The area is severely affected by desertification processes, which are aggravated by reduced rainfall, recurrent forest fires and herbivore caused by the abundant presence of wild goats. In recent years, dry periods, without rainfall, have lasted more than 10 months, which difficult the reforestation efforts that try to establish a vegetation cover in order to protect the soil from the erosion. Although soils are not particularly vulnerable to erosion due to the high stoniness, the low vegetation cover, the steep slopes of the slopes and the torrential rains favour erosive processes. These processes cause the loss of fertile soil, which makes it even more difficult to establish a vegetation cover.

The following indices and sub-indicators, reported in Table 35, have been selected in order to monitor the pressures and processes described above.

Table 35. Indices and sub-indicators selected for Tifaracas study site.

<table>
<tr><th colspan="2">Sub-indicators</th><th>Sensor</th><th>Spatial resolution (m)</th><th>Spatial frame</th><th>Temporal frame</th></tr>
<tr><td colspan="2" rowspan="2">LAND COVER MAP</td><td>Landsat</td><td>30</td><td rowspan="5">N2K +5 km buffer</td><td>2005; 2011; 2014</td></tr>
<tr><td>Sentinel-2</td><td>10</td><td>2016; 2021</td></tr>
<tr><td>PRIMARY PRODUCTIVITY</td><td>PLANT PHENOLOGY INDEX (PPI)</td><td rowspan="2">Sentinel-2</td><td rowspan="2">10</td><td>2017-2020</td></tr>
<tr><td colspan="2">BURN SEVERITY MAP</td><td>2019</td></tr>
<tr><td colspan="2">SOC</td><td>Sentinel-2</td><td>10; 30</td><td>2005 - 2021</td></tr>
</table>

4.2.1 LC temporal trend

Methodology

Analysis of LC maps was performed for years 2005, 2011, 2014, 2016 and 2021. They have been generated by automatic classification processes of images obtained from the Landsat series satellites (mainly Landsat-5/7/8) for year 2005-2014, through their TM, ETM+, OLI and MSI sensors and the incorporation of auxiliary information, available from the Information System on Soil Occupation of Spain. Maps of 2016 and 2021 have been generated using Sentinel-2A and 2B data (mosaic of tiles T28RDR and T28RDS) and a classification method based on kNN classifier (González-Guerrero et al., 2019). Bands with native spatial resolution of 20 meters (i.e., B5, B6, B7, B8A, B11, B12) were resampled, by a Nearest Neighbour algorithm, at 10 meters as those native (B2, B3, B4, B8). For 2016 map, 15 images distributed along the year were selected to obtain a good representation of the phenological dynamics of natural vegetation and crop covers (Moré and Pons, 2007). For 2021 map, 27 images were used. Table 36 shows the whole of satellite imagery considered for the 2017 and 2021 classifications with their acquisition dates.

Table 36. List of satellite imagery considered for the LC mappings.

Year	Acquisition date		Sensor	Spatial resolution (m)	Bands
2016	January, 7th January, 17th March, 17th March, 27th June, 5th June, 25th July, 15th	July, 25th August, 4th August, 14th August, 24th September, 3rd September, 13th October, 23rd November, 2nd	Sentinel-2 A	10	B2, B3, B4 (Vis) B5, B6, B7 (Red Edge) B8, B8A (NIR) (8 bands) NDVI and NDWI2
2021	January, 20th January, 25th January, 30th February, 14th February, 19th March, 11th March, 16th March, 26th April, 20th May, 20th May, 30th June, 14th July, 14th July, 19th	August, 18th August, 23rd August, 28th September, 2nd October, 2nd October, 12th October, 17th October, 27th November, 1st November, 16th November, 21st December, 26th December, 31st	Sentinel A/B		

These images were classified using the kNN algorithm to obtain a map with 8 categories. A set of training areas collected through visual interpretation of available orthophotos and distributed with a "stratified" sampling to ensure a minimum number of polygons–samples for each class (i.e., stratum) (Congalton et al., 2014) were considered for training the classifier and subsequent validation of the output map.

Results

The analysis of temporal land cover trends performed in this area shows the following trends for the specific land cover categories (Figure 80 and Table 37).

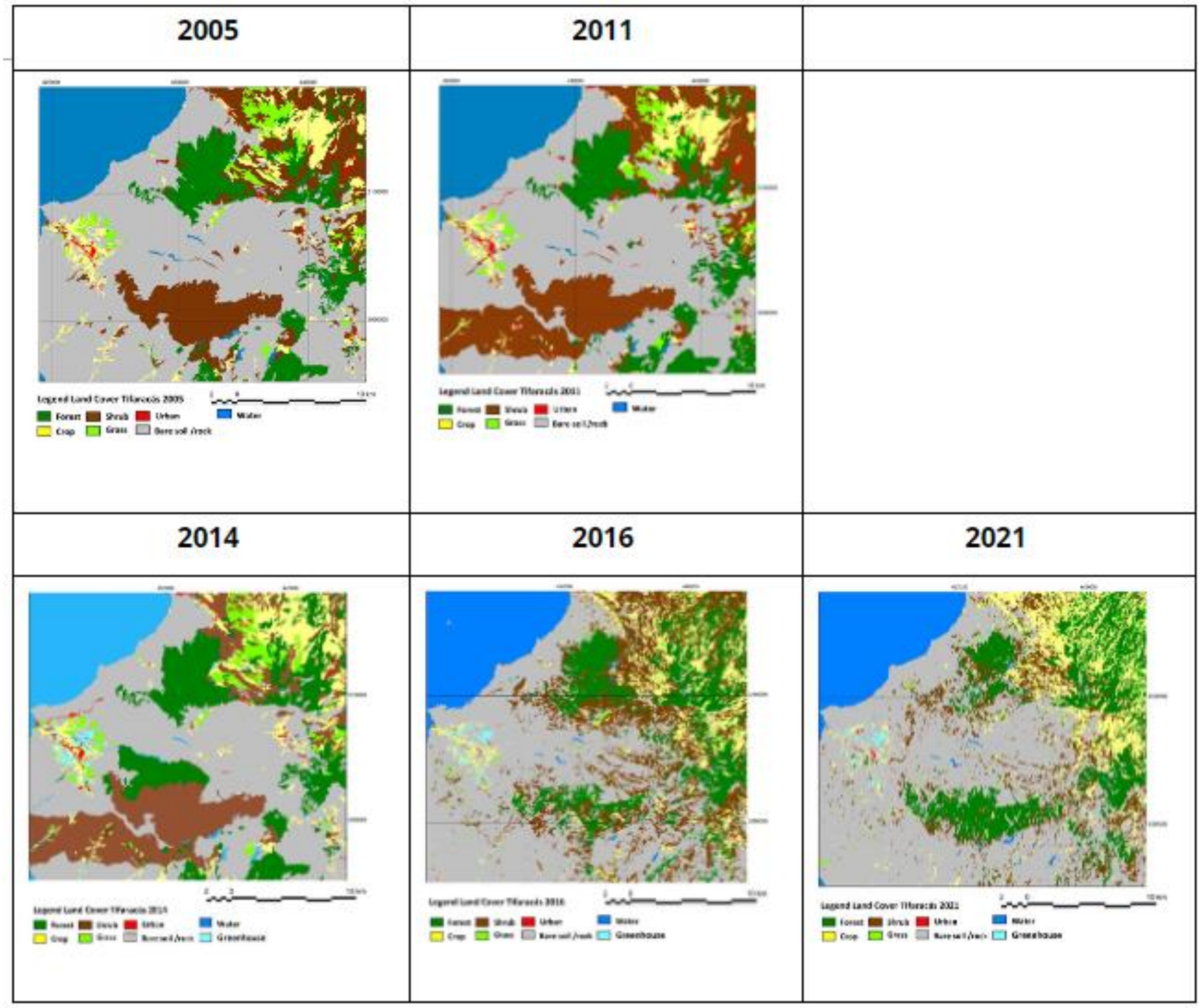

Figure 80. Land cover maps generated.

Table 37. Land cover categories (ha) for each year respect Tifaracás pilot area (in ha).

	2005	2011	2014	2016	2021
Bare soil /rock	29127.46	25658.18	23590.65	26498.26	29764.93
Crop	3774.93	3337.1	4912.43	4917.88	6202.2
Forest	6253.64	6911.13	9336.88	8246.99	8661.01
Grasslands	1651.84	1559.27	1954.27	521.96	823.81
Greenhouse			306.28	245.7	198.29
Shrublands	9788.92	13091.56	10345.31	10474.88	5353.29
Urban Areas	323.61	357.31	390.43	95.2	63.84
Water bodies	7481.34	7487.19	7562.7419	7400.87	7334.37

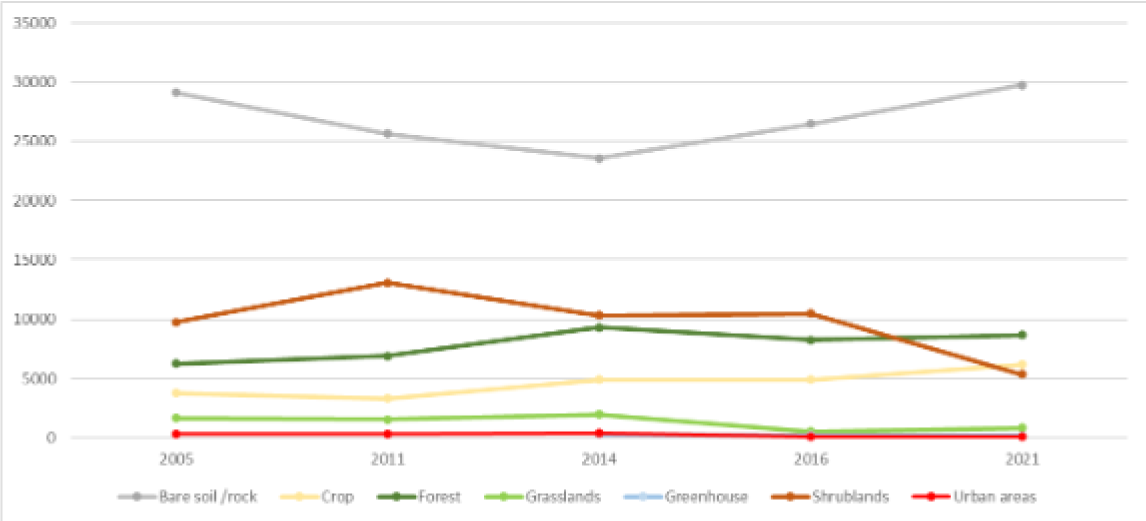

Figure 81. Temporal trend of LC classes presence.

From the analysis of the temporal trend for the LC of the area where restoration practices were performed (Figure 81), the following considerations can be evaluated:

- This study area has been undergoing a strong desertification process since 2014. Bare soil areas have increased while shrubland areas have decreased;
- Other types of categories remain similar during the period analysed (16 years), indicating the slow changing processes occurring in the area.

In terms of LC degradation and following the transitions defined by the UNCCD protocol (degradation, stable or Improvement), the evolution of LC of the study area (Figure 82) between 2005 and 2021 shows some areas that have been strongly degraded during these years due to fire events (2019).

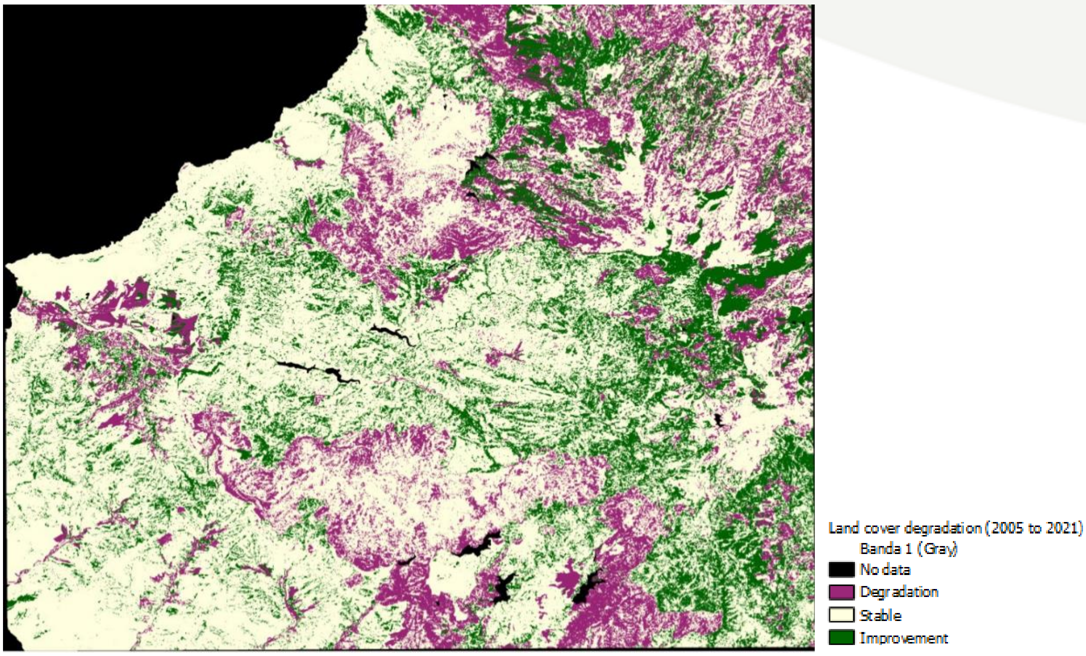

Figure 82. Temporal trend of LC classes presence.

4.2.2 BS temporal trend

Methodology

The Tamadaba area suffered a big fire event starting in August, 17th 2019. Such event did not affect the study area. However, since the area affected by the fire is close and similar regarding the LC types to the one included in the project, an analysis to identify the fire-affected area has been performed in order to monitor the recovery trends of these type of land covers. BS has been calculated according to Nasery & Kalkan (2020) for a satellite image just before the event and just after the event. Following, the difference between the former and the latter NBRs (dNBR) has been also computed as indicator of burn severity. The analysis has been carried out using Sentinel-2 images. The list of images used is included in Table 38.

Table 38. List of satellite imagery considered for the BS mappings.

Year	Acquisition date	Sensor	Spatial resolution (m)	Bands
2019	June, 20th August, 24th	Sentinel-2 A /B	10	B8A (NIR narrow) B12 (SWIR)

Results

Resulting mappings are shown in Figures 83 and 84.

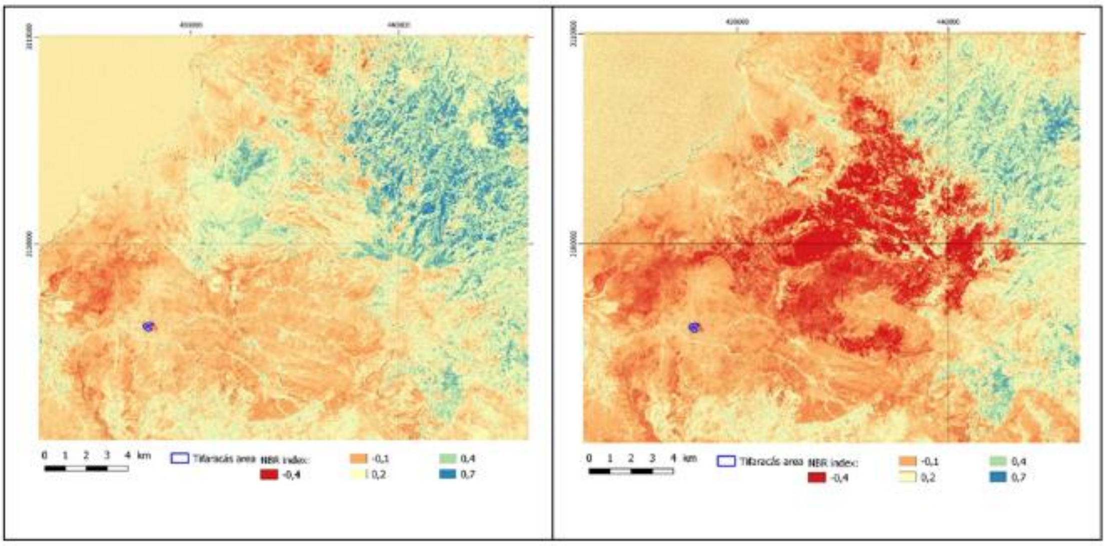

Figure 83. BS mapping for Sentinel-2 June, 20th (pre-fire) (left) and August, 24th (post-fire) (right).

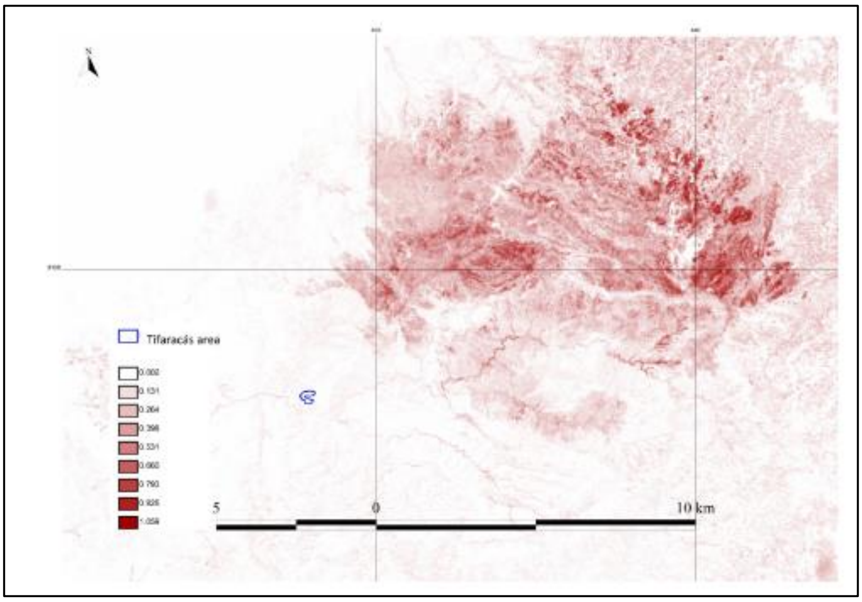

Figure 84. dNBR indicating the severity of the fire event.

From the analysis of the BS mapping, it can be concluded that:

- Part of the area affected by the fire event was forest composed by *Pinus canariensis*, a fire adapted species, very resistant to fight high temperatures and flames (due to the tick, insulating bark), with capacity to regrowth after fire events;
- Most of the area presenting high intensity fire corresponded to bare soil and rocks;
- In areas with very low or null vegetation, the NBR accuracy is reduced and the limits of the burned area are quite inaccurate. This fact should be considered when monitoring areas affected by advanced desertification processes.

4.2.3 PP temporal trend

Methodology

Primary productivity has been analysed based on the Copernicus HR-VPP product. TPROD for the 4 available years (2017-2020) has been downloaded from WeKEO platform and combined with the area of the study to monitor its productivity trends. First year of analysis correspond to 2017, two years before the fire events of 2019.

Results

Figure 85 illustrates the TPROD product and Table 39 and Figure 87 quantitatively analyse the results. Figure 86 shows the difference of productivity for the period 2022 and 2017. In 2019, the perimeter of the fire is easily identified and the distribution of the main productivity degradation is sparse along the whole area.

Table 39. Statistics of all pixels included in the study area.

	2017	2018	2019	2020	2021	2022
Mean	796.6663	847.5101	721.2555	465.0731	1255.427	1154.47
St. Dev	716.1951	702.8564	725.1095	597.9858	971.9349	848.5118
Minimum	0	0	0	0	0	0
Maximum	8898	9598	9269	8063	17072	13985
1st quartile	534	579	350	132	579	534
Media	1154.47	1255.42	1115.8	1.94	1054	1002
3rd quartile	1584	1690	1599	1132	1690	1584

2017	2018
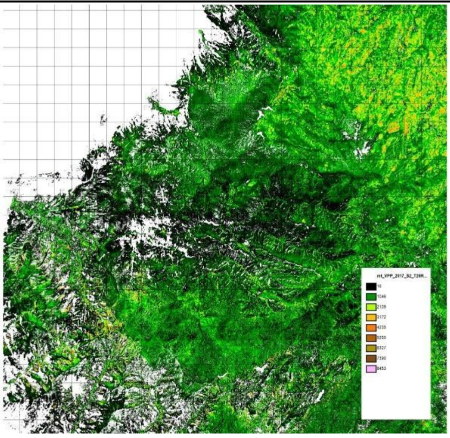	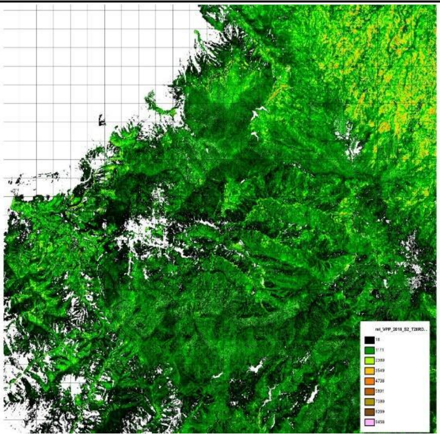
2019	**2020**
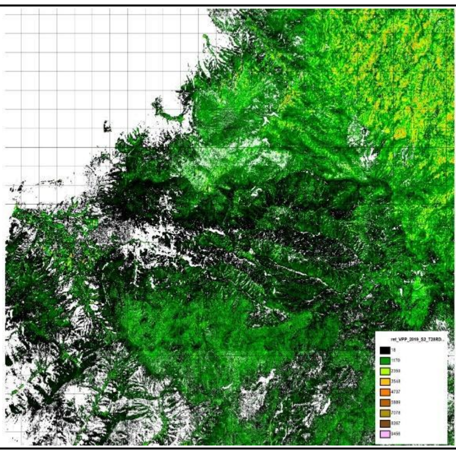	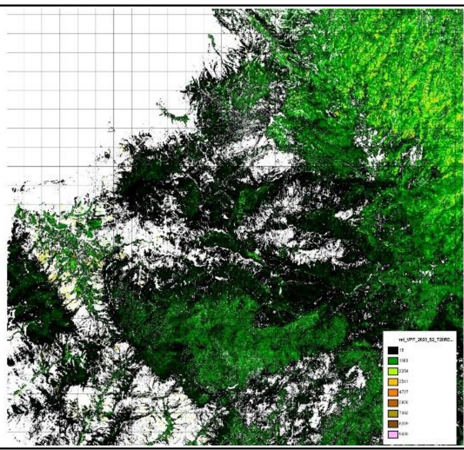
2021	**2022**
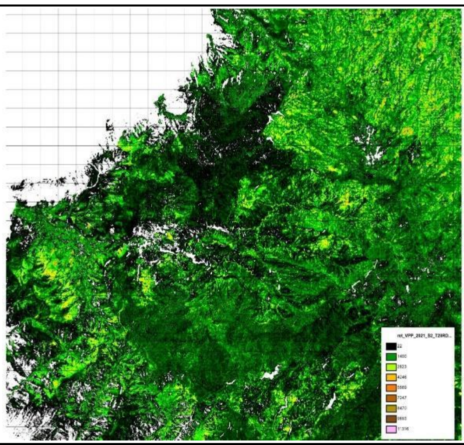	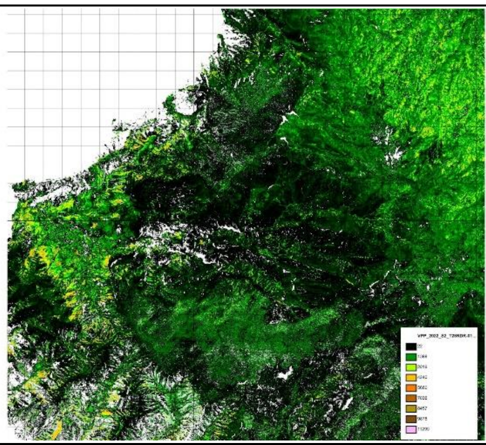

Figure 85. TPROD. The growing season integral computed as sum of all daily values minus their base level value (units: PPI * day).

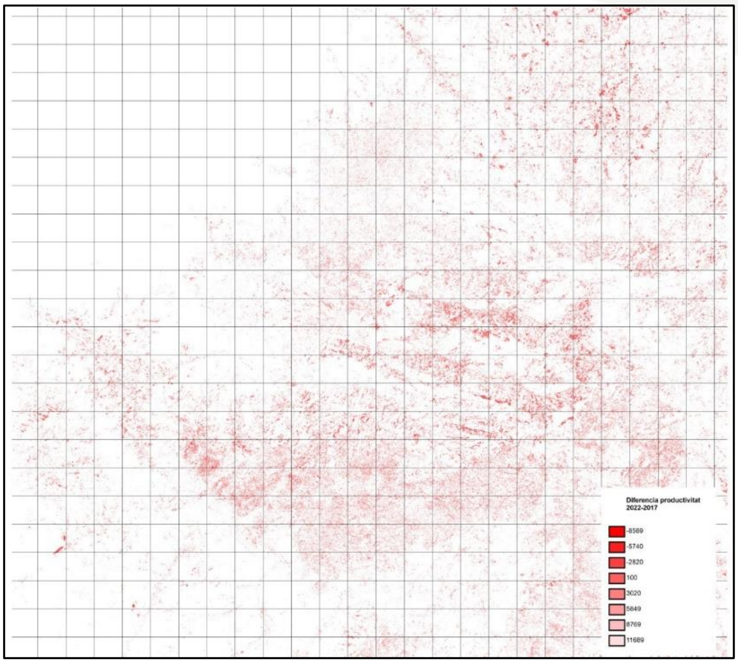

Figure 86. Difference of productivity between 2022 and 2017.

The trend of productivity clearly decreases until 2020 (R2=0.71) and after this period it slightly increases. This might be due to climatic conditions. An important aspect to highlight is that although the minimum and the maximum productivity values remain almost constant, the 1st and 3rd quartiles decrease significantly with time, except for the last two years.

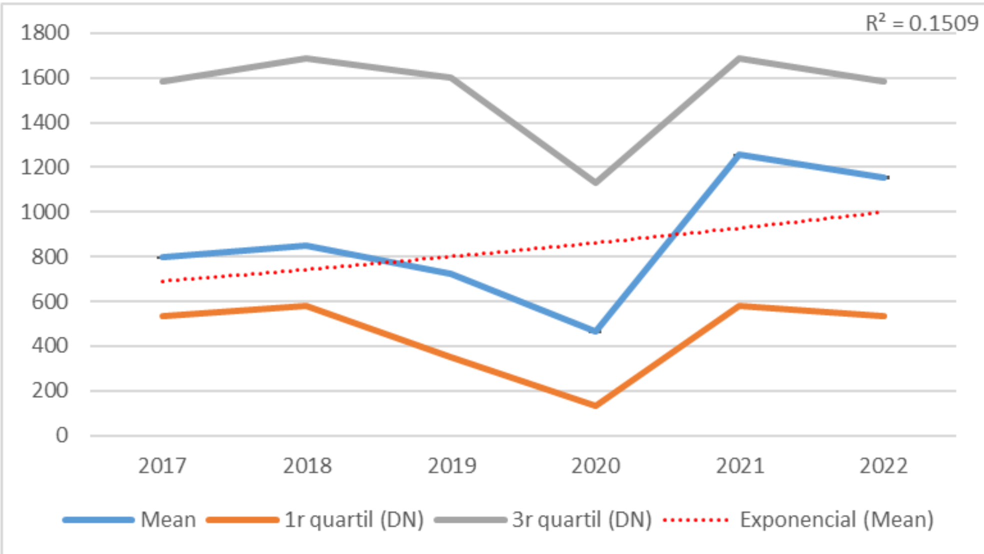

Figure 87. Trends of mean, min, max, 1st quartile and 3rd quartile of TPROD of the area.

4.2.4 SOC temporal trend

Methodology

The extraction of SOC temporal trend was performed following the same methodology as for El Bruc case study. The initial and final years considered for the land cover changes were 2005 and 2021.

Results

Results (Figure 88) show that most of the areas presenting SOC degradation are also presenting LC degradation. Similar to El Bruc case study, differences between LC degradation and SOC degradation are found at croplands, where SOC is mainly considered stable or even improve in 2021.

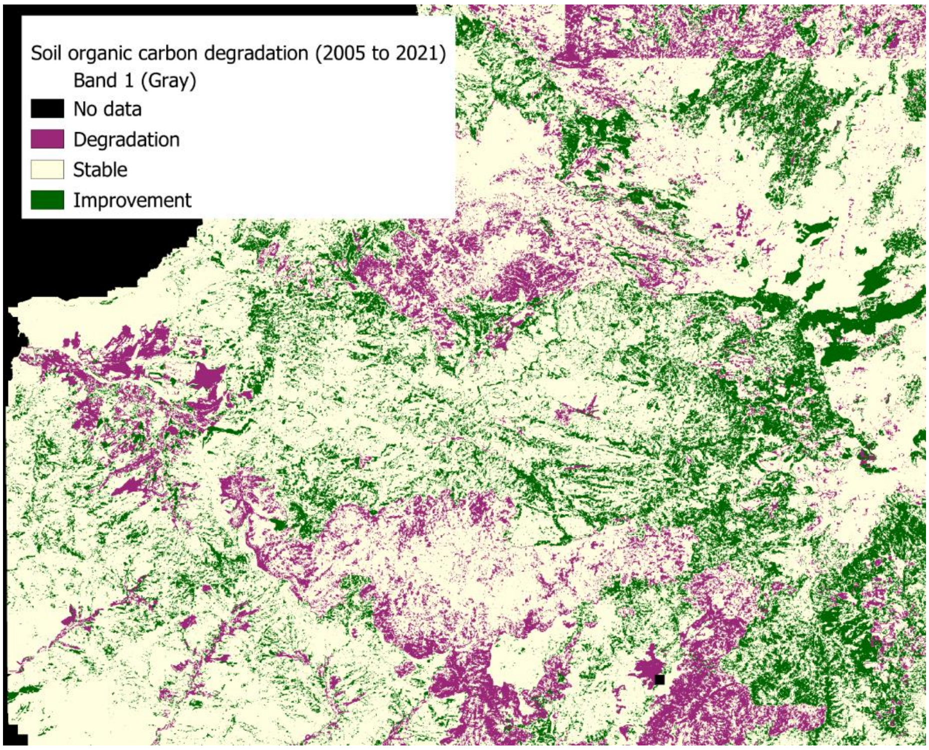

Figure 88. SOC degradation mapping produced for Tifaracás for period 2005-2021.

4.2.5 SDG 15.3.1 computation and land degradation mapping

Methodology

The calculation of SDG 15.3.1 for Tifaracás has been done following the UNCCD guidelines. The 3 sub-indicators have been computed for the period 2005-2021 (PP from 2005 to 2020) obtaining 3 categorical maps with categories: *stable, improved, degradation*. LC sub-indicator has been computed using the baseline maps presented in section 4.2.1 at spatial resolution of 10 m. PP has been computed using *Trends.Earth* plug-in for QGIS software, based on MODIS annual product (MOD13Q1) at 250 m spatial resolution. SOC has also been computed using *Trends.Earth* based on *SoilGrids* product (2016) at 250 m spatial resolution. Since the computation of the SOC trend is based on the LC changes identified with the LC sub-indicator at 10 m, the output product is at 10 m.

In order to proceed with the integration of the 3 sub-indicators, PP sub-indicator has been resampled to 10 m using nearest neighbour algorithm, since it is a categorical map.

The SDG 15.3.1 indicator presents 3 categories: *Loss, Gains and No change*. The sub-indicators integration decision criteria was based on the “*one-out, all-out*” rule. If any of the three sub-indicators presented degradation for a given pixel, the final category should be *Loss*.

Results

The land degradation mapping obtained for 2005-2021 for Tifaracás is shown in Figure 89:

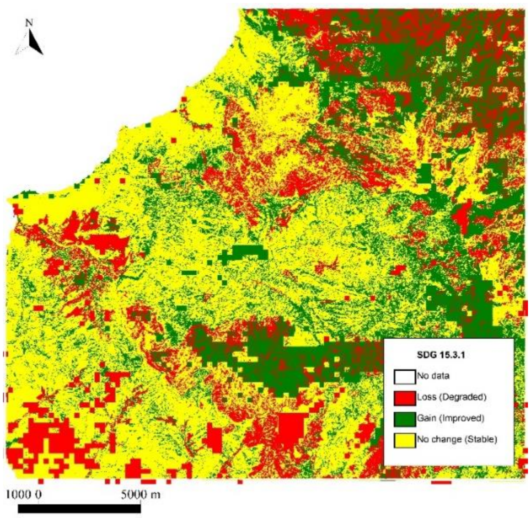

Figure 89. SDG 15.3.1 indicator for Tifaracás region for period 2005-2021.

One of the main issues identified in the final map is the artifacts derived of using sub-indicators that have different resolutions. If the end user prefers to avoid these artifacts, it is recommended to work with the smallest resolution of the 3 sub-indicators (in this case would have been 250 m), although spatial detail will be lost.

It is also noteworthy, that the LC transition of *Trends.Earth* is based on 7 land cover categories (wetlands, water, artificial, grasslands, croplands, tree cover and other covers), but none of them is related to shrublands, a typical cover at Mediterranean landscapes. This forced classification might introduce some accuracy errors.

Once the indicator obtained, the proportions of land that is degraded over the total land area has been also computed. A 21.59% of the area present degradation for the period 2005-2021, a 28.94% present improvement and the rest 49.46% do not present changes in terms of degradation.

Conclusions

RS data and techniques represent an essential support for the monitoring of the LD status.

In the framework of NewLife4Drylands project, Action A2 has focused on the extraction from RS data of EVs (indices, indicators or their proxies) at local scale useful to characterize and monitor the LD status of each study site according to the local pressures and threats affecting each site. Freely available open data have been considered as much as possible.

For each EV, the temporal trend has been analysed and time-series maps have been produced. These EVs have been considered as sub-indicators to be integrated to compute the SDG 15.3.1 indicator as recommended by United Nations Convention to Combat Desertification (UNCCD) to characterize the LD status of the site producing degradation mappings.

Interesting information about LD status have emerged and both quantitative and qualitative evaluations have been possible for long-term and medium/short term analysis for each study site as reported in the specific sections.

The following overall considerations can be addressed:

- Working at a local scale, it is essential to produce information that is truly useful to local decision makers, and freely available services such as Copernicus at a pan-European scale are unreliable.
- Starting from the analysis of local pressures and threats affecting each site is essential to address all the investigations by choosing the most suitable sub-indicators to be integrated in the calculation of SDG 15.3.1: as an example even if in the UNCCD Guidelines (Sims et al., 2021) changes in cultivated land use are not degradation this is not true for the Alta Murgia , because can be considered the main cause of biodiversity loss from the natural grassland ecosystem;
- Focusing on a specific class of LC subject to degradation can allow for reduced calculation complexity;
- The QGIS *Trends.Earth* plugin is the current tool for calculating SDG 15.3.1 and its main sub-indicators, but it often has problems of instability and the customised use of its own data is not so straightforward: for example, the calculation of SOC is based on the use

of 2 mappings of LCs that are reclassified by the tool into 7 macro-classes of LCs that in many cases do not allow the local landscape to be represented with efficacy;

- The use of additional sub-indicators in the calculation of SDG 15.3.1 needs to be better investigated in order to assess not only the empirical and crisp thresholds, but also a fuzzy approach could represent higher reliability;
- Some known sub-indicators would require more suitable formulations: HP, for example, would require taking into account the season (month) in which the presence of water (rain/snow) during the year and its quantity;
- The availability of ground truth data is essential for the validation of mappings obtained with RS techniques and many more field inspections would be necessary: in countries where other projects have been previously funded, more accurate validations have been possible.

References

Adamo, M.; Tomaselli, V.; Tarantino, C.; Vicario, S.; Veronico, G.; Lucas, R.; Blonda, P. (2020). Knowledge-based classification of grassland ecosystem based on multi-temporal WorldView-2 data and FAO-LCCS taxonomy. Remote Sensing, 12, 1447. https://doi.org/10.3390/rs12091447

Adamo, M.; Tarantino, C.; Tomaselli, V.; Veronico, G.; Nagendra, H.; Blonda, P. (2016). Habitat mapping of coastal wetlands using expert knowledge and Earth observation data. J. Appl. Ecol., 53, 1521–1532. https://doi.org/10.1111/1365-2664.12695

Adamo, M.; Tarantino, C.; Tomaselli et al. (2014). Expert knowledge for translating land cover/use maps to general habitat categories (GHC). Landsc. Ecol., 29, 1045–1067. DOI: 10.1007/s10980-014-0028-9

Anys, H.; Bannari, A.; He, D.C.; Morin, D. (1994). Texture analysis for the mapping of urban areas using airborne MEIS-II images. In Proceedings of the First International Airborne Remote Sensing Conference and Exhibition, Strasbourg, France, 12–15 September 1994; Volume 3, pp. 231–245.

Borgogno-Mondino, E.; de Palma, L.; Novello, V. (2020). Investigating Sentinel 2 Multispectral Imagery Efficiency in Describing Spectral Response of Vineyards Covered with Plastic Sheets. Agronomy 10, 1909. doi:10.3390/agronomy10121909

Carnicer, J.; Domingo-Marimon, C.; Ninyerola, M.; Camarero, J.J.; Bastos, A.; López-Parages, J.; Blanquer, L.; et al. (2019). Regime Shifts of Mediterranean Forest Carbon Uptake and Reduced Resilience Driven by Multidecadal Ocean Surface Temperatures. Global Change Biology 25, (8), 2825-40. https://doi.org/10.1111/gcb.14664

Chad A. Greene, Kaustubh Thirumalai, Kelly A. Kearney, Jose Miguel Delgado, Wolfgang Schwanghart, Natalie S. Wolfenbarger, Kristen M. Thyng, David E. Gwyther, Alex S. Gardner, and Donald D. Blankenship (2019). The Climate Data Toolbox for MATLAB. Geochemistry, Geophysics, Geosystems, 20, 3774-3781. doi:10.1029/2019GC008392

Congalton, R.G.; Gu, J.; Yadav, K.; Thenkabail, P.; Ozdogan, M. (2014). Global Land Cover Mapping: A Review and Uncertainty Analysis. Remote Sens. 6, 12070–12093.

Congalton, R.G.; Kass, G. (2009). Assessing the Accuracy of Remotely Sensed Data: Principle and Practices, 2nd ed.; Taylor & Francis Group: Abingdon, UK, 2009; ISBN 9781420055122.

Deliverable A2.1, NewLife4Drylands. (September 2021). https://www.newlife4drylands.eu/a2-1_report-on-indicators-for-the-evaluation-of-restoration-actions-to-combat-degradation/

Di Gregorio, A.; Jansen, L.J.M. (2005). Land Cover Classification System (LCCS): Classification Concepts and User Manual. Food and Agriculture Organization of the United Nations: Rome, Italy.

Domingo-Marimon, C. (2016). Contributions to the knowledge of the multitemporal spatial patterns of the Iberian Peninsula droughts from a Geographic Information Science perspective. Revista de Teledetección 0(46), 171–173. doi:10.4995/raet.2016.5190

Forte, L.; Perrino, E.V.; Terzi, M. (2005). Le praterie a Stipa austroitalica Martinovsky ssp. austroitalica dell’Alta Murgia (Puglia) e della Murgia Materana (Basilicata). Fitosociologia, 42, 83–103

Foody, G.M.; Mathur, A. (2004). A relative evaluation of multiclass image classification by support vector machines. IEEE Trans. Geosci. Remote Sens., 6, 1335–1343

Giuliani, G.; Chatenoux, B.; Benvenuti, A.; Lacroix, P.; Santoro, M. & Mazzetti, P. (2020). Monitoring land degradation at national level using satellite Earth Observation time-series data to support SDG15 – exploring the potential of data cube. Big Earth Data, 4:1, 3-22, DOI: 10.1080/20964471.2020.1711633

González-Guerrero, O.; Pons, X.; Bassols-Morey, R.; Camps Fernández , F.X. (2019). Dinàmica de les superfícies de conreu a Catalunya mitjançant teledetecció en el període 1987-2012. Revista Quaderns Agraris, 46, 59-91.
https://raco.cat/index.php/QuadernsAgraris/article/view/359167

Hargreaves, George H., and Zohrab A. Samani. "Reference crop evapotranspiration from temperature." Applied Engineering in Agriculture 1.2 (1985): 96-99. doi:10.13031/2013.26773.

Hengl, T.; Mendes de Jesus, J.; Heuvelink, G.B.M.; Ruiperez Gonzalez, M.; Kilibarda, M.; Blagotić, A. et al. (2017). SoilGrids250m: Global gridded soil information based on machine learning. PLoS ONE 12(2): e0169748. doi:10.1371/journal.pone.0169748

Huang, C.; Davis, L.S.; Townshend, J.R.G. (2002). An assessment of support vector machines for land cover classification. Int. J. Remote Sens., 23, 725–749.

ICGC (2021). Mapa topogràfic de Catalunya 1:50.000. Available in: https://www.icgc.cat/Administracio-i-empresa/Descarregues/Cartografia-topografica/Mapa-topografic-1-50.000

Keenan, R.J. (2015). Climate change impacts and adaptation in forest management: a review. Annals of Forest Science 72, 145–167. https://doi.org/10.1007/s13595-014-0446-5

Mairota, P.; Cafarelli, B.; Labadessa, R.; Lovergine, F.; Tarantino, C.; Lucas, R.; Nagendra, H.; Didham, R. (2015). Very high resolution Earth observation features for monitoring plant and animal community structure across multiple spatial scales in protected areas. Int. J. Appl. Earth Obs. Geoinf., 37, 100–105

McMahon, T. A., et al. "Estimating actual, potential, reference crop and pan evaporation using standard meteorological data: a pragmatic synthesis." Hydrology and Earth System Sciences 17.4 (2013): 1331-1363. doi:10.5194/hess-17-1331-2013

Moré, G.; Pons, X. (2007). Influencia del número de imágenes en la calidad de la cartografía detallada de vegetación forestal. Revista de Teledetección, 28, 61- 68. Recuperado de http://www.aet.org.es/revistas/ revista28/7-111_More_revisado.pdf

Morris, B.; Dupigny-Giroux, L. (2010). Using the Nir/blue surface moisture index to explore feature identification at multiple spatial resolutions. In Proceedings of the Abstracts of AGU Fall Meeting, San Francisco, CA, USA,13–17 December 2010; Volume 1, p. 1298.

Mountrakis, G.; Im, J.; Ogole, C. (2011). Support vector machines in remote sensing: A review. ISPRS J. Photogramm. Remote Sens., 66, 247–259.

Nasery, S.; Kalkan, K. (2020). Burn Area Detection and Burn Severity Assessment Using Sentinel 2 MSI Data: The Case of Karabağlar District, İzmir/Turkey. Turkish Journal of Geosciences, Vol. 1, Issue 2, pp. 72-77.

Othman, A.A.; Gloaguen, R. (2014). Improving lithological mapping by SVM classification of spectral and morphological features: The discovery of a new chromite body in the Mawat ophiolite complex (Kurdistan, NE Iraq). Remote Sens., 6, 6867–6896.

Sims, N.C., Newnham, G.J., England, J.R., Guerschman, J., Cox, S.J.D., Roxburgh, S.H., Viscarra Rossel, R.A., Fritz, S. and Wheeler, I. (2021). Good Practice Guidance. SDG Indicator 15.3.1, Proportion of Land That Is Degraded Over Total Land Area. Version 2.0. United Nations Convention to Combat Desertification, Bonn, Germany. Available online at:

https://www.unccd.int/publications/good-practice-guidance-sdg-indicator-1531-proportion-land-degraded-over-total-land

Tarantino, C.; Aquilino, M.; Labadessa, R.; Adamo, M. (2023). “Time Series of Land Cover Mappings Can Allow the Evaluation of Grassland Protection Actions Estimated by Sustainable Development Goal 15.1.2 Indicator: The Case of Murgia Alta Protected Area”, Remote Sensing, Special Issue “Remote Sensing Measurements for Monitoring Achievement of the Sustainable Development Goals (SDGs)”, 15(2), 505, https://doi.org/10.3390/rs15020505

Tarantino, C.; Forte, L.; Blonda, P.; Vicario, S.; Tomaselli, V.; Beierkuhnlein, C.; Adamo, M. (2021). Intra-Annual Sentinel-2 Time-Series Supporting Grassland Habitat Discrimination”, Remote Sensing, Special Issue “Remote Sensing for Habitat Mapping, 13(2), 277, ISSN: 2072-4292, https://doi.org/10.3390/rs13020277

Tarantino, C.; Casella, F.; Adamo, M.; Lucas, R.; Beierkuhnlein, C.; Blonda, P. (2019). Ailanthus altissima mapping from multi-temporal very high resolution satellite images. ISPRS Journal of Photogrammetry and Remote Sensing. https://doi.org/10.1016/j.isprsjprs.2018.11.013

Tomaselli, V.; Dimopoulos, P.; Marangi, C.; Kallimanis, A.S.; Adamo, M.; Tarantino et al. (2013). Translating land cover/land use classifications to habitat taxonomies for landscape monitoring:

A Mediterranean assessment. Landsc. Ecol. 2013, 28, 905–930. DOI: 10.1007/s10980-013-9863-3

Trimble. Ecognition Developer 9.5. Reference Book. (2019). Available online: https://docs.ecognition.com/v9.5.0//

Vicario, S.; Adamo, M.; Alcaraz-Segura, D.; Tarantino, C. (2020). Bayesian Harmonic Modelling of Sparse and Irregular Satellite Remote Sensing Time Series of Vegetation Indexes: A Story of Clouds and Fires. Remote Sensing, Special Issue “Remote Sensing in Ecosystem Modelling”, 12(1), 83. doi:10.3390/rs12010083

Xeidakis, G. S. & Delimani, P. (2002). Coastal erosion problems in Northern Aegean coastline, Greece. The case of the Rhodope Prefecture coasts. Environmental Studies, 8: 151 - 158

Yang, X. (2011). Parameterizing support vector machines for land cover classification. Photogramm. Eng. Remote Sens., 77, 27–38.